EXPLOITING THE SPIN OF PHOTONS AND ELECTRONS IN LIGHT-MATTER INTERACTIONS

A DISSERTATION
SUBMITTED TO THE FACULTY OF THE GRADUATE SCHOOL
OF THE UNIVERSITY OF MINNESOTA
BY

LI HE

IN PARTIAL FULFILLMENT OF THE REQUIREMENTS
FOR THE DEGREE OF
DOCTOR OF PHILOSOPHY

MO LI

May, 2018

Acknowledgements

Looking back at the past five years of my graduate studies, there are many people that I owe thanks to. First of all, I would like to express my deepest gratitude to my advisor, Prof. Mo Li for the great guidance and support throughout my Ph.D. He has provided me not only the wonderful research resources but also freedom and encouragement to explore my own interest, which made this diverse work possible.

I would like to thank all the colleagues in Prof. Mo Li's group. In particular, I am grateful to Dr. Huan Li, who taught me every experimental skill with great patience when I just started in the group. The discussions with Huan have always been inspiring and helpful for me. I would also like to thank Dr. Yu Chen, Dr. Semere Tadesse, Dr. Nathan Youngblood for their help on my research projects.

I would like to acknowledge Prof. Jianping Wang for a great collaboration with his group and all the help. I want to thank Dr. Junyang Chen for providing me hundreds of samples in the ultrafast magnetization switching experiment.

I would like to thank Prof. Paul Crowell, Prof. Alex Kamenev and Prof. Joseph Talghader for reviewing this dissertation and serving as my defense committee. I benefitted a lot from Prof. Kamenev's lectures on electrodynamics and solid state physics.

Finally, I would like to thank my parents and entire family for their endless

support and love. I will always be greatly indebted to them.

Dedication

To my family.

Abstract

In light-matter interaction, the conservation law of angular momentum requires the transfer of angular momentum of light to matter, which consequently couples light polarization to various state variables of materials, such as mechanical motion, magnetization or charge current, thus gives rise to a plethora of intriguing physical phenomena. This dissertation focuses on the roles of photon spin and electron spin in light-matter interaction. Here, the angular momentum transfer in three different scenarios are studied.

First, in an integrated optomechanical device, the spin angular momentum of light propagating in a waveguide is revealed through the use of optical torque to excite torsional motion of the device. The quantitative optical torque measurement confirms the spin angular momentum of a photon in waveguide to be on the order of $\hbar$. Our measurement also provides a check of the famous Minkowski-Abraham dilemma of photon angular momentum and verifies the Minkowski momentum applies in our system.

Second, the coupling of light polarization and electron spin orientation is investigated in the optical excitation of surface states in a 3D topological insulator Bi_2Se_3. The angular momentum conservation manifests itself in the spin-dependent optical selection rules and the generation of a photocurrent at zero bias voltage.

Finally, we present the all-optical manipulation of magnetic order in ferrimagnetic alloy Gd(FeCo) using sub-picosecond laser pulses as the ultrafast stimuli. The instantaneous heating of the electron temperature due to light absorption

triggers the energy and angular momentum exchange between the three thermodynamic reservoirs (electron, spin and lattice) and leads to the switching of magnetization. As a step towards device application, we demonstrate an magnetic tunnel junction that can be switched all-optically without any external magnetic fields.

Contents

List of Tables

List of Figures

Chapter 1

Introduction

1.1 Overview

As one of the elementary particles, photons carry not only energy but also momentum, both linear and angular ones cite. The energy and momentum of light are implicitly embedded in the Maxwell equations, the classical theory that governs the interaction between light and matter. In fact, the energy and momentum of light are obvious when consider a charged particle experiences a Lorentz force when is subject to electromagnetic fields. The induced acceleration of the particle manifests the exchange of energy and momentum with light. From the quantum theory of light, the linear and angular momentum of a single photon are connected to its two fundamental degrees of freedom: frequency ω and polarization. Interestingly, for a circularly polarized photon in vacuum, the linear momentum is proportional to its frequency as $\hbar\omega/c$, whereas the angular momentum is a constant $\hbar$.

The research on the interaction between light and matter has formed the foundation of modern optoelectronics and spawned numerous technologies ranging

from optical communication, imaging to solar energy that have profound impacts on our society. Particularly, most of the optoelectronic devices have been developed based on the energy and linear momentum attributes of light, namely the transfer of energy and linear momentum with materials in the process of absorption, emission or diffraction of light, whereas the role of angular momentum is often ignored. Nevertheless, the conservation law also requires the exchange of angular momentum between light and matter, which could, in some circumstances, couple light polarization to various state variables of materials and lead to a plethora of intriguing physical phenomena.

The most intuitive example of such an angular momentum transfer is the light propagation in a birefringent dielectric. The continuous evolution of light polarization along the propagation direction implies the periodic exchange of angular momentum between light and the dielectric, and thus a spatially varying torque applied on the dielectric by light. A theoretical derivation based on the Maxwell equations, a completely classical theory, reveals that the angular momentum of a circularly polarized photon in vacuum is quantized to $\hbar$, in consistent with the quantum theory [1]. Because $\hbar$ is extremely small, the resulted optical torque is typically negligible to have any effect on the motion of a macroscopic object. However, the mechanical effect of light can be dramatically enhanced in nanophotonic devices, where light is tightly confined at the sub-wavelength scale and the device size goes down to a few microns or even smaller, enabling the coupling between light polarization and objects' rotational degree of freedom [2].

The angular momentum transfer could also manifest itself in the optical transitions of electrons in either isolated atoms or solids. For an optical transition to happen, the angular momentum difference in the initial and final electronic states must be compensated by photons. The required balance in angular momentum of

photons and electronic states sets strict rules for certain transitions to be allowed or forbidden, namely, the optical selection rules. Therefore, when consider a system with spin splitting (due to either spin-orbit coupling or Zeeman effect), the selection rules could couple light polarization to the electron spin in both classical and quantum regimes, although photons do not interact directly with electron spin. For example, it has been shown that a spin polarized photocurrent can be generated in various semiconductors under the homogeneous illumination of circularly polarized light [3]. In this case, the spin-orbit coupling splits the band spin degeneracy and the resulted optical transitions become asymmetric in momentum space and thus spin-dependent. The information of light helicity is encoded in the optically induced spin orientation. Notably, same physics rules the reverse process such that the electron spin injection into a semiconductor light emitting diode could lead to a circularly polarized light emission [4]. Furthermore, the coupling of photons with electron spin can be extended to the quantum regime when consider the interaction between single photons with quantum emitters (quantum dots, defect states etc), providing an efficient interface for the quantum information processing and conversion between optical and electronic domains [5].

1.2 Dissertation Outline

This dissertation studies the phenomena of angular momentum transfer during the process of light-matter interaction, with a focus on the roles of photon spin and electron spin. Experiments performed in three different systems are presented as follows:

Chapter 2 presents the measurement of spin angular momentum of light propagating in a silicon waveguide and the use of optical torque to actuate rotational

motion of an on-chip optomechanical device. We show the optical torque can be determined by the optical polarization states that are synthesized on the chip. The quantitative measurement on the optical torque reveals that the spin angular momentum carried by a single photon is on the order of $\hbar$.

Chapter 3 discusses the optical manipulation of surface electrons in 3D topological insulator Bi_2Se_3. Because of the optical selection rules, circularly polarized light can preferably excite the interband transitions between surface states and bulk states with their spin aligned to the optical spin. As a result, the selective optical excitation in momentum space induces a net spin-polarized photocurrent originates from surface bands with its sign being determined by light helicity. Furthermore, we present an novel optoelectronic device that integrates a TI with a silicon waveguide. Due to the spin-momentum locking in both photons and surface electrons, the device converts the path information of light into a directional photocurrent in TI.

Chapter 4 discusses the all-optical manipulation of magnetic order in ferrimagnetic materials Gd(FeCo) using sub-picosecond laser pulses as the ultrafast stimuli. The demonstrated switching process relies on the instantaneous heating of the electronic temperature and the energy and angular momentum exchange between three thermodynamic reservoirs (electron, spin and lattice). As a step towards device application, we demonstrate the first magnetic tunnel junction that can be switched all-optically without any external magnetic fields.

Chapter 5 summarizes the work presented in this dissertation along with the discussion on future studies.

Chapter 2

Measurement of Optical Spin Angular Momentum and Optical Torque in Integrated Photonic Devices

2.1 Introduction

Photons carry both linear momentum and angular momentum, which are connected respectively to the two fundamental degrees of freedom of light: frequency ω and polarization. For example, for a single photon in vacuum, the linear momentum is given by $\hbar\omega/c$, where c is the speed of light. In contrast, its spin angular momentum depends only on light polarization state: $\pm\hbar$ for right/left-handed circular polarization and is independent of ω. As a direct consequence of conservation laws, during light-matter interaction, there is linear and angular momentum transfer of photons to atoms and macroscopic objects, which gives

rise to optical force and torque, respectively [6]. However, the force and torque applied by light are extremely feeble because the linear and angular momentum of a single photon is so tiny ($\hbar$ is small and c is large), set great challenges to measure.

Historically, optical force (or radiation pressure force) was first predicted by Maxwell and then experimentally observed in 1901 [7, 8]. The first observation of optical torque effect was carried out by R. A. Beth in 1930s [1], three decades after the first measurement of radiation pressure. Beth's classic experiment was based on Poynting's prediction that circularly polarized light should exert a torque on a half waveplate when passign through it, which changes the output light helicity (as shown in Fig. 2.1). In the experiment, a half waveplate was suspended on a quartz fiber and formed a torsional pendulum. Based on the fact that a right (left) circularly polarized photon carries spin angular momentum of $\pm\hbar$, conservation of angular momentum requires each photon to transfer (receive) angular momentum of $2\hbar$ to (from) the waveplate and thus twist it. By detecting the rotation of the waveplate, Beth observed the optical torque and confirmed the angular momentum of light predicted by theory.

The mechanical effects of light can be significantly enhanced in micro- and nanophotonic devices [9–12], in which light is tightly confined to the subwavelength scale, leading to unprecedented optomechanical effects in both classical and quantum regimes. For example, there has been an explosion of interest in exploring the interaction between light and motional devices mediated by radiation pressure in various platforms over the last several years [13–16], with the most notable achievement being the backaction cooling of cavity optomechanical systems to the quantum ground state [16, 17]. However, the other essential mechanical attribute of light, the angular momentum of light, has only been utilized

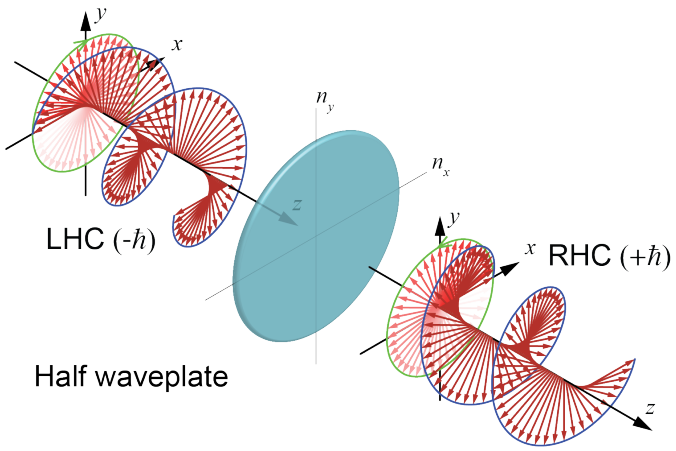

Figure 2.1: Polarization conversion in a half waveplate.

in optical tweezers [18,19] and remained unexplored in integrated optomechanical systems.

The spin angular momentum of light is important in that it directly relates to light polarization, which is an essential state variable in both classical and quantum information processing [20–22]. In integrated photonic devices, the polarization state of light is frequently manipulated so that the angular momentum exchange between photons and devices is ubiquitous [23, 24]. Understanding and using photon angular momentum-induced mechanical effects should have important implications for these areas and spawn new principles of operation.

2.2 Theory of optical torque in silicon waveguide

In our experiment, instead of using a half waveplate, we consider a rectangular silicon waveguide, which supports two modes, designated as transverse electric

(TE) and transverse magnetic (TM) mode, resembling the two orthogonal polarizations of a plane wave in vacuum. The two modes are quasi-linearly polarized with the major electric field components in x and y axis, respectively (we assume z axis is the direction of light propagation). Unlike the half waveplate made of an anisotropic material, the rectangular waveguide made of isotropic material such as silicon can have particularly strong birefringence, because of its geometric anisotropy. As a result, when the two modes are co-propagating in the waveguide with equal power, the relative phase φ between the two modes is a function of z and thus light polarization continues to evolve along the waveguide (Fig. 2.3). For example, the polarization state is quasi-linear when $\varphi = 0$ or π, and it is quasi-right (left) circular when $\varphi = \pm\pi/2$. Like the waveplate situation, accompanying the evolution between linear, elliptical, and circular polarization states is the angular momentum exchange between light and waveguide. As a result, the photons apply an optical torque pointing in the z axis on the birefringent waveguide to twist it.

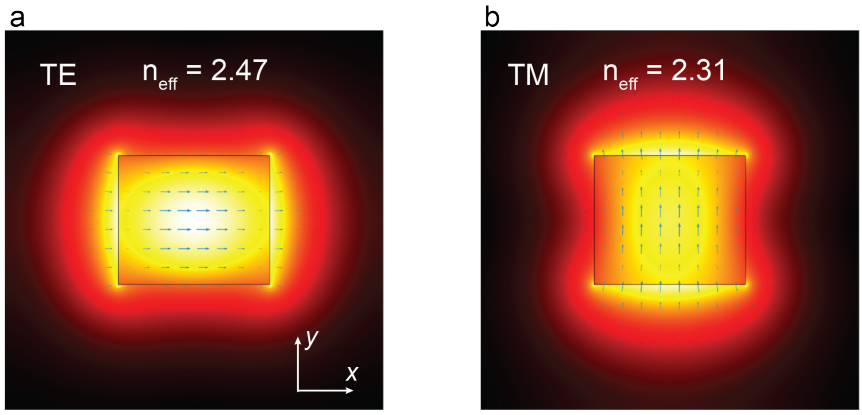

Figure 2.2: Electric field intensity and local polarization of (a) TE and (b) TM modes in a silicon waveguide suspended in air. The waveguide dimension is 400×340 nm.

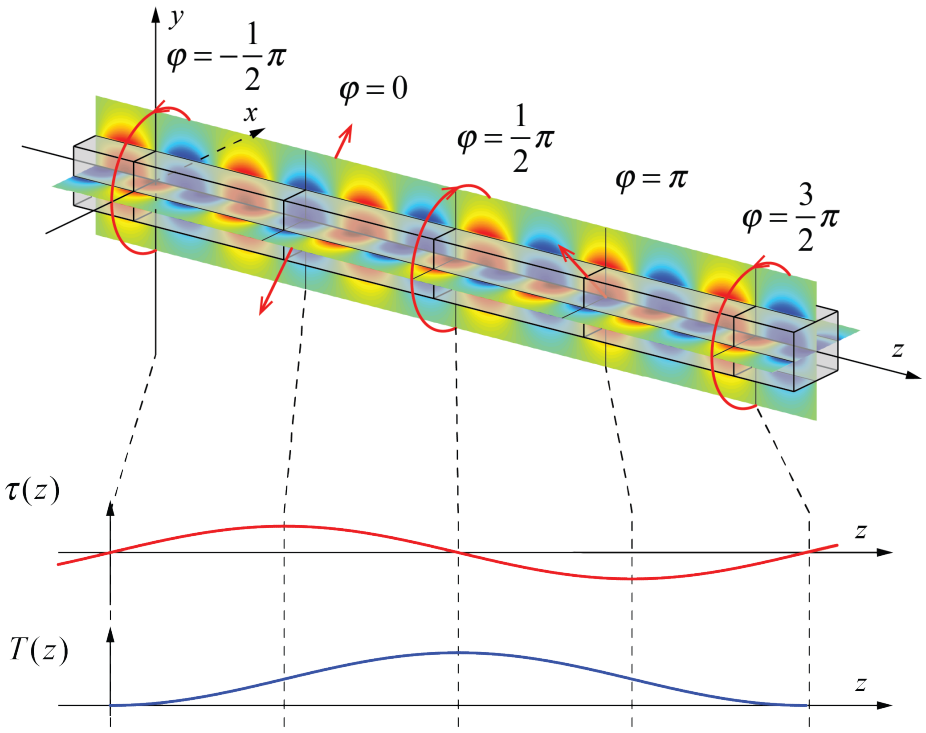

Figure 2.3: The polarization state of a hybrid mode in a silicon waveguide evolves from quasi-linear to quasi-circular and return to quasi-linear periodically along the propagation. The horizontal (vertical) plane plots the E_x (E_y) components of the TE (TM) mode.

2.2.1 Linear optical torque density

The total optical torque $T(l)$ applied on a section of waveguide with length l should be the integration of the time-averaged, local linear torque density $\tau(z)$ (torque per unit length), which varies along the waveguide as the polarization state evolves and can be expressed as

$$\langle \tau(z) \rangle = -\Phi \partial_z S_e(z) \tag{2.1}$$

where $\langle ... \rangle$ denotes time averaging, $\Phi = P/\hbar\omega$ is the photon flux and S_e is the effective spin angular momentum per photon in the waveguide. The principle is illustrated in Fig. 2.3. In more detail, when the light of arbitrary polarization state propagates along the waveguide, the electromagnetic fields generate a distributed force $f(x, y, z)$, hence a distributed torque $\tau(x, y, z)$ inside the waveguide. The integration of this distributed torque over the waveguide cross section yields the linear torque density $\tau(z)$. As will be shown later, in the case of two orthogonal modes co-propagating in a dielectric waveguide, the amplitude of linear torque density $\tau(z)$ is related to light polarization (in other words, $\tau(z)$ is a function of P_{TE}, P_{TM} , and $\varphi(z)$). This correlation between optical torque and light polarization manifests the transfer of photon spin angular momentum to dielectric media.

In general, the force exerted by electromagnetic fields on dielectric media during light-matter interaction includes dipole [6] and electrostrictive contributions [25]. Therefore, in the calculations of $S_e(z)$ and $\langle \tau(z) \rangle$, the two distinct mechanisms must be evaluated accordingly as we approached below

$$\langle \tau(z) \rangle = \left\langle \tau^d(z) \right\rangle + \langle \tau^{es}(z) \rangle = -\Phi(\partial_z S_e^d + \partial_z S_e^{es}) \tag{2.2}$$

2.2.2 Dipole contribution

The optical torque density that arises from dipole force on linear dielectric media can be written in the general form as [6]

$$\tau(\mathbf{r}) = \mathbf{r} \times [(\mathbf{P} \cdot \nabla)\mathbf{E} + \partial_t \mathbf{P} \times \mathbf{B}] + \mathbf{P} \times \mathbf{E} \tag{2.3}$$

where $\mathbf{P}$ is electric polarization. For isotropic medium such as silicon, the contribution from the internal torque $\mathbf{P} \times \mathbf{E}$ vanishes, as $\mathbf{E}$ and $\mathbf{P}$ are parallel. Furthermore, assuming optical modes with time dependence $e^{-i\omega t}$, the time-averaged

force associated with the magnetic fields $\partial_t \mathbf{P} \times \mathbf{B}$ also vanishes. The only non-vanishing term $(\mathbf{P} \cdot \nabla)\mathbf{E}$ needs to be treated with caution at dielectric interfaces where the normal components of $\mathbf{E}$ and $\mathbf{P}$ are discontinuous. Therefore, we evaluate the torque in Eq. 2.3 inside the bulk material and at the dielectric interfaces separately as follows.

The total bulk contribution is obtained by integrating Eq. 2.3 over the volume inside the dielectric medium, where both $\mathbf{E}$ and $\mathbf{P}$ are continuous

$$\mathbf{T}^{d,bulk} = \int \mathbf{r} \times (\mathbf{P} \cdot \nabla)\mathbf{E} d^3x = \frac{1}{2}\varepsilon_0(\varepsilon - 1) \int \mathbf{r} \times \nabla(\mathbf{E} \cdot \mathbf{E}) d^3x \tag{2.4}$$

where ε is the dielectric constant and we employed following identity and dropped the term involving magnetic fields,

$$(\mathbf{E} \cdot \nabla)\mathbf{E} = \frac{1}{2}\nabla(\mathbf{E} \cdot \mathbf{E}) - \mathbf{E} \times (\nabla \times \mathbf{E}) = \frac{1}{2}\nabla(\mathbf{E} \cdot \mathbf{E}) + \mathbf{E} \times \partial_t \mathbf{B} = \frac{1}{2}\nabla(\mathbf{E} \cdot \mathbf{E}) \tag{2.5}$$

Therefore, the time-averaged torque along waveguide direction (z axis) is

$$\left\langle \mathbf{T}^{d,bulk} \right\rangle = \frac{1}{4}\varepsilon_0(\varepsilon - 1) \int [x\partial_y(\mathbf{E} \cdot \mathbf{E}^*) - y\partial_x(\mathbf{E} \cdot \mathbf{E}^*)] d^3x \tag{2.6}$$

Now we consider two lowest waveguide modes with quasi-TE and TM polarization are co-propagating along z direction. The complex electric fields in the waveguide can be written as the sum of the two modes

$$\mathbf{E} = \mathbf{E}_{\mathrm{TE}}(x, y)e^{ik_{\mathrm{TE}}z} + \mathbf{E}_{\mathrm{TM}}(x, y)e^{ik_{\mathrm{TM}}z - i\varphi_0} \tag{2.7}$$

where k_{TE} and k_{TM} are the wave vectors of each mode and φ_0 is the relative phase at $z = 0$. With Eq. 2.7 it can be easily verified that the $\mathbf{E} \cdot \mathbf{E}^*$ term in Eq. 2.6 consists of four components

$$\mathbf{E} \cdot \mathbf{E}^* = \mathbf{E}_{\mathrm{TE}} \cdot \mathbf{E}^*_{\mathrm{TE}} + \mathbf{E}_{\mathrm{TM}} \cdot \mathbf{E}^*_{\mathrm{TM}} + \mathbf{E}_{\mathrm{TE}} \cdot \mathbf{E}^*_{\mathrm{TM}} e^{i\varphi(z)} + \mathbf{E}_{\mathrm{TM}} \cdot \mathbf{E}^*_{\mathrm{TE}} e^{-i\varphi(z)} \tag{2.8}$$

where $\Delta k = k_{\mathrm{TE}} - k_{\mathrm{TM}}$ and $\varphi(z) = \Delta k z + \varphi_0$. Note the first two terms in Eq. 2.8 account for the contributions due to TE and TM mode alone, whereas the cross terms are non-vanishing only when the two modes are both present. Due to the symmetry of the field distributions, the net torque induced by TE and TM modes alone should vanish and hence only the cross terms contribute. Thus Eq. 2.6 can be further written as

$$\left\langle T^{d,bulk} \right\rangle = \frac{1}{4}\varepsilon_0(\varepsilon - 1) \int [x\partial_y(\mathbf{E}_{\mathrm{TE}} \cdot \mathbf{E}^*_{\mathrm{TM}}) - y\partial_x(\mathbf{E}_{\mathrm{TE}} \cdot \mathbf{E}^*_{\mathrm{TM}})]dxdy \int e^{i\varphi(z)}dz + c.c \tag{2.9}$$

We can always set the phase of the two eigenmodes in such a way that the two transverse electric field components $(E_x, E_y)_{\mathrm{TE,TM}}$ in Eq. 2.9 are real while the longitudinal components are imaginary. Therefore, Eq. 2.9 can be written as

$$\begin{aligned} \left\langle T^{d,bulk} \right\rangle &= \int \{\frac{\varepsilon_0(\varepsilon - 1)}{2} \cos(\varphi) \int [x\partial_y(\mathbf{E}_{\mathrm{TE}} \cdot \mathbf{E}^*_{\mathrm{TM}}) - y\partial_x(\mathbf{E}_{\mathrm{TE}} \cdot \mathbf{E}^*_{\mathrm{TM}})]dxdy\}dz \\ &= \int \left\langle \tau^{d,bulk}(z) \right\rangle dz \end{aligned} \tag{2.10}$$

where the linear torque density $\left\langle \tau^{d,bulk}(z) \right\rangle$ can be obtained as

$$\left\langle \tau^{d,bulk} \right\rangle = \frac{\varepsilon_0(\varepsilon - 1)}{2} \cos(\varphi) \int [x\partial_y(\mathbf{E}_{\mathrm{TE}} \cdot \mathbf{E}^*_{\mathrm{TM}}) - y\partial_x(\mathbf{E}_{\mathrm{TE}} \cdot \mathbf{E}^*_{\mathrm{TM}})]dxdy \tag{2.11}$$

We normalized the field amplitudes to the mode powers such that $\mathbf{e} = \mathbf{E}/\sqrt{P} = \mathbf{E}/a$, then Eq. 2.11 is revised to be

$$\left\langle \tau^{d,bulk} \right\rangle = \frac{\varepsilon_0(\varepsilon - 1)}{2} \cos(\varphi)(a_{\mathrm{TE}} a_{\mathrm{TM}}) \int [x\partial_y(\mathbf{e}_{\mathrm{TE}} \cdot \mathbf{e}^*_{\mathrm{TM}}) - y\partial_x(\mathbf{e}_{\mathrm{TE}} \cdot \mathbf{e}^*_{\mathrm{TM}})]dxdy \tag{2.12}$$

Remarkably, Eq. 2.12 predicts that $\left\langle \tau^{d,bulk}(z) \right\rangle$ exhibits a sinusoidal dependence on φ and is proportional to $(a_{\mathrm{TE}} a_{\mathrm{TM}})$, which are closely related to light polarization in the waveguide. Comparing Eq. 2.12 with Eq. 2.1 shows that

the effective angular momentum per photon due to the dipole force inside the waveguide can be written as

$$S_e^{d,bulk} = -\eta^{d,bulk}\hbar\frac{2a_{\mathrm{TE}}a_{\mathrm{TM}}}{a_{\mathrm{TE}}^2 + a_{\mathrm{TM}}^2}\sin(\varphi) \tag{2.13}$$

where $\eta^{d,bulk}$ is a dimensionless coefficient

$$\eta^{d,bulk} = \varepsilon_0(\varepsilon-1)\frac{\omega}{4\Delta k}\int[x\partial_y(\mathbf{e}_{\mathrm{TE}}\cdot\mathbf{e}_{\mathrm{TM}}^*) - y\partial_x(\mathbf{e}_{\mathrm{TE}}\cdot\mathbf{e}_{\mathrm{TM}}^*)]dxdy \tag{2.14}$$

which characterizes the (effective) spin angular momentum carried by each photon in unit of $\hbar$ when $a_{\mathrm{TE}} = a_{\mathrm{TM}}$. For example, the coefficient η is equal to 1 in vacuum.

A similar procedure can be applied to evaluate the optical torque exerted on waveguide surfaces. Consider air-waveguide interface at $x = x_0$ plane, the derivative of normal electric field component (E_x) with respect to x is a delta function, which leads to the surface force density

$$\mathbf{f}^{d,surf} = (\mathbf{P}\cdot\nabla)\mathbf{E} = \frac{1}{2}\varepsilon_0(\varepsilon-1)E_{x,mat}(E_x(x_0^+) - E_x(x_0^-))\delta(x-x_0)\hat{\mathbf{x}} \tag{2.15}$$

where $E_{x,mat}$ is the x component of the electric field inside the waveguide and $\hat{\mathbf{x}}$ is the unit vector towards x axis. Eq. 2.15 accounts for a surface force density with its direction normal to the interface. The boundary condition for the normal component of $\mathbf{E}$ requires

$$\varepsilon E_{x,mat} = E_{x,air} \tag{2.16}$$

Therefore, Eq. 2.15 can be rewritten as

$$\mathbf{f}^{d,surf} = (\mathbf{n}\cdot\hat{\mathbf{x}})\frac{1}{2}\varepsilon_0(\varepsilon-1)^2E_{x,mat}^2\delta(x-x_0)\hat{\mathbf{x}} \tag{2.17}$$

where $\hat{\mathbf{n}}$ is the unit vector towards outside waveguide. The associated torque exerted on the surface $x = x_0$ is

$$T^{d,surf}(x_0) = -\int yf^{d,surf}d^3x = -(\mathbf{n}\cdot\hat{\mathbf{x}})\frac{1}{2}\varepsilon_0(\varepsilon-1)^2\int yE_{x,mat}^2(x_0)dydz \tag{2.18}$$

Using complex field expression, the time-averaged torque on surface $x = x_0$ is

$$\begin{aligned}\left\langle T^{d,surf}(x_0)\right\rangle &= \int dz\{-\mathbf{n}\cdot\hat{\mathbf{x}}\frac{1}{2}\varepsilon_0(\varepsilon-1)^2\cos(\varphi)\int yE_{x,mat,\mathrm{TE}}(x_0)E^*_{x,mat,\mathrm{TM}}(x_0)dy\}\\ &= \int\left\langle\tau^{d,surf}(z)\right\rangle dz\end{aligned} \tag{2.19}$$

where $\left\langle\tau^{d,surf}(z)\right\rangle$ can be written in terms of the normalized field amplitudes as

$$\left\langle\tau^{d,surf}(z)\right\rangle = -(\mathbf{n}\cdot\hat{\mathbf{x}})\frac{1}{2}\varepsilon_0(\varepsilon-1)^2\cos(\varphi)(a_{\mathrm{TE}}a_{\mathrm{TM}})\int ye_{x,mat,\mathrm{TE}}(x_0)e^*_{x,mat,\mathrm{TM}}(x_0)dy \tag{2.20}$$

Eq. 2.20 illustrates that optical torque on waveguide surfaces shows the same dependence $\cos(\varphi)(a_{\mathrm{TE}}a_{\mathrm{TM}})$ on light polarization as its bulk counterpart in Eq. 2.12. In comparison with Eq. 2.12 and Eq. 2.14, one can easily obtain surface linear torque density $\left\langle\tau^{d,surf}(z)\right\rangle$ and the corresponding coefficient $\eta^{d,surf}$ on surface $x = x_0$. Similarly, the contributions from other surfaces can be evaluated accordingly. Therefore, the total linear torque density that arises from dipole force simply reads

$$\left\langle\tau^{d}(z)\right\rangle = \left\langle\tau^{d,bulk}(z)\right\rangle + \left\langle\tau^{d,surf}(z)\right\rangle \tag{2.21}$$

2.2.3 Electrostriction

For isotropic materials and for cubic crystals (such as silicon), the electrostrictively-induced stress is related to the optical fields as [25]

$$\langle\sigma^{es}_{kl}\rangle = -\frac{1}{4}\varepsilon_0 n^4 p_{ijkl}\mathrm{Re}(E_iE^*_j) \tag{2.22}$$

where p_{ijkl} is the photoelastic tensor. The force density is calculated from the stress tensor as

$$\langle f^{es}_i\rangle = -\partial_j\left\langle\sigma^{es}_{ji}\right\rangle \tag{2.23}$$

Similar to the dipole force, due to the discontinuity of $\langle \sigma_{kl}^{es} \rangle$ at the material boundaries, $\langle f_i^{es} \rangle$ needs to be evaluated inside the material and at the dielectric interfaces separately. All of the stress components that are related to torque calculation are listed below

$$
\begin{aligned}
\langle \sigma_{xx}^{es} \rangle &= -\frac{1}{4}\varepsilon_0 n^4 \big(p_{11}|E_x|^2 + p_{21}|E_y|^2 + p_{31}|E_z|^2 \big) \\
&= -\frac{1}{4}\varepsilon_0 n^4 \big(p_{11}E_{x,\mathrm{TE}}E_{x,\mathrm{TM}} + p_{21}E_{y,\mathrm{TE}}E_{y,\mathrm{TM}} + p_{31}E_{z,\mathrm{TE}}E_{z,\mathrm{TM}} \big) e^{i\varphi} + c.c. \\
\langle \sigma_{xy}^{es} \rangle &= \langle \sigma_{yx}^{es} \rangle = -\frac{1}{4}\varepsilon_0 n^4 p_{66} \big(E_x E_y^* + E_y E_x^* \big) \\
&= -\frac{1}{4}\varepsilon_0 n^4 p_{66} \big(E_{x,\mathrm{TE}}E_{y,\mathrm{TM}} + E_{x,\mathrm{TM}}E_{y,\mathrm{TE}} \big) e^{i\varphi} + c.c. \\
\langle \sigma_{zx}^{es} \rangle &= -\frac{1}{4}\varepsilon_0 n^4 p_{55} \big(E_z E_x^* + E_x E_z^* \big) \\
&= -\frac{1}{4}\varepsilon_0 n^4 p_{55} \big(iE_{z,\mathrm{TE}}E_{x,\mathrm{TM}} - iE_{z,\mathrm{TM}}E_{x,\mathrm{TE}} \big) e^{i\varphi} + c.c. \\
\langle \sigma_{yy}^{es} \rangle &= -\frac{1}{4}\varepsilon_0 n^4 \big(p_{12}|E_x|^2 + p_{22}|E_y|^2 p_{32}|E_z|^2 \big) \\
&= -\frac{1}{4}\varepsilon_0 n^4 \big(p_{12}E_{x,\mathrm{TE}}E_{x,\mathrm{TM}} + p_{22}E_{y,\mathrm{TE}}E_{y,\mathrm{TM}} + p_{32}E_{z,\mathrm{TE}}E_{z,\mathrm{TM}} \big) e^{i\varphi} + c.c. \\
\langle \sigma_{zy}^{es} \rangle &= -\frac{1}{4}\varepsilon_0 n^4 p_{44} \big(E_y E_z^* + E_z E_y^* \big) \\
&= -\frac{1}{4}\varepsilon_0 n^4 p_{44} \big(-iE_{y,\mathrm{TE}}E_{z,\mathrm{TM}} + iE_{y,\mathrm{TM}}E_{z,\mathrm{TE}} \big) e^{i\varphi} + c.c.
\end{aligned}
\tag{2.24}
$$

Therefore, the corresponding electrostrictive force and torque density inside the silicon waveguide are

$$\begin{aligned}
\left\langle f_x^{es,bulk}\right\rangle &= -\frac{\partial\left\langle\sigma_{xx}^{es}\right\rangle}{\partial x} - \frac{\partial\left\langle\sigma_{yx}^{es}\right\rangle}{\partial y} - \frac{\partial\left\langle\sigma_{zx}^{es}\right\rangle}{\partial z} \\
&= \frac{1}{2}\varepsilon_0 n^4\big[\frac{\partial}{\partial x}(p_{11}E_{x,\mathrm{TE}}E_{x,\mathrm{TM}} + p_{21}E_{y,\mathrm{TE}}E_{y,\mathrm{TM}} + p_{31}E_{z,\mathrm{TE}}E_{z,\mathrm{TM}}) \\
&+ \frac{\partial}{\partial y}(p_{66}E_{x,\mathrm{TE}}E_{y,\mathrm{TM}} + p_{66}E_{x,\mathrm{TM}}E_{y,\mathrm{TE}}) \\
&+ \Delta k(-p_{55}E_{z,\mathrm{TE}}E_{x,\mathrm{TM}} + p_{55}E_{z,\mathrm{TM}}E_{x,\mathrm{TE}})\big]\cos(\varphi) \\
\left\langle f_y^{es,bulk}\right\rangle &= -\frac{\partial\left\langle\sigma_{xy}^{es}\right\rangle}{\partial x} - \frac{\partial\left\langle\sigma_{yy}^{es}\right\rangle}{\partial y} - \frac{\partial\left\langle\sigma_{zy}^{es}\right\rangle}{\partial z} \\
&= \frac{1}{2}\varepsilon_0 n^4\big[\frac{\partial}{\partial x}(p_{66}E_{x,\mathrm{TE}}E_{y,\mathrm{TM}} + p_{66}E_{x,\mathrm{TM}}E_{y,\mathrm{TE}}) \\
&+ \frac{\partial}{\partial y}(p_{12}E_{x,\mathrm{TE}}E_{x,\mathrm{TM}} + p_{22}E_{y,\mathrm{TE}}E_{y,\mathrm{TM}} + p_{32}E_{z,\mathrm{TE}}E_{z,\mathrm{TM}}) \\
&+ \Delta k(p_{44}E_{y,\mathrm{TE}}E_{z,\mathrm{TM}} - p_{44}E_{y,\mathrm{TM}}E_{z,\mathrm{TE}})\big]\cos(\varphi) \\
\left\langle\tau^{es,bulk}(\mathbf{r})\right\rangle &= x\left\langle f_y^{es,bulk}\right\rangle - y\left\langle f_x^{es,bulk}\right\rangle
\end{aligned} \tag{2.25}$$

The corresponding electrostrictive force and torque density on the silicon waveguide surface can be expressed in a similar way. The main feature of electrostrictively-induced linear torque density is the same sinusoidal dependence on φ, as shown in Eq. 2.25. Therefore, a similar set of quantities such as S_e^{es} and η^{es} can be derived from them.

By summing up the optical torque from dipole and electrostrictive contributions, we obtained the final expressions for total linear torque density and the effective spin angular momentum of photon in the waveguide as

$$\tau(z) = -\Phi\partial_z S_e = \eta\frac{\Delta k}{\omega}(2a_{\mathrm{TE}}a_{\mathrm{TM}})\cos(\varphi) \tag{2.26}$$

$$S_e(\varphi) = -\eta\hbar\frac{2a_{\mathrm{TE}}a_{\mathrm{TM}}}{a_{\mathrm{TE}}^2 + a_{\mathrm{TM}}^2}\sin(\varphi) \tag{2.27}$$

where the value of η can be determined numerically.

2.2.4 Numerical calculations

Having derived the expression for the optical torque density resulted from the two distinct effects, we proceed to calculated the optical torque in a suspended silicon waveguide. We consider a silicon waveguide with 400 nm in width and 340 nm in height, surrounded by air. Figure 2.4 illustrates the torque density profiles inside the waveguide when the two modes are in phase ($\varphi = 0$) and equal in power ($a_{\mathrm{TE}} = a_{\mathrm{TM}}$).

Figure 2.5 depicts the non-vanishing surface torque density on the air-waveguide interfaces for both dipole and electrostrictive effects due to the discontinuity of normal electric field and stress tensor across the boundaries.

To explore the dependence of optical torque on waveguide geometry, we calculate the coefficient η for waveguides with various width. As shown in Fig. 2.6, the effective spin angular momentum η various slightly as the waveguide width increases. Furthermore, the dipole (η^d) and electrostrictive contribution (η^{es}) to the optical torque are of the similar magnitude.

2.3 Torsional cavity optomechanical oscillator

To measure the feeble optical torque and demonstrate the transfer of optical angular momentum, we designed and fabricated a nano-optomechanical device on silicon-on-insulator wafer. As shown in Fig. 2.7(a), the core element of the device is a portion of rectangular waveguide that is released from the substrate. The geometry of the waveguide (400 nm wide and 340 nm high) is designed to have

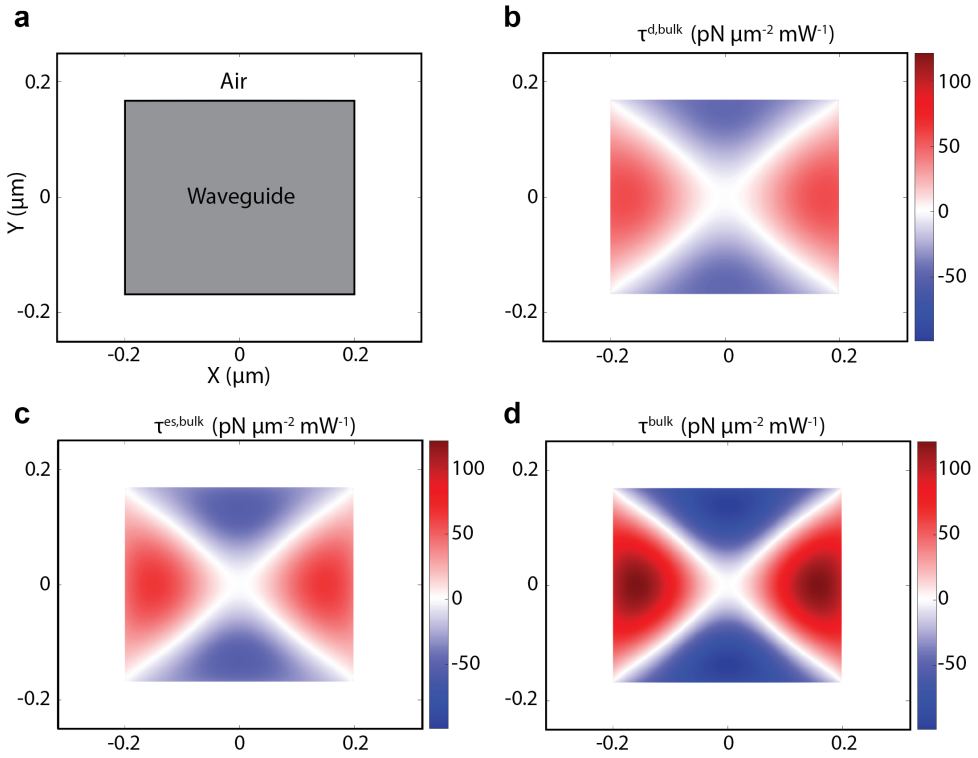

Figure 2.4: Simulated torque density distributions inside a silicon waveguide (bulk contribution) suspended in air. (a) The waveguide geometry is 400 nm wide and 340 nm high. (b)-(d) Torque density distributions due to (b) dipole force, (c) electrostrictive force and (d) the sum of the two.

strong geometric birefringence for the fundamental TE and TM modes with effective index difference $\Delta n = 0.16$. Attached to the waveguide and also suspended from the substrate is a nanobeam in which two one-dimensional photonic crystal nanocavities [26] are embedded, one on each side. The resonance modes of the nanocavities are optimized to be particularly sensitive to their distance from the substrate. Thus, they provide very sensitive detection to the rotation of the waveguide actuated by the optical torque. One of the nanocavities is coupled

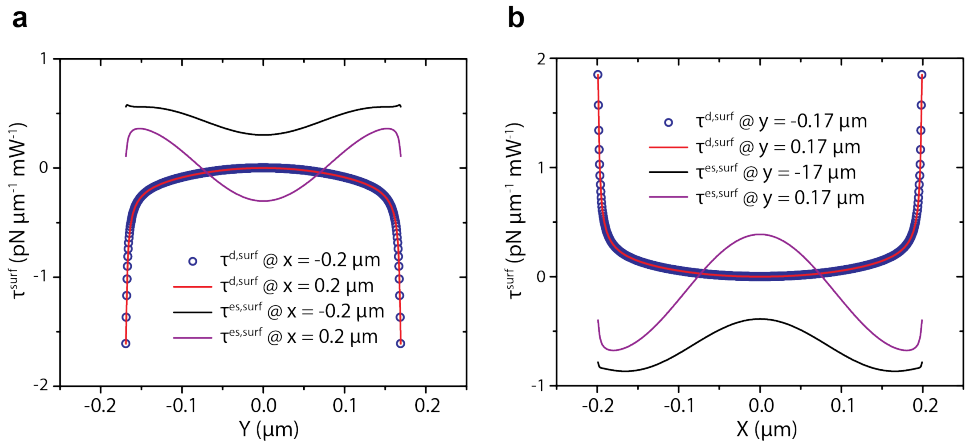

Figure 2.5: Simulated surface torque density distributions along waveguide surfaces.

to a nearby waveguide. Therefore, the torsional motion of the mechanical see-saw oscillator is transduced into the shift of the optical resonance peaks, which can be read out through the coupling waveguide. Such an optomechanical oscillator with simultaneously high mechanical and optical quality factors enables ultra-high measurement sensitivity and is the key for the following optical torque measurement.

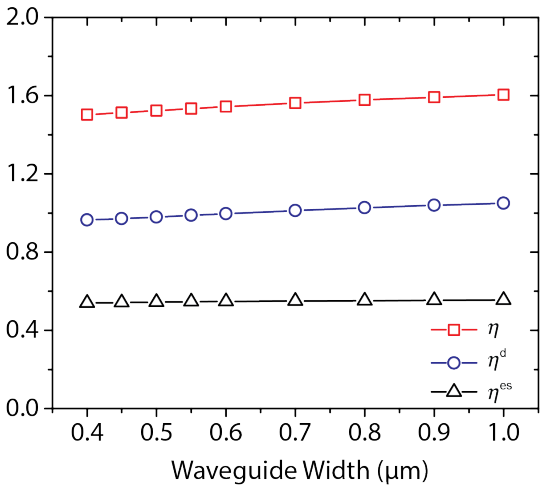

Figure 2.6: Simulated coefficient η for waveguides with various width and fixed height of 340 nm.

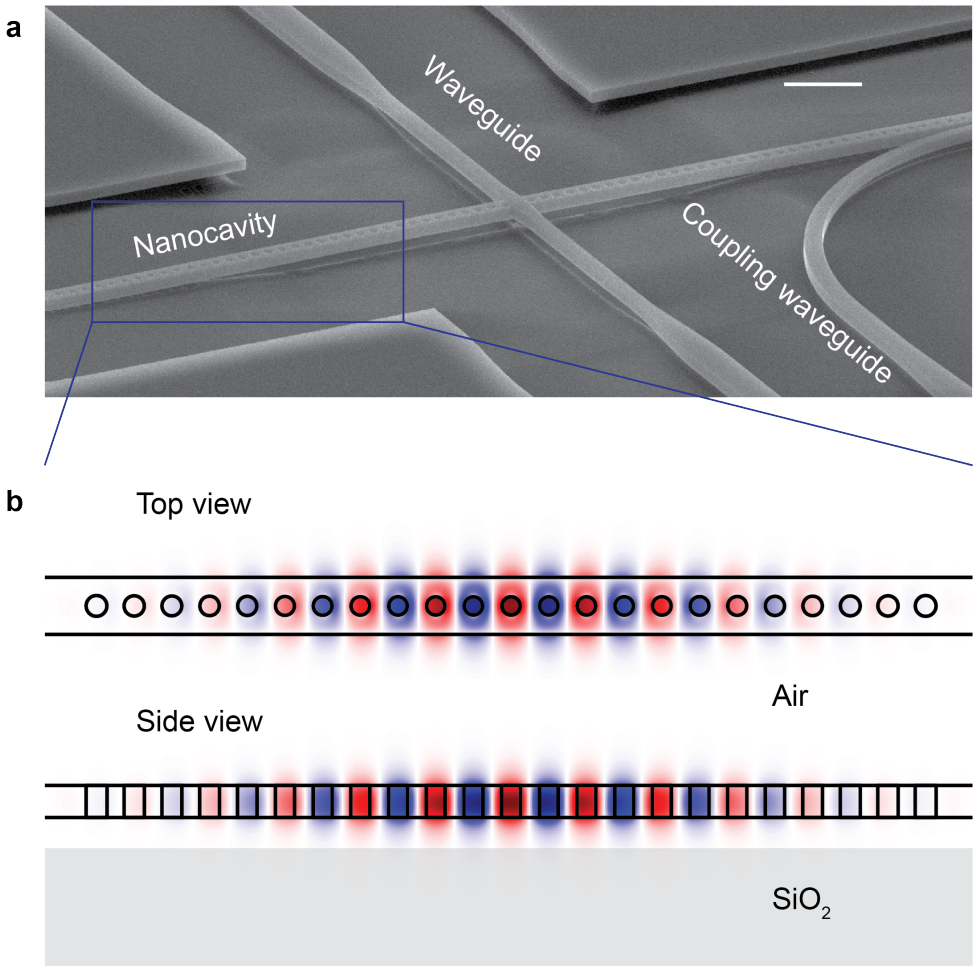

Figure 2.7: Torsional optomechanical oscillator. (a) SEM image of the suspended waveguide-nanobeam structure. (b) Simulated optical mode profile of the photonic crystal nanocavity. Scale bar, 2 µm.

2.3.1 Effective torsional simple harmonic oscillator model

We use Finite Element Method (COMSOL Multiphysics) to simulate the mechanical resonances of the waveguide-nanobeam structure. In the simulation, the two ends of the waveguide are clamped while the nanobeam hinged on the waveguide is free to rotate. Four prominent mechanical modes are revealed with the resonant frequencies below $\sim 1\,\mathrm{MHz}$. They are, with increasing frequency, the out-of-plane torsional mode, out-of-plane flapping mode, in-plane torsional mode, and in-plane flapping mode. Figure 2.8 shows the simulated mechanical mode profiles of the waveguide-nanobeam structure. The resonance frequencies of the four mechanical modes for various suspended waveguide lengths are summarized in Table. 2.1.

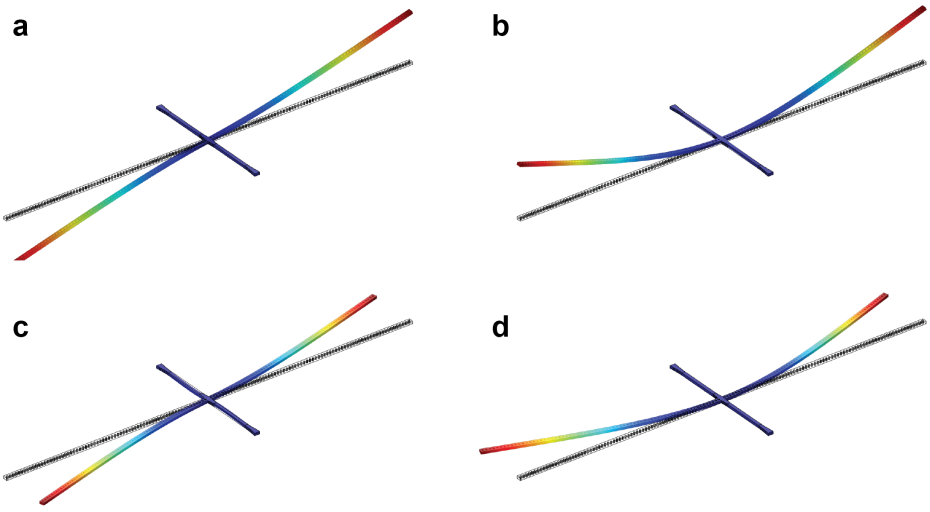

Figure 2.8: Simulated mechanical mode profiles of the suspended silicon waveguide-nanobeam structure. (a) Fundamental (first order) out-of-plane torsional (anti-symmetric) mode. (b) Fundamental (first order) out- of-plane flapping (symmetric) mode. (c) Fundamental (first order) in-plane torsional (anti-symmetric) mode. (d) Fundamental (first order) in-plane flapping (symmetric) mode.

l µm	9.0	10.5	12	13.5	15	16.5	18
OT (kHz)	378.6	362.6	348.2	335.3	323.9	313.5	304.0
OF (kHz)	497.8	497.5	497.0	496.4	495.6	494.6	493.5
IT (kHz)	911.3	886.2	862.0	838.9	817.1	796.5	777.2
IF (kHz)	1040.6	1040.6	1040.6	1040.6	1040.6	1040.6	1040.6

Table 2.1: Simulated four lowest mechanical resonances for devices with various suspended waveguide lengths l. O, out-of-plane; I, in-plane; T, torsional mode; F, flapping mode.

In the following optical torque measurement, we will only focus on the fundamental out-of-plane torsional mode (Fig. 2.8(a)), in which the waveguide undergoes pure torsional motion with its two ends fixed while the nanobeam tilts with it. This fundamental mechanical mode can be modeled as a torsional simple harmonic oscillator (SHO), whose equation of motion is

$$I_e\partial_t^2\theta(t) + \frac{\sqrt{I_e\kappa_e}}{Q}\partial_t\theta(t) + \kappa_e\theta(t) = T_e(t) \tag{2.28}$$

where $\theta(t)$ is the instantaneous mode displacement in terms of rotation angle, I_e is the effective moment of inertia, κ_e is the effective torsional spring constant, Q is the mechanical quality factor, and $T_e(t)$ is the effective driving torque. Note that the definition of $\theta(t)$ in the equation of motion can be arbitrary as the rotation angle at each point on the waveguide-nanobeam structure varies (for example, $\theta(t)$ is maximum at $z = 0$ and decreases to 0 at the two fixed ends). Nevertheless, we choose to define as the rotation angle at the center of the nanobeam. Furthermore, I_e, κ_e and the mode frequency f_0 can be calculated using

$$\begin{aligned} U_k(t) &= \frac{1}{2}I_e(\partial_t\theta)^2 \\ U_p(t) &= \frac{1}{2}\kappa_e\theta^2 \\ f_0 &= \frac{\sqrt{\kappa_e/I_e}}{2\pi} \end{aligned} \tag{2.29}$$

where $U_k(t)$ and $U_p(t)$ are, respectively, the simulated instantaneous kinetic and potential energy. The simulated parameters of the effective torsional SHO are summarized in table 2.2.

l µm	9.0	10.5	12	13.5	15	16.5	18
I_e(ng $\cdot$ µm^2)	30.63	24.84	21.09	18.51	16.65	15.25	14.16
κ_e (pN $\cdot$ µm $\cdot$ µrad^{-1})	173.3	128.9	101.0	82.19	68.95	59.17	51.66
f_0 (kHz)	378.6	362.6	348.2	335.3	323.9	313.5	304.0

Table 2.2: Simulated parameters of the effective torsional simple harmonic oscillator.

2.3.2 Calibration of system's measurement sensitivity

In thermal equilibrium, the mechanical oscillator is in Brownian motion (thermal fluctuation) and the measurement of the thermomechanical noise in frequency domain can be utilized to calibrate the system's measurement sensitivity [27]. In the section we will derive how the power spectral density (PSD) of the thermomechanical noise is related to the mechanical properties of the torsional simple harmonic oscillator (spring constant κ_e, moment of inertia I_e, damping coefficient C, etc.).

In a real experiment, we can only measure the rotation of a torsional mechanical oscillator $\theta(t)$ within a finite time interval T. We define the gated Fourier transform of $\theta(t)$ as [13]

$$\theta(\omega) = \frac{1}{\sqrt{T}} \int_0^T \theta(t) e^{i\omega t} dt \tag{2.30}$$

and the power spectral density $S_{\theta\theta} = \left\langle |\theta(\omega)|^2 \right\rangle$ as the average of $|\theta(\omega)|^2$ over many independent measurements. Moreover, according to the Wiener-Khinchin theorem, the power spectral density is related to the Fourier transform of the

correlation function $R_{\theta\theta}(t) = \langle\theta(0)\theta(t)\rangle$ as

$$R_{\theta\theta}(0) = \left\langle\theta^2(t)\right\rangle = \frac{1}{2\pi}\int_{-\infty}^{\infty} S_{\theta\theta}(\omega)d\omega \tag{2.31}$$

We note the expected value of the potential energy of the harmonic oscillator $\langle U_p(t)\rangle$ is half of its total energy and can be written as

$$\langle U_p(t)\rangle = \left\langle\frac{1}{2}\kappa_e\theta^2(t)\right\rangle = \frac{1}{2}\frac{\hbar\omega_0}{e^{\hbar\omega_0/k_BT}-1} \tag{2.32}$$

where ω_0 is the angular frequency of the mechanical resonance of interest, k_B is the Boltzmann constant and T is the lab temperature. In the low energy limit ($\hbar\omega_0 \ll k_BT$), Eq. 2.32 can be further simplified as

$$\langle U_p(t)\rangle = \left\langle\frac{1}{2}\kappa_e\theta^2(t)\right\rangle = \frac{1}{2}k_BT \tag{2.33}$$

Substituting Eq. 2.31 into Eq. 2.33 yields

$$\frac{1}{2}k_BT = \frac{1}{2}\kappa_e R_{\theta\theta}(0) = \frac{\kappa_e}{4\pi}\int_{-\infty}^{\infty} S_{\theta\theta}(\omega)d\omega \tag{2.34}$$

We assume the driving torque $T_e(t)$ (right hand side of Eq. 2.28) due to thermal excitation is a white noise with a constant power spectral density $S_{TT}(\omega) = \sigma^2$, therefore, the power spectral density of $\theta(t)$ can be written as

$$S_{\theta\theta}(\omega) = |H(\omega)|^2 S_{TT}(\omega) = \frac{\sigma^2}{(\kappa_e - \omega^2 I_e)^2 + \omega^2 C^2} \tag{2.35}$$

where $H(\omega) = \frac{1}{(\kappa_e-\omega^2 I_e)^2+\omega^2C^2}$ is the transfer function and $C = \frac{\sqrt{I_e\kappa_e}}{Q}$ is the damping coefficient of the harmonic oscillator. Substituting Eq. 2.35 back into Eq. 2.34, we have

$$\frac{1}{2}k_BT = \frac{\kappa_e\sigma^2}{4\pi}\int_{-\infty}^{\infty}\frac{1}{(\kappa_e - \omega^2 I_e)^2 + \omega^2 C^2}d\omega = \frac{\kappa_e\sigma^2}{4\omega_0^2 C I_e} \tag{2.36}$$

where we have used the following equation that holds when the damping coefficient is small

$$\int_{-\infty}^{\infty}\frac{1}{(\kappa_e - \omega^2 I_e)^2 + \omega^2 C^2}d\omega = \frac{\pi}{\omega_0 C I_e} \tag{2.37}$$

Thus, from Eq. 2.36, the PSD of the thermal excitation σ^2 is

$$\sigma^2 = 2k_B TC \tag{2.38}$$

Substituting Eq. 2.38 back into Eq. 2.35 gives the expression for $S_{\theta\theta}(\omega)$ in terms of the characteristics of the mechanical oscillator

$$S_{\theta\theta}(\omega) = \frac{2k_B TC}{(\kappa_e - \omega^2 I_e)^2 + \omega^2 C^2} \tag{2.39}$$

In our experiment, the rotation of the nanobeam is transduced by the coupling waveguide and the photodetector into a voltage signal $V(t)$ and measured by a spectral analyzer (SA). We define the transduction factor G such that

$$V(t) = G\theta(t) \tag{2.40}$$

The transduction factor G is determined by the optomechanical coupling of the nanocavity, the optical resonance line shape etc. Therefore, the PSD measured by the SA is

$$S_{VV}(\omega) = G^2 \frac{\frac{k_B T}{\sqrt{I_e \kappa_e} Q}}{(\omega - \omega_0)^2 + (\frac{\omega_0}{2Q})^2} \tag{2.41}$$

which is used for the curve fitting to obtain f_0, Q and G.

2.3.3 Effective torque

When an arbitrary time-varying external force density $\mathbf{f}$(r,t) is applied on the structure, the effective driving torque $T_e(t)$ on the right hand side of the equation of motion (Eq. 2.28) should be calculated as the overlap integral between $\mathbf{f}(\mathbf{r}, t)$ and $\mathbf{u}_n(\mathbf{r}, t)$ [13, 28], where $\mathbf{u}_n(\mathbf{r}, t)$ is the normalized mechanical mode profile. In our case, $\mathbf{f}$(r,t) is exerted by the guided optical modes inside the waveguide, hence is negligible inside the nanobeam. Therefore

$$T_e(t) = \int_{\text{waveguide}} \mathbf{f}(\mathbf{r}, t) \cdot \mathbf{u}_n(\mathbf{r}) d^3x \tag{2.42}$$

Because the waveguide undergoes pure torsional motion,

$$\mathbf{u}_n(\mathbf{r}) \approx (\hat{\mathbf{z}} \times \mathbf{r})\theta_n(z) \tag{2.43}$$

where $\theta_n(z)$ is the normalized rotation angle of the waveguide. Therefore, the effective torque can be written as

$$T_e(t) \approx \int_{\text{waveguide}} \mathbf{f}(\mathbf{r},t) \cdot (\hat{\mathbf{z}}) \times \mathbf{r})\theta_n(z) d^3x = \int_{\text{waveguide}} \tau_z(\mathbf{r},t)\theta_n(z) d^3x \tag{2.44}$$

which can be further simplified as

$$T_e(t) \approx \int \left[\int \tau_z(\mathbf{r},t) dxdy \right] \theta_n(z) dz \approx \int \tau(z,t)\theta_n(z) dz \tag{2.45}$$

In order to derive a closed-form expression for $T_e(t)$, we approximate the waveguide cross-section as a perfect rectangular waveguide with a constant size. Therefore, substituting Eq. 2.26 for $\tau(z,t)$ yields

$$T_e(t) \approx \eta(\Delta k/\omega)(2a_{\text{TE}}a_{\text{TM}}) \int_{-l/2}^{l/2} \cos\left(\varphi(z,t)\right)\theta_n(z) dz \tag{2.46}$$

and l is the total suspended waveguide length.

In our experiment, we sinusoidally modulate $\varphi(z,t)$, so we explicitly express its time-dependence in Eq. 2.46 and in the following derivations. Note $\varphi(z,t) = \varphi_0(t) + \Delta k z$, the integrand in Eq. 2.46 can be expanded as

$$\cos\left(\varphi_0(t)\right)\cos\left(\Delta k z\right)\theta_n(z) - \sin\left(\varphi_0(t)\right)\sin\left(\Delta k z\right)\theta_n(z) \tag{2.47}$$

where the first term is an even function of z, while the second term is an odd function of z, hence has no contribution to the integral, because $\theta_n(z)$ is an even function. Consequently the expression for $T_e(t)$ can be further simplified as

$$T_e(t) \approx T_m \cos\left(\varphi_0(t)\right) \tag{2.48}$$

where

$$T_m = \eta(\Delta k/\omega)(2a_{\mathrm{TE}}a_{\mathrm{TM}})2\int_0^{l/2}\cos(\Delta kz)\theta_n(z)dz \tag{2.49}$$

Therefore, the effective torque T_e changes sinusoidally with φ_0 and reaches extrema when φ_0 is equal to 0 or π. The maximal effective torque T_m depends on the waveguide length and birefringence. To further simplify the expression of T_m, we approximate $\theta_n(z)$ as a triangular function

$$\theta_n(z) \approx \begin{cases} 1-|2z/l| & \text{when } |z| < l/2 \\ 0 & \text{otherwise} \end{cases} \tag{2.50}$$

By substituting Eq. 2.50 into Eq. 2.49, we solve the integral by parts and obtain the final closed-form expression of T_m as

$$T_m \approx \eta\frac{2a_{\mathrm{TE}}a_{\mathrm{TM}}}{\omega}\left[\frac{2\sin^2(\Delta k/4)}{\Delta kl/4}\right] = -S_e\frac{\pi}{2}\Phi\left[\frac{2\sin^2(\Delta k/4)}{\Delta kl/4}\right] \tag{2.51}$$

where S_e and Φ are the effective photon spin angular momentum and the photon flux defined previously.

2.4 Controlling optical torque through synthesis of light polarization state

As derived previously, the transfer of spin angular momentum and the resulted optical torque effect can be understood as the variation of light polarization along its propagation in the waveguide. Therefore, both the sign and the magnitude of the optical torque can be controlled by varying light polarization inside the waveguide, namely the power ratio between TE and TM modes as well as their relative phase $(a_{\mathrm{TE}}, a_{\mathrm{TM}}, \varphi)$, as suggested by Eq. 2.26. This is achieved with the on-chip peripheral photonic circuits (Fig. 2.9(a)) and off-chip setup. Figure 2.9

shows the schematics of the experiment setup and device layout. The TE and TM modes are both derived from the same laser source with their power ratio controlled by a fiber polarization controller (FPC1). The sinusoidally varying phase is applied through an electro-optic modulator (EOM), after which the two modes are separated into two optical paths by a fiber polarization beam splitter (PBS) and then coupled into silicon waveguide through TE and TM grating couplers (GCs), respectively. Since accurate control of the relative phase is crucial in our experiment, we also fabricated an on-chip interferometer next to the GCs to monitor the relative phase φ_{I}, the output of which was utilized as the feedback to compensate any low frequency phase fluctuations introduced in the optical fibers due to small temperature variation in the environment. Although the actual difference between φ_{I} and φ_0 cannot be practically predetermined by design, the difference $\varphi_0 - \varphi_{\mathrm{I}}$ remains consistent for any single device at a stabilized temperature. Therefore, the one-to-one correspondence between φ_0 and φ_{I} allows the measurement of phase dependence of the optical torque in the waveguide. Figure 2.9(b) is a representative transmission spectrum of the photonic crystal nanocavities through the side-coupled waveguide, showing the resonance of the nanocavity with a loaded (intrinsic) quality factor of 4200 (23,000). To avoid air damping, the sample was placed in the vacuum chamber with a pressure below 10^{-4} torr. All measurements were performed at room temperature with the temperature fluctuation less than $\pm 0.2\,\mathrm{K}$.

2.5 Optical torque modulation and measurement

To measure the optical torque, we employed the resonance method similar to Beth's original experiment but in a modern fashion, by modulating the optical

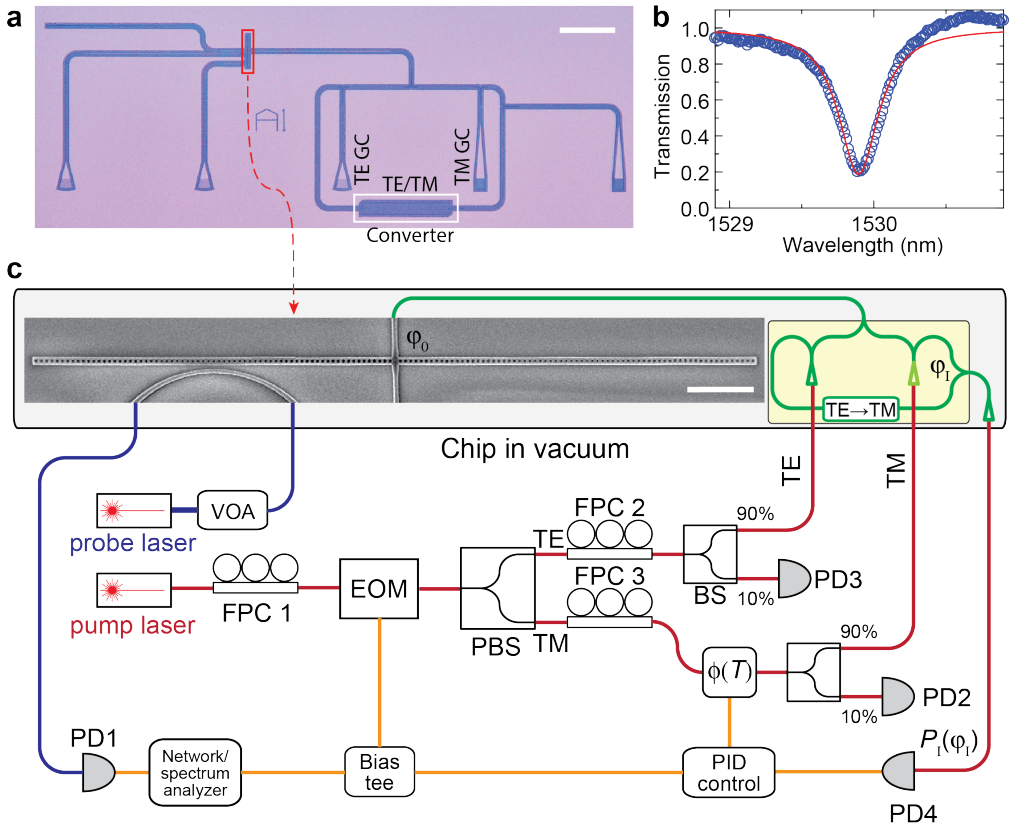

Figure 2.9: Schematics of the experimental setup and device layout. (a) Optical microscope image of the integrated photonic device include the suspended waveguide-nanobeam structure (in the red box) and the interferometer with a TE-to-TM mode convertor (in the white box) for phase stabilization. Scale bar, 100 µm. (b) Optical transmission spectrum of the photonic crystal nanocavity. (c) Schematics of the measurement system. FPC, fiber polarization controller; EOM, electro-optic modulator; PBS, polarization beam splitter; BS, beam splitter; PD, photodetector; VOA, variable optical attenuator; $\phi(T)$, fiber thermo-optic phase shifter.

torque to excite the resonant motion of the nanobeam hinged on the waveguide. When performing resonance measurement, the electro-optic modulator is driven by a network analyzer to sinusoidally modulate the phase φ_0 by a small amplitude $\delta\varphi_0$ and thus generate a dynamic effective torque

$$\delta T_e \cos(\Omega t) = -T_m \sin(\varphi_0)\delta\varphi_0 \cos(\Omega t) \tag{2.52}$$

where Ω is the modulation frequency. By performing only phase modulation and avoiding amplitude modulation, the photothermal effect is minimized [15, 29, 30]. Additionally, the structural symmetry of the device and the large gap between the waveguide and the substrate eliminate the "light-pressure torque" effect [1], although a small residual amplitude modulation might remain because of instrumental nonideality.

2.5.1 Mechanical characteristics of torsional optomechanical device

To characterize the mechanical properties of the suspended optomechanical oscillator and calibrate system's sensitivity, we measured the thermomechanical noise PSD for devices with various suspended waveguide lengths. In the experiment, the pump laser is off and the probe laser is sufficiently attenuated to avoid dynamic cavity optomechanical backaction and optimally detuned from the nanocavity resonance to transduce the torsional motion [31]. Figure 2.10(a) shows the noise PSD measured from the transmitted probe laser power for a representative device with $l = 10.5\,\mu\text{m}$. Four mechanical resonance peaks due to the thermomechanical excitations are observed, with the peak at 358.7 kHz corresponding to the fundamental torsional mode (Fig. 2.10(d)), showing a mechanical quality factor of 12,000. The

measured fundamental resonance frequencies of seven devices with various waveguide lengths l (9.0, 10.5, 12.0, 13.5, 15.0, 16.5, and 18.0 µm) are summarized in Fig. 2.10(c). The results agree well with the simulation results (purple line) using an elasticity matrix for silicon that is 19% lower than the typical value for bulk silicon (red line) [32].

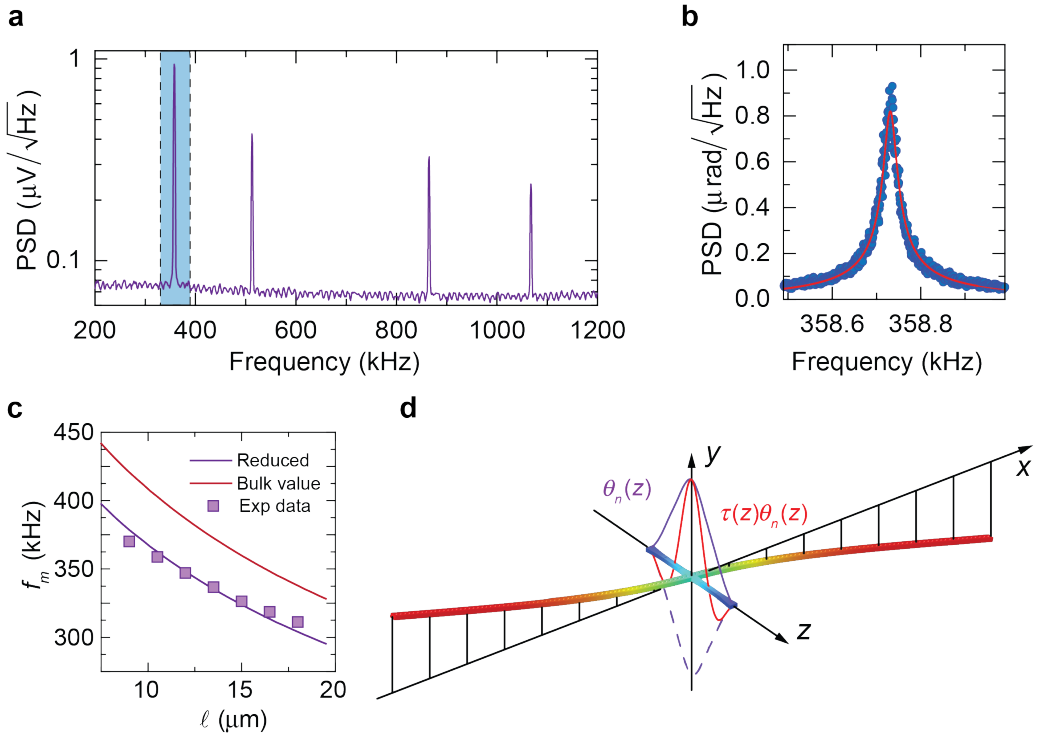

Figure 2.10: Mechanical characteristics of the waveguide-nanobeam optomechanical oscillator. (a) Measured noise PSD to calibrate the system sensitivity. The observed four prominent peaks correspond to the fundamental out-of-plane torsional mode, out-of-plane flapping mode, in-plane torsional mode and in- plane flapping mode with increasing frequencies. (b) Zoon-in view of the fundamental torsional mode with the resonance frequency of 358.7 kHz and a quality factor of 12,000. (c) The fundamental torsional resonance frequencies for devices with various suspended waveguide lengths. (d) Simulated mode profile of the fundamental torsional mode. Also plotted in yz plane is the angular mode profile $\theta_n(z)$ and its overlap integral with the linear optical torque density $\tau(z)$.

2.5.2 Phase dependence

We first measure the phase dependence of the optical torque by varying φ_0 while keep other parameters such as $\delta\varphi_0$ and laser power ($P_{\mathrm{TE}} = P_{\mathrm{TM}}$, $P = P_{\mathrm{TE}} + P_{\mathrm{TM}} = 95\,\mu\mathrm{W}$) being constant. The quadrature components of the response from a representative device with $l = 10.5\,\mu\mathrm{m}$ are plotted in Fig. 2.11(a), showing the fundamental torsional mode is excited by the optical torque. In particularly, the data measured for six different values of φ_0 reveals that both the magnitude and the sign of the response depend on φ_0. Moreover, from the response for each value of φ_0, $\delta T_e/\delta\varphi_0$ is calculated and plotted in Fig. 2.11(b), showing a clear sinusoidal dependence as predicted by $-T_m \sin(\varphi_0)$ term in Eq. 2.52. The value of T_m can also be extracted from Fig. 2.11(b).

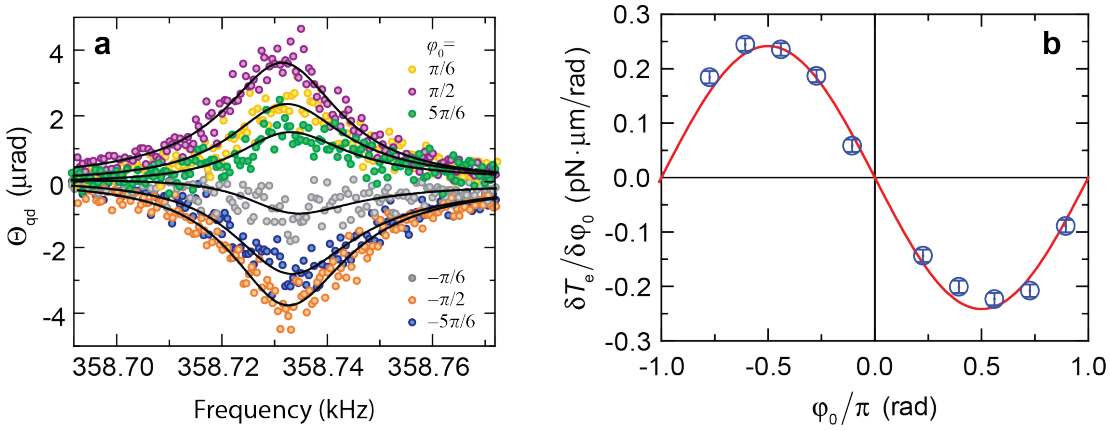

Figure 2.11: Dependence of optical torque on the relative phase. (a) The quadrature components of the responses of the device with $l = 10.5\,\mu\mathrm{m}$ for various φ_0. The total optical power in the waveguide is kept at $95\,\mu\mathrm{W}$ with $P_{\mathrm{TE}} = P_{\mathrm{TM}}$. (b) Measured effective driving torque over the phase modulation $\delta T_e/\delta\varphi_0$ depends sinusoidally on the phase φ_0.

2.5.3 Power and waveguide length dependence

To further confirm the observed optical torque is due to the interplay of the two orthogonal optical modes, we vary the ratio between $P_{\mathrm{TE}} = a_{\mathrm{TE}}^2$ and $P_{\mathrm{TM}} = a_{\mathrm{TM}}^2$ while keep the total power $P = P_{\mathrm{TE}} + P_{\mathrm{TM}} = 95\,\mu\mathrm{W}$. The measured T_m for two devices with different waveguide lengths ($l = 9$ and $10.5\,\mu\mathrm{m}$) exhibits similar semicircular dependence on P_{TE}/P as shown in Fig. 2.12(a), which agrees with Eq. 2.51. This result agrees with our expectation that either TE or TM mode alone ($P_{\mathrm{TE}}/P = 1$ or 0) should not generate optical torque, as the light polarization is invariant along the propagation and thus no angular momentum transfer between light and waveguide.

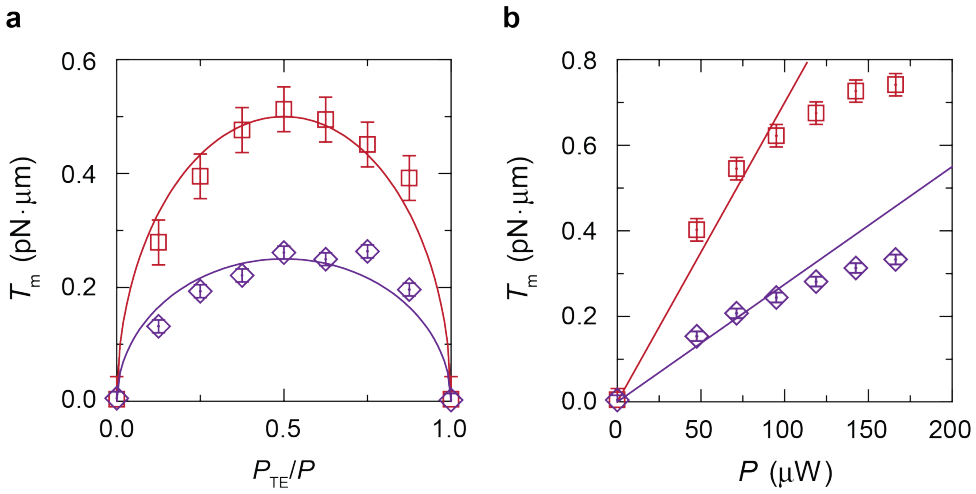

Figure 2.12: Dependence of optical torque on optical power. (a) The maximal torque T_m shows a semicircular dependence on the ratio P_{TE}/P with total optical power fixed for two devices with $l = 10.5\,\mu\mathrm{m}$ (purple) and $9\,\mu\mathrm{m}$ (red). (b) For the same two devices, the maximal torque T_m linearly depends on optical power when P is below $100\,\mu\mathrm{W}$ and it deviates from linear dependence for higher power.

With the same two devices, we also measure the dependence of T_m on the total optical power P with $P_{\mathrm{TE}} = P_{\mathrm{TM}}$. Surprisingly, the optical torque T_m

deviates from linear dependence on optical power when P is above $100\,\mu W$, as shown in Fig. 2.12(b). This nonlinear power dependence cannot be explained by our theory, as all effects considered in the preceding analysis are linear in optical power. Control experiments have been performed to rule out the typical Duffing mechanical nonlinearity in the measurement. Further investigation is required to resolve the origin of the nonlinear behavior observed here. However, the observed nonlinear behavior does not affect the results obtained in the linear regime.

Finally we measure the dependence of T_m on the suspended waveguide length with fixed total optical power and power ratio ($P_{\mathrm{TE}} = P_{\mathrm{TM}}$). The result plotted in Fig. 2.13 is fitted using Eq. 2.51 with η and Δn as free parameters, showing a good agreement with the theory. The value of Δn obtained from the fitting is 0.18, which is very close to the designed value of 0.16. The η obtained is 2.2 ± 1.0, implies the effective spin angular momentum carried by each photon in the waveguide is $(2.2 \pm 1.0)\hbar$. Therefore, the calculated value of $1.5\hbar$ is within the measurement uncertainty of the experiment.

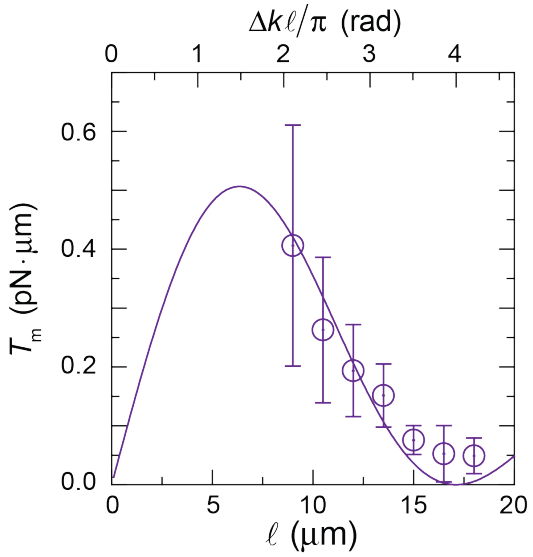

Figure 2.13: Dependence of optical torque on suspended waveguide length. The solid line is the fitting using Eq. 2.51.

2.6 Conclusion

Our experiments present the first unambiguous measurement of optical spin angular momentum and optical torque in integrated photonic devices. We have shown, both in theory and experiment, that the induced optical torque in waveguide is a direct consequence of change in light polarization state due to the geometric birefringence of the waveguide, which can be rationally engineered to enhance the effect. These designs can be achieved in other nanophotonic structures such as plasmonic devices, metasurfaces, and metamaterials to generate even more profound effects [33]. Furthermore, because the photon angular momentum only depends on light polarization and is independent of waveguide, the optical torque effects is universal over a broad spectral band, providing great leeway for engineering. In addition to spin angular momentum, photons can also have orbital angular momentum [34], and optomechanical effects arising from the spin-orbit interactions of light in nanophotonic systems [35] will be even more intriguing. Exploiting optical torque and optomechanical interaction with photon angular momentum can lead to efficient all-optical excitation and transduction of torsional nanomechanical devices with applications such as optomechanical gyroscopes [36] and torsional magnetometry [37, 38].

Chapter 3

Spin-Momentum Locked Interaction between Guided Photons and Surface Electrons in Topological Insulators

The propagation of electrons and photons can respectively have the spin-momentum locking effect which correlates the spin with the linear momentum. For the surface electrons in three-dimensional topological insulators (TIs), their spin is locked to the transport direction. For photons in optical fibers and photonic waveguides, they carry transverse spin angular momentum which is also locked to the propagation direction. A direct connection between the electron and photon spins occurs in TIs with lifted spin degeneracy, which leads to spin-dependent selection rules of optical transitions and results in phenomena such as circular photogalvanic effect (CPGE). In this chapter, we study the optical manipulation of surface electronic states in TIs at room temperature using circularly polarized light through the

circular photogalvanic effect. We also demonstrate an optoelectronic device that integrates a TI with a photonic waveguide. Interaction between the photons in the waveguide mode, which carries transverse spin angular momentum, and the surface electrons in a Bi_2Se_3 layer generate a directional, spin-polarized photocurrent. Because of optical spin-momentum locking, the device works in a novel way such that changing the light propagation direction reverses the photon spin and thus the direction of the photocurrent in TI. This novel device provides a directional interface that directly converts the information of light propagation path to the direction and spin polarization of the photoexcited surface current in TI.

3.1 Introduction to topological insulators

3.1.1 Topological classification of materials

The idea of using topological index to classify materials can be traced back to the integer quantum Hall effect (IQHE) in 1980s [39], where a two-dimensional free electron gas is subject to a strong perpendicular magnetic field at low temperature. In an IQH phase, the Hall conductance is quantized to an integer value that is characterized by a topological index [40], the Chern number, defined as the integral of the Berry curvature [41] over the two dimensional Brillouin zone. The measurement uncertainty of the quantized Hall conductance is remarkably small (on the order of 10^{-9}) even for macroscopic-size samples with disorders [42], which is very unusual for typical condensed matter experiments where things like impurities play important role. The physical reason underlies the accurate measurement is the chiral edge states developed at the sample edges that are immune to any back-scatterings or localization by impurities in the sample. Later on, Haldane proposed a theoretical model, showing that the IQH phase could also be

implemented in a honeycomb lattice with zero net magnetic flux passing through each unit cell and yet produce similar chiral edge states, known as the Haldane model [43]. However, the fundamental physics in the Haldane model is the same as the IQH phase: there are nonzero Chern numbers associated with the isolated electronic bands due to the breaking of time reversal symmetry.

It is until recent years people had realized that, similar to the Chern number introduced in the IQHE, in the presence of certain symmetries, other types of topological invariants can be defined to classify different gapped material systems. In this sense, insulators with nontrivial (nonzero) topological invariants refer to symmetry-protected topological insulators. For example, the most widely explored two-dimensional topological insulators are the time-reversal-symmetry protected topological insulators (or Z_2 topological insulators) that are classified with the so called Z_2 topological invariant [44]. Here, the Z_2 topological invariant can be either even or odd (0 or 1). Unlike the IQH phase, the Z_2 topological phase relies on time reversal symmetry and will be destroyed if the T symmetry is broken.

One of the most extraordinary consequences of having distinct gapped topological phases is the emergence of metallic/gapless boundary states at the interface of different topological phases (edge states for 2D systems and surface states for 3D systems), which is known as bulk-boundary correspondence [45]. This can be understood as the bulk topological index is a quantized number and cannot be changed by adiabatically deforming the bulk Hamiltonian. The change of the topological index across the materials interface can only be achieved through phase transition by closing and reopening the bandgap. Therefore, the existence of gapless boundary states is ensured by the topology of the bulk band structures and is independent of the detailed interface conditions.

3.1.2 Topological insulators in two and three dimensions

In the following we will briefly introduce the time reversal invariant topological insulators (topological insulators in short) in 2D and 3D and their realizations in real material systems.

2D topological insulators: quantum spin Hall effect

The tight-binding model proposed by Haldane considers a single spinless electron in the presence of a staggered external magnetic field. Therefore, the time reversal symmetry is broken. In 2005, Kane and Mele showed that a similar (but distinct) phase can be constructed in a graphene lattice by including the spin degrees of freedom of electrons, where the external magnetic field is replaced by spin-orbit coupling [46]. Since the spin-orbit coupling term is T invariant, the time reversal symmetry is preserved. Furthermore, the spin orbit coupling can serve as a spin-dependent effective magnetic field when an electron is hopping between next nearest lattice sites, meaning that spin-up and spin-down electrons experience an opposite effective magnetic field. Therefore, the Kane-Mele model is equivalent to two copies of Haldane's model with opposite magnetic fields for spin-up and spin-down electrons, respectively. The similarity of these two models implies that there must be a pair of edge states propagating at the boundary: electrons with opposite spins propagate in the reverse directions, which are known as the helical edge states. It can be shown that the helical edge states are topologically protected and are immune to back scattering by finite size impurities at the boundary as along as the time reversal symmetry is preserved [46]. One can also show that under an applied electric field, the total Hall conductance is zero as the contributions from electrons with opposite spins cancel each other. However, there will develop a pure spin current flowing perpendicular to the electric field and the spin current conductance is quantized. Therefore, it is named quantum

spin Hall effect [46].

Notably, for quantum spin Hall phase, the Z_2 topological invariant can be interpreted as the number of pairs of helical edge states intersecting with the Fermi energy is even or odd. For example, consider a 1D interface formed between two distinct insulators, the Kramers theorem requires all edge states at time-reversal-invariant k points ($k = 0$ or π) must be doubly degenerate. The double degeneracy will be lifted up due to spin-orbit coupling when moving away from the time-invariant k points. Therefore, two possible phases can be identified based on how the two degenerate points connected to each other in momentum space, as shown in Fig. 3.1. In the former configuration, the two double degenerate points at $k = 0$ and π are connected pairwise, which generally results in an energy gap. In contrast, gapless edge states are developed in the latter case due to the distinct paring. Compared to the IQH phase, where the edge states are unidirectional, there are equal number of edge states propagating in opposite directions that are time reversal pairs of each other in QSHI.

The original proposal of quantum spin Hall effect in graphene is far from experimental realization because the spin orbit coupling in carbon atoms is too weak [46]. In 2006, Bernevig et. al. showed that the quantum spin Hall effect can be experimentally realized in HgTe semiconductor quantum wells [47]. In particular, when the HgTe quantum well thickness is above the threshold value, the electronic bands of the HgTe go through a band inversion, which turns the electronic state into quantum spin Hall phase. One year after the theoretical prediction, König et al have experimental confirmed the gapless helical edge states in HgTe quantum wells in the transport measurements [48].

3D topological insulators

The idea of topological insulators can be generalized to 3D, which supports

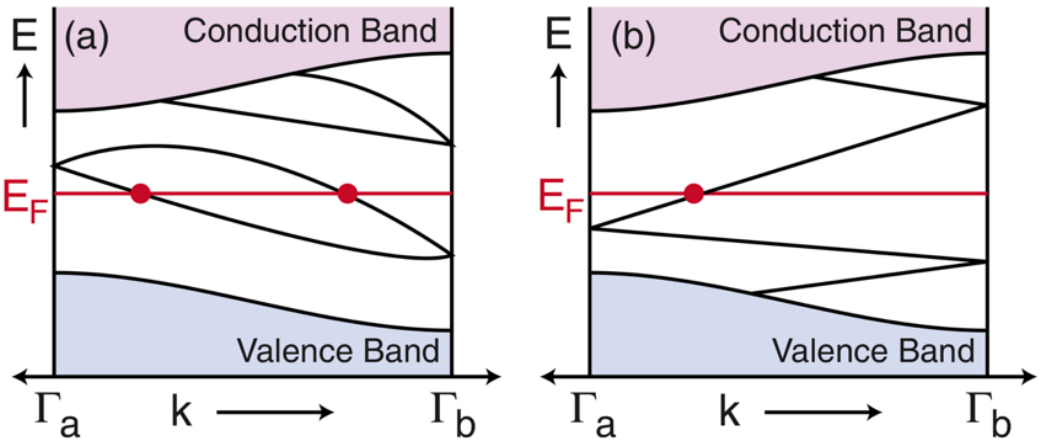

Figure 3.1: Energy dispersion between two Kramers degenerate points at $k = 0$ and π. (a) The Fermi energy intersects even number of edge states in a trivial insulator, whereas in (b) it is odd in a topologically nontrivial insulator. Reproduced with permission from [45].

gapless surface states at the 2D interface between two insulators of distinct phases. The topological invariants in 3D TIs are four Z_2 indices $(\nu_0; \nu_1, \nu_2, \nu_3)$ [49], which describe how the four time-invariant k points of the 2D Brillouin zone (Dirac points) are connected. Detailed discussion on the TI theory can be found in the reference [49–51].

Soon after the theoretical prediction of 3D TIs, its realizations in real materials have been demonstrated experimentally in various materials systems [52, 53], among which Bi_2Se_3 is one of the most promising materials due to the large band gap of 0.3 eV. In particular, the surface states hosted at the Bi_2Se_3/vacuum interface form a helical Dirac dispersion near the Γ point within the band gap, where the electron spin is locked perpendicular to its momentum. These exotic transport properties of surface electrons make them an intriguing platform to explore topological physics and hold promises for practical applications in the fields of spintronics and topological quantum computing.

3.2 Circular photogalvanic effect in Bi_2Se_3

3.2.1 Introduction to circular photogalvanic effect

Spin polarized current can be generated in materials with spin-orbit coupling under the homogenous irradiation of circularly polarized light without a bias voltage [3, 54–56]. The direction and magnitude of the generated current is proportional to the degree of circular polarization of light, meaning that the current flips direction under the reversal of light helicity and vanishes under the illumination of linear polarization. This is named circular photogalvanic effect, which has been extensively studied in bulk semiconductor materials and quantum well systems with spin-orbit coupling [3]. The microscopic mechanism that underlying the circular photogalvanic effect can be understood as following: circularly polarized light excites the interband transitions of electrons from valence band to the above conduction band. Because of the finite spin angular momentum of circularly polarized photons and the lifted spin degeneracy in electron bands, the transition probability depends on both the electron spin orientations and the helicity of the incident photons due to the selection rule imposed by angular momentum conservation. As a result, circularly polarized light generates an asymmetric excitation of electrons in momentum space, which leads to a finite spin polarized current in real space.

In addition to circular photogalvanic effect, other effects such as linear photogalvanic effect (LPGE) and photon drag effect [3, 57, 58] can also generate a photocurrent in an unbiased sample. However, in most cases the corresponding photocurrent is not spin polarized and is independent of light helicity, making them distinguishable from the circular photogalvanic effect in experiments.

3.2.2 Symmetry analysis

The form of the photocurrent as a function of light polarization can be obtained through symmetry analysis, which relies only on the information of crystalline symmetry. In the following, we give a brief discussion on the photogalvanic effect from a symmetry argument. More detailed derivations are given in [3, 59, 60]. Assuming the leading term of the dc photoresponse is of the second order in the complex electric field amplitudes and can, in general, be written as

$$j_i = \sigma_{ijk} E_j^* E_k + T_{ijkl} q_l E_j^* E_k \tag{3.1}$$

where σ_{ijk} and T_{ijkl} are, respectively, the third and fourth rank complex tensors, E is the complex electric field and q is the optical wave vector. Microscopically, the second term takes into account the transfer of linear momentum of photons to electrons in the light-matter interaction, known as the photon drag effect [3], as it involves the optical linear momentum q. For simplicity, we will drop the second term and focus on the first term that is independent of q in the following analysis. The first important implication of Eq. 3.1 is the photocurrent should vanish in a materials with spatial inversion symmetry: under spatial inversion operation, j_i changes sign while $E_j^* E_k$ does not. Therefore, for material such as Bi_2Se_3 with bulk inversion symmetry, the measured photocurrent should only be generated at the sample surface, where the inversion symmetry is broken. Moreover, by separating the real and imaginary part of σ_{ijk}, we have

$$j_i = \mathrm{Re}(\sigma_{ikj}) E_j^* E_k + i\mathrm{Im}(\sigma_{ikj}) E_j^* E_k \tag{3.2}$$

By noting that j_i is real and comparing Eq. 3.2 with its complex conjugate, we can conclude that $\mathrm{Re}(\sigma_{ijk})$ is symmetric in its last two indices whereas $\mathrm{Im}(\sigma_{ijk})$

is antisymmetric. Therefore, the photocurrent can be rewritten as:

$$j_i = \frac{1}{2}j_i + \frac{1}{2}j_i^* = \frac{1}{2}\mathrm{Re}(\sigma_{ijk})(E_j^* E_k + E_j E_k^*) + \frac{i}{2}\mathrm{Im}(\sigma_{ijk})(E_j^* E_k - E_j E_k^*) \quad (3.3)$$

Note that the photocurrent contributed from $\mathrm{Im}(\sigma_{ijk})$ can be further simplified using a second rank tensor γ_{ip} as

$$\mathbf{j}_{\mathrm{CPGE}} = \frac{i}{2}\mathrm{Im}(\sigma_{ijk})(E_j^* E_k - E_j E_k^*) = i\gamma_{ip}(\mathbf{E}^* \times \mathbf{E})_p \quad (3.4)$$

where $\gamma_{ip} = \frac{1}{2}\mathrm{Im}(\sigma_{ijk})$. The dependence of $\mathbf{j}_{\mathrm{CPGE}}$ on $\mathbf{E}^* \times \mathbf{E}$ implies that it is helicity-dependent photoexcitation: photocurrent changes sign for left- and right-handed circularly polarized light and vanishes for linear polarization. The lattice symmetry of Bi_2Se_3 at surface ($C_{3\nu}$) further reduces the number of nonvanishing tensor elements of γ_{ip} from 9 to 2, namely $\gamma_{xy} = -\gamma_{yx} = \gamma$ [59] (here material interface is in x-y plane). Therefore, the CPGE current can be simplified as

$$\mathbf{j}_{\mathrm{CPGE}} = i\gamma[(E_z^* E_x - E_x^* E_z)\hat{\mathbf{x}} - (E_y^* E_z - E_z^* E_y)\hat{\mathbf{y}}] \quad (3.5)$$

Eq. 3.5 implies that oblique light incidence (or a finite E_z field) is essential for the generation of the CPGE current and the induced $\mathbf{j}_{\mathrm{CPGE}}$ must flow in the transverse direction perpendicular to the light incidence plane. To see this, we consider a plane wave $\mathbf{E}$ with arbitrary polarization incident in x-z plane and the complex electric fields can be written as

$$\mathbf{E} = \begin{bmatrix} E_p \cos(\theta) e^{i\phi} \\ E_s \\ E_p \sin(\theta) e^{i\phi} \end{bmatrix} e^{-i\omega t} \quad (3.6)$$

where E_s, E_p, ϕ are the s and p wave amplitudes and their relative phase, taken together determine light polarization. Substituting Eq. 3.6 back into Eq. 3.5 yields

$$\mathbf{j}_{\mathrm{CPGE}} = 2\gamma E_s E_p \sin\theta \sin\phi \hat{\mathbf{y}} \quad (3.7)$$

This surface current is flowing in the transverse direction (along y axis) and vanishes for normal light incidence ($\theta = 0$).

Similar analysis can be applied to the real part of σ_{ijk} and reveals that the corresponding photocurrent $\mathbf{j}_{\mathrm{LPGE}}$ is independent of light helicity and can have both transverse and longitudinal components [59]. Therefore, in a real experiment, the contributions from $\mathbf{j}_{\mathrm{CPGE}}$ and $\mathbf{j}_{\mathrm{LPGE}}$ can be distinguished by measuring their dependence on light polarization and the current direction with respect to light incident plane. Moreover, the dependence of the photocurrent on the crystalline orientation may also help to distinguish the contributions from different mechanisms, as they are related to the photocurrent through tensors of various rank, which embed the information of crystalline symmetry.

3.2.3 Microscopic model of CPGE in Bi_2Se_3

The microscopic mechanism that is responsible for the circular photogalvanic effect in Bi_2Se_3 can be understood by considering the spin-dependent interband transitions induced by circularly polarized light. To be concrete, we consider the illumination of near infrared light ($\hbar\omega \approx 0.8\,\mathrm{eV}$) on a heavily n-doped Bi_2Se_3 sample, as shown in Fig. 3.2, where the Fermi level is at the bottom of the bulk conduction band. Based on the Fermi's golden rule and Boltzmann equation, the dc photocurrent resulted from the interband transitions from the occupied surface bands to the bulk conduction bands can be expressed as [60]

$$\begin{aligned}\mathbf{J} = -\frac{2\pi e}{\hbar}\sum_{\mathbf{k},\langle\eta,\xi\rangle}\left(\tau_{pb}\mathbf{v}_{b,\mathbf{k},\eta} - \tau_{ps}\mathbf{v}_{s,\mathbf{k},\xi}\right)\left|\langle\phi_{b,\mathbf{k},\eta}|H_{int}|\phi_{s,\mathbf{k},\xi}\rangle\right|^2 \\ \times\left(f^0_{s,\mathbf{k},\xi} - f^0_{b,\mathbf{k},\eta}\right)\delta(E_{b,\mathbf{k},\eta} - E_{s,\mathbf{k},\xi} - \hbar\omega)\end{aligned} \tag{3.8}$$

where τ_{pb} and τ_{ps} are the momentum relaxation time of bulk and surface bands, $\mathbf{v}$ is electron velocity, f_0 is the equilibrium Fermi distribution function, η denotes

the two-fold spin degeneracy of the bulk bands and ξ refers to upper and lower Dirac cone. The interaction Hamiltonian $H_{int} = -\frac{e}{m}\mathbf{A} \cdot \mathbf{P}$ accounts for the minimal coupling between light and electrons. The full evaluation of Eq. 3.8 can be rather complicated, however, the analysis of the transition matrix element $|\langle \phi_{b,\mathbf{k},\eta}|H_{int}|\phi_{s,\mathbf{k},\xi}\rangle|^2$ can give instructive information [60]. For example, by noting that the electron velocity $\mathbf{v}$ is odd in $\mathbf{k}$, the induced photocurrent after the summation over $\mathbf{k}$ space is nonzero only if the transition matrix element is asymmetric in $\mathbf{k}$. This requires the optically induced interband transitions to be asymmetric in momentum space, which can be satisfies through the optical selection rules that are dependent of the electron spin. In this case, the right (left) moving surface band, marked in red (purple) in Fig. 3.2, is preferably excited under left (right) circularly polarized light illumination, giving rise to a directional net current flow in real space. Moreover, direction of the resulted current should be perpendicular to the light incidence direction, as the surface electron spin is locked perpendicularly to its crystal momentum $\mathbf{k}$ due to spin-momentum locking effect.

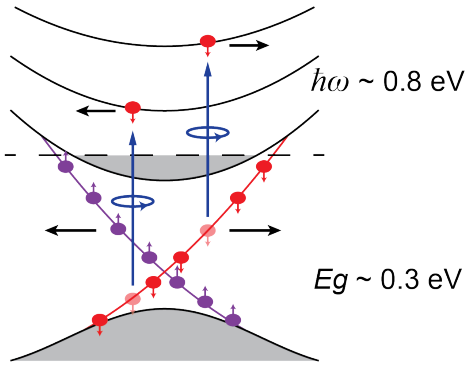

Figure 3.2: Schematic illustration of the selection rules in TI. The selection rules of optical transitions in TI with lifted spin degeneracy lead to spin-dependent photoexcitation. Circularly polarized light will selectively excite electrons with one-type of spin from the surface bands to the bulk bands, generating a spin-polarized photocurrent flowing in a direction determined by the optical polarization.

3.2.4 Device layout and measurement setup

Device fabrication

To experimentally investigate the photogalvanic effects in TIs, we use films of topological insulator Bi_2Se_3 exfoliated from a bulk crystal (obtained from HQ Graphene, Netherland) and transferred on a silicon substrate with 450 nm thick SiO_2 layer. To explore how the photoresponse depends on sample crystalline direction, the flakes were first patterned into circular shape using electron beam lithography and low power argon ion milling, followed by the deposition of eighteen electrodes positioned in a rotation around the Bi_2Se_3 disk (as shown in Fig. 3.3). A Ti(10 nm)/Al(400 nm)/Au(80 nm) metal multilayer was deposited as the electrodes using electron beam evaporator after an interface cleaning step using argon ion milling for 10 seconds.

Measurement scheme

We measure the photogalvanic effects in the sample using a free-space optics configuration similar to the previous studies [58,60–62] but with the difference that near infrared continuous wave laser ($\lambda = 1.55\,\mu m$) is used instead of visible light. The photoresponse is measured by modulating the laser source with a high-speed electro-optic modulator (Lucent 2623 NA) driven by a lock-in amplifier (Stanford Research Systems, SR865A). An additional erbium-doped fiber amplifier (EDFA) is used after the modulator to amplify the optical power and the laser intensity was modulated at 10 kHz. The polarization of the incident light is varied from linear to circular by rotating a quarter waveplate with angle α, while the incident angle is fixed at 45° (in x-z plane) to the sample surface. The measurement configuration is shown in Fig. 3.3. The photocurrent is collected from the pair of electrodes positioned along the y-axis when the sample was rotated in directions specified with the azimuthal angle φ. To minimize the thermoelectric effect due

to non-uniform heating of the sample, we focus the laser beam to a spot of 330 µm in diameter, much larger than the size of the Bi_2Se_3 sample which has a diameter of 10 µm, and position the sample at the beam center. The laser power level is fixed at 45 mW, at which the photoresponse of the device is in the linear regime. All of the following measurements are performed at room temperature in the atmosphere.

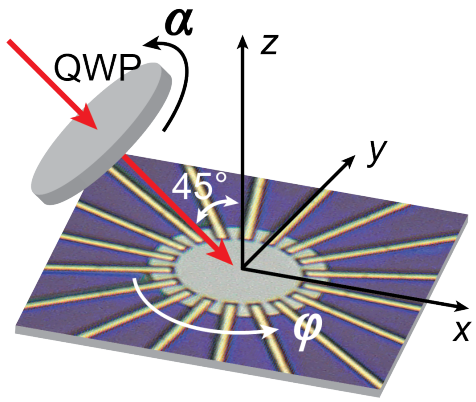

Figure 3.3: Device image and measurement scheme. The polarization of the incident light is changed by rotating a quarter waveplate with angle α. The Bi_2Se_3 is patterned to a circular disk. Nine pairs of electrodes are used to measure the transverse photocurrent generate along y directions when the sample is rotated with angle φ.

3.2.5 Anisotropy of photogalvanic effects in Bi_2Se_3

We investigate the anisotropy of the photogalvanic effects in Bi_2Se_3 by measuring its polarization-dependent photoresponse at various azimuthal angle φ. The results of polarization dependent photocurrent with $\varphi = 0°, 20°, 40°, 60°$ are plotted in Fig. 3.4, which show similar variation with polarization as reported in the

previous works [58,60,62]. The polarization dependence also exhibits clear difference when the photocurrent is collected with different sample rotation angle φ, manifesting the anisotropy. We fit the results with the model that includes four components of distinctive polarization dependence:

$$j_y(\varphi,\alpha) = C(\varphi)\sin(2\alpha) + L_1(\varphi)\sin(4\alpha) + L_2(\varphi)\cos(4\alpha) + D(\varphi) \tag{3.9}$$

The coefficient C corresponds to the circular photogalvanic effect, coefficient L_1 and L_2 correspond to linear photogalvanic effect but possibly with different origins, and D is the polarization independent photocurrent that may include a thermoelectric contribution.

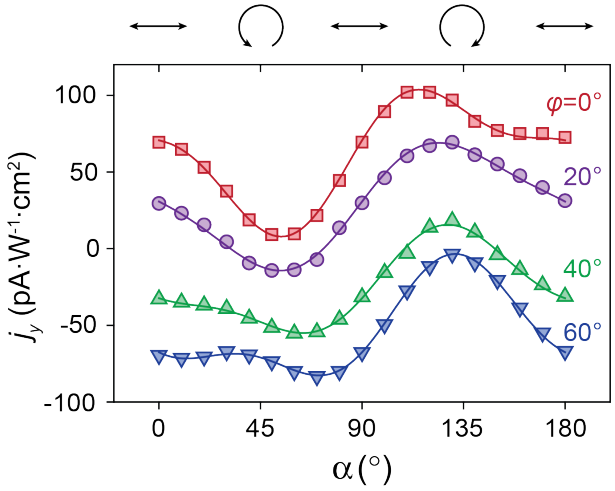

Figure 3.4: Polarization-dependent photocurrent collected with electrode pair positioned along the y-axis when the sample is rotated to representative values of φ.

We fit the measurement results obtained at each φ and extract the parameters (C, L_1, L_2, D). The angular dependence results are plotted in Fig. 3.5. The results for L_2 and D clearly exhibit a three-fold rotation symmetry with a period of 120°, in agreement with the space group of the Bi_2Se_3 crystal. This agreement

corroborates with the conclusion of previous temperature-dependent studies [58] that L_2 and D stem from a similar origin of the bulk crystal. In clear contrast, the results of C and L_1 show indiscernible angular dependence. Because the helical Dirac cone for the surface states appears at the Γ point in k-space, in the low energy limit, rotational symmetry is expected for interband transitions that involve the surface states. Therefore, C and L_1 are likely to share a common origin of interband transitions from the occupied surface states to the bulk bands above, given that the exfoliated Bi_2Se_3 sample is n-doped and the photon energy of 0.8 eV is much larger than the bulk bandgap of 0.3 eV. In addition, photon drag effect may also cause helicity-dependent photocurrent, however, recent measurement by varying the incident angle has ruled it out [60]. Our angular-dependent photocurrent measurement is useful to clarify the origins of different contributions and show that the overall photogalvanic current varies with the crystalline orientation due to the anisotropic contribution from the bulk.

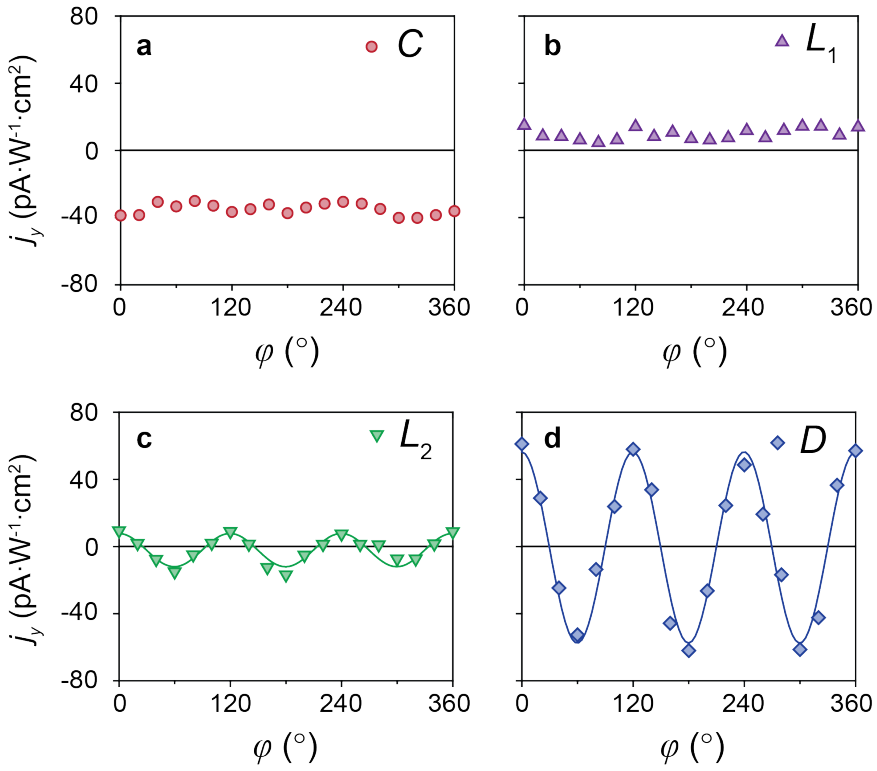

Figure 3.5: Anisotropy of the photogalvanic effect in Bi_2Se_3. (a)-(d) Parameters (C, L_1, L_2, D) extracted from the measurement in Fig. 3.4 as a function of φ. L_2 and D show clear anisotropy with threefold rotational symmetry, in agreement with the crystal structure of Bi_2Se_3, whereas C and L_1 show no obvious angular dependence.

3.2.6 Further experiments

Dependence of photoresponse on optical power

We make sure the measured photoresponse on all devices are in the linear regime by measuring the photocurrent as a function of optical power. For example, Fig. 3.6 shows the result measured on the same device presented in Fig. 3.3 under various optical power excitation ($\alpha = 0°, \varphi = 0°$), which shows a clear linear dependence on laser intensity.

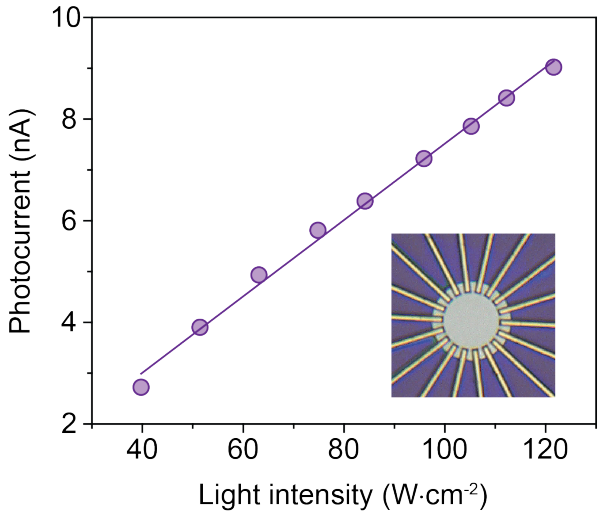

Figure 3.6: Linear dependence of photocurrent on laser intensity. The purple line is the linear fitting to the experimental data. The inset shows the device optical image.

Frequency responses of different photocurrent contributions

Different mechanisms (thermoelectric effect and photogalvanic effect) that contribute to the photocurrent have distinct frequency responses, which are measured in the free-space optics configuration. Figure 3.7(a) shows the optical image of a device with a pair of metal contacts in the transverse direction (y axis). To

isolate the CPGE contribution from the total photocurrent, we position the sample at the beam center ($y = 0$) and measure the frequency-dependent photoresponse under the excitation of either left- or right-handed circularly polarized light ($\alpha = 45°, 135°$). According to Eq. (3.9), the thermoelectric current (due to misalignment) and LPGE current are helicity-independent, whereas CPGE current changes sign for opposite light helicity. Therefore, by subtracting the photocurrent of the two measurements, only the CPGE contribution remains, showing a characteristic frequency of $f_{3\mathrm{dB}} = 4\,\mathrm{MHz}$ (red line in Fig. 3.7(b)). On the other hand, the thermoelectric photoresponse can also be isolated by subtracting the photocurrents measured at positions shifted from the beam center ($y = \pm 25\,\mu\mathrm{m}$) under linearly-polarized light excitation ($\alpha = 0°$). The thermoelectric contribution in the two measurements changes polarities due to the reversal of temperature gradients, whereas the photogalvanic current remains unchanged. The difference of the two measurements gives the thermoelectric current and exhibits a characteristic frequency of $f_{3\mathrm{dB}} = 30\,\mathrm{kHz}$ (blue line in Fig. 3.7)(b), much slower than that of the photogalvanic current.

3.3 Spin-momentum locked interactions between photons and electrons

3.3.1 Spin-momentum locking for guided photons

In contrast to plane wave in homogenous media, the electric field of non-paraxial optical beams or spatially bound optical modes in fibers or waveguides are no longer purely transverse but also have longitudinal field components due to the lateral confinement. In particular, the emerging longitudinal field has a $\pm\pi/2$

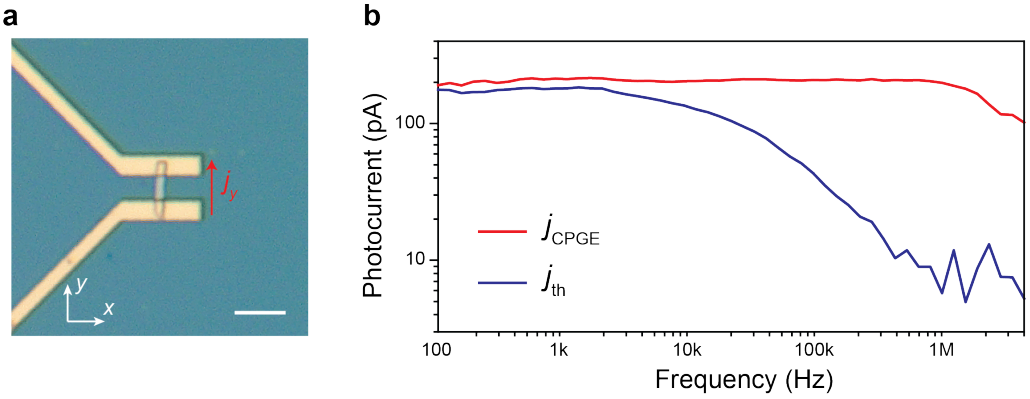

Figure 3.7: Frequency responses of the thermoelectric and photogalvanic current. (a) Optical microscopic image of a device used to determine the frequency responses. The scale bar is 5 µm. (b) The extracted CPGE and thermoelectric current show a cut-off frequencies of 4 MHz and 30 kHz, respectively.

phase shift relative to the transverse field component, with the sign being locked to the wave vector or light propagation direction [5,63–65]. The physical principle underlying the nonvanishing longitudinal field is the Gauss's law $\nabla \cdot \mathbf{E} = 0$ (where we assume a lossless dielectric medium). To show this, consider a waveguide mode propagating along $z-$axis, the electric field is $\mathbf{E}(x, y)e^{\pm ikz - i\omega t}$, where k is the wave vector and ω is the optical frequency. Substituting the electric field back into the Gauss's equation yields:

$$\partial_x E_x + \partial_y E_y \pm ikE_z = 0 \tag{3.10}$$

Eq. 3.10 implies that the longitudinal field E_z is nonvanishing when the transverse field components are nonuniform in the transverse plane, as for the case of waveguide modes that are laterally confined. Furthermore, its magnitude is directly proportional to the lateral confinement strength (the lateral divergence of transverse fields), suggesting that the effect is most prominent in integrated photonic circuits, where the lateral confinement is down to subwavelength scale. Consequently, the

corresponding light carries transverse spin angular momentum (here we define the optical angular momentum of the electric field as $\mathbf{S} = -[i\varepsilon_0/(2\omega)]\mathbf{E}^* \times \mathbf{E}$ [63,66]), where ε_0 is vacuum permittivity. Eq. 3.10 also suggests the handedness of the polarization and the transverse SAM are locked to the propagation direction, meaning that their signs reverse with the flip of light propagation direction, as illustrated in Fig. 3.8 for a waveguide mode. This effect is conceptually analogous to the helical edge states in quantum spin Hall effect and the spin-momentum locking effect occurring for the surface electrons in 3D TIs, albeit the optical systems (waveguide, fibers) are topologically trivial (which means the waveguide modes do not have topological protection).

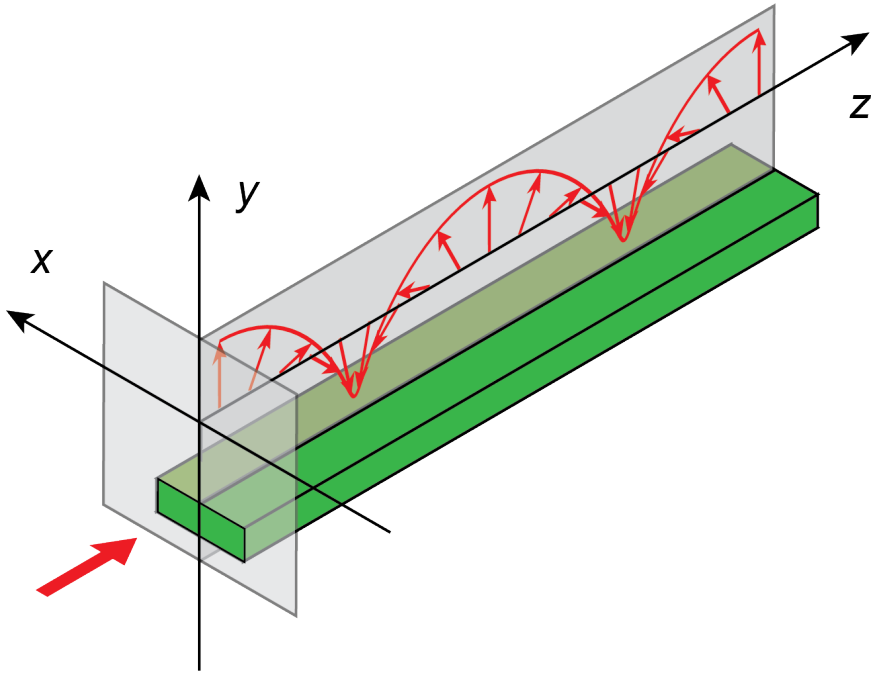

Figure 3.8: Spinning evanescent electric field of the TM mode in a silicon waveguide.

Consider the quasi-TE and TM modes of a waveguide made of silicon, as simulated in Fig. 3.9(a), which is 1500 nm wide and 220 nm high and cladded

on all sides with silicon dioxide. The mode has considerable longitudinal field component (E_z) with a $\pm\pi/2$ phase difference to the transverse field component, and thus are elliptically polarized in the propagation plane with transverse SAM. It is apparent that, on top of the waveguide, the transverse electric SAM density (S_x) of the TM mode is more significant, more than 100 times higher than that of the TE mode.

Now consider a layer of TI material placed on the top of the waveguide, as marked with the dashed line in Fig. 3.9(a). Because the photons in the TM mode are elliptically polarized, through CPGE effect there will induce a photocurrent flowing in the longitudinal direction (z axis) with spin polarized along the transverse direction (x axis). In this way, the CPGE interaction couples the spin-momentum locking of the TM mode photons with the surface electrons in the TI. Reversing the propagation direction of the light in the waveguide will reverse the handedness of the elliptical polarization, the CPGE photocurrent direction and the spin polarization. Therefore, such a TI-waveguide integration makes an optoelectronic device, the first of its kind, that converts the propagation path information (forward or backward) of photons to the spin polarization of electrons in a directional photocurrent. The spin-momentum locking of both photons and electrons should manifest themselves in the photocurrent direction. The schematic diagram in Fig. 3.9(b) illustrates the working principle of such a novel device.

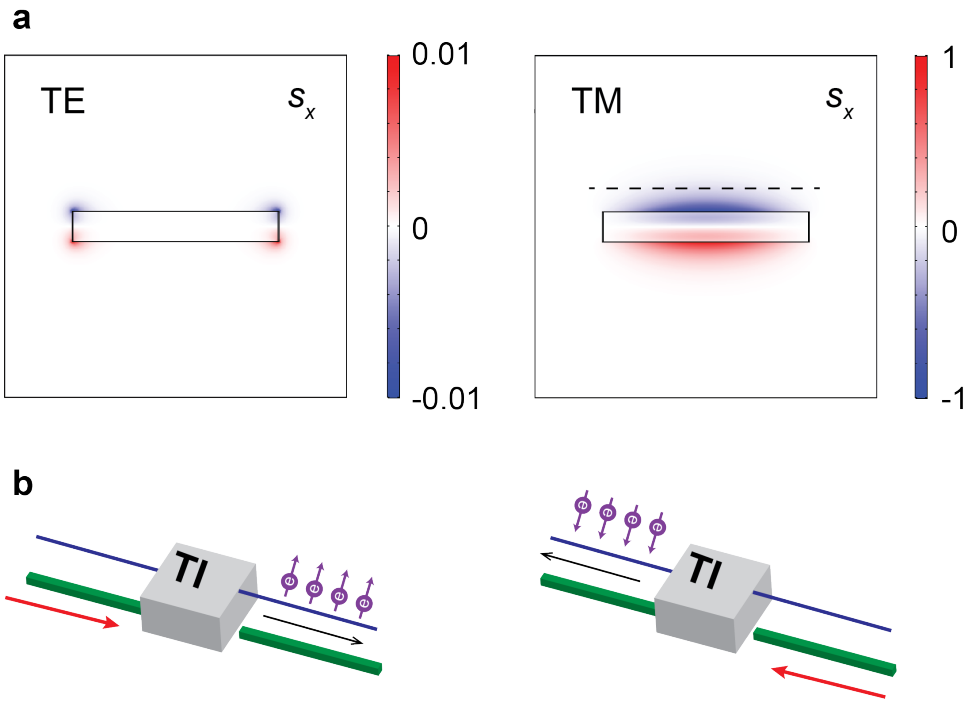

Figure 3.9: Spin-momentum locking for photons and electrons. (a) The x-component of SAM density (S_x) for the TE and TM mode of a silicon waveguide (1500 nm wide and 220 nm high). On the top of the waveguide, S_x of the TM mode is more than 100 times higher than that of the TE mode. Therefore, the TM mode has a more significant helicity-dependent effect in its evanescent field. (b) The proposed device integrates the TI on a waveguide to explore the spin-momentum locking of electrons and photons. It outputs a spin-polarized current with its spin polarization and direction determined by the light input direction.

3.3.2 Experiment results

Device fabrication and measurement layout

We integrate an exfoliated Bi_2Se_3 flake on a silicon waveguide to demonstrate the device. Figure 3.10(a) shows the optical microscope image of a representative device (Device C). The waveguide-integrated Bi_2Se_3 devices are fabricated on a silicon-on-insulator wafer with a 220 nm top silicon layer and a 3 µm buried oxide layer. The underlying photonics layer is patterned using standard electron beam lithography and reactive ion etching processes. Subsequently, a 150 nm layer of hydrogen silsesquioxane (HSQ) is spin-coated and exposed with electron beam lithography to planarize the photonics layer, on top of which a Bi_2Se_3 flake is then transferred. This cladding layer is intentionally designed to be thick to avoid significant disturbance of the waveguide mode by both the TI and the electrical contacts, but allows the evanescent field of the mode to interact with the TI. Two pairs of electrodes underneath the flake are used to collect the photocurrent generated at the bottom surface of the TI. One electrode pair is positioned (with a separation of $l = 3\,\mu m$ for Device C) along the longitudinal direction (z axis). We design the integrated photonic circuit to allow coupling of either TM or TE modes to the waveguide, and symmetrically from either the left or the right ends. Therefore, overall there are eight different measurement configurations for the TM or the TE modes propagating either leftward or rightward along the waveguide with either the longitudinal or the transverse current being collected.

When measuring the waveguide-integrated device, a fiber array is used to couple light into the device and collect the transmitted optical signal for alignment and calibration. Integrated grating couplers are fabricated to couple the TE and TM modes into the photonic device. A fiber polarization controller is used to control the optical polarization. The coupling efficiencies for TE and TM mode

coupler are $\sim$ 8% and $\sim$ 6%, respectively. During the measurement the laser power is fixed at 4 mW and hence the devices' photoresponse is in the linear regime.

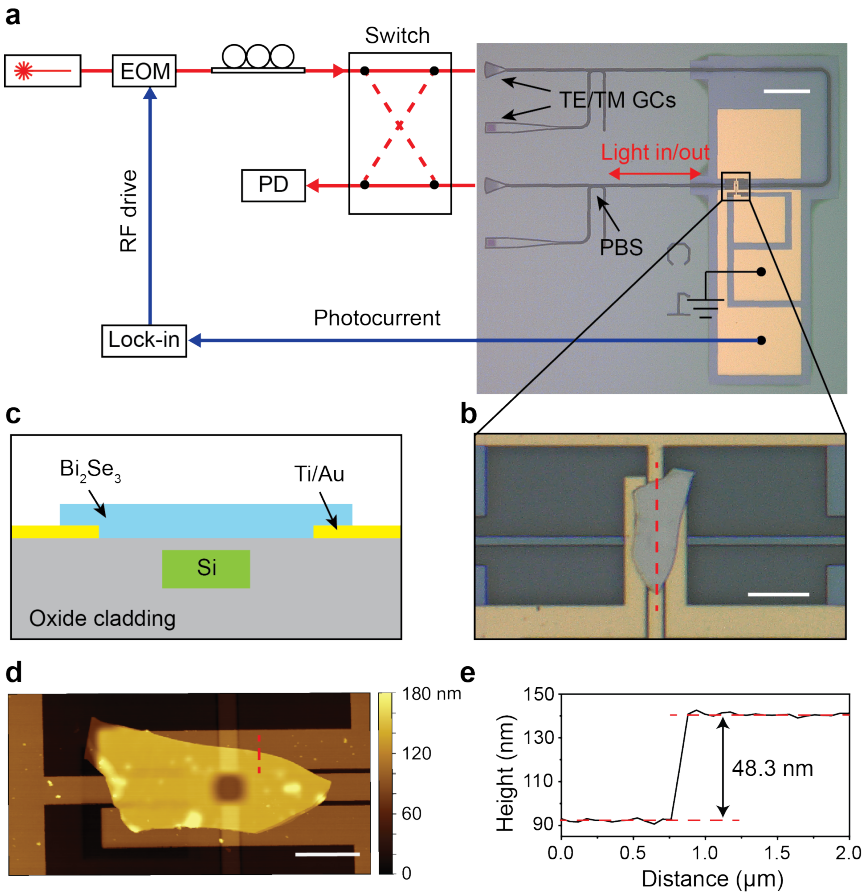

Figure 3.10: Waveguide-integrated device layout and measurement scheme. (a) The x-component of SAM density (S_x) for the TE and TM mode of a silicon waveguide (1500 nm wide and 220 nm high). On the top of the waveguide, S_x of the TM mode is more than 100 times higher than that of the TE mode. Therefore, the TM mode has a more significant helicity-dependent effect in its evanescent field. (b) The proposed device integrates the TI on a waveguide to explore the spin-momentum locking of electrons and photons. It outputs a spin-polarized current with its spin polarization and direction determined by the light input direction.

Results

Figure 3.11 illustrates the situations when the TM mode is launched into the waveguide. As shown in Fig. 3.9(a), the photons in the TM mode are elliptically polarized and carry transverse SAM (along x axis), and through the CPGE effect they will selectively excite surface electrons with their spin aligned with the optical SAM and induce a spin-polarized net current I_{CPGE} flowing in the longitudinal direction (z axis) due to the spin momentum locking effect of topological surface states. Here, the CPGE effect is due to the SAM of the waveguide TM mode in the transverse direction, rather than the longitudinal SAM as in the free-space laser beam. Importantly, when the propagation direction of the TM mode is reversed (equivalent to apply time reversal operation and change wave vector from k to $-k$), the polarity of $\mathbf{S}$ also reverses, namely the optical spin-momentum locking, and the resulting I_{CPGE} will flow in the opposite direction, as illustrated in Fig. 3.11. Such a longitudinal photocurrent with its direction dependent on the light propagation thus is the hallmark of the spin-momentum locked interaction between the guided optical mode and the topological surface states. Other than CPGE, other effects, including LPGE and thermoelectric effect can also generate photocurrent so the total longitudinal photocurrent should be expressed as: $I_{\mathrm{long}} = I_{\mathrm{CPGE}} + I_{\mathrm{LPGE}} + I_{\mathrm{th}}$. The current produced by LPGE can have both transverse (x) and longitudinal (z) components but should be independent of the light propagation direction (Fig. 3.11). The thermoelectric effect due to the temperature gradient along the waveguide may induce a longitudinal photocurrent (I_{th}) that also reverses sign with the light propagation. However, this thermal effect should work in the same way for both TM and TE modes, the latter, however, should produce negligible longitudinal I_{CPGE} because of its negligible S_x in its evanescent field. Therefore, through analyzing the results obtained with different measurement configurations

in our device, contributions from different mechanisms can be unambiguously distinguished from each other.

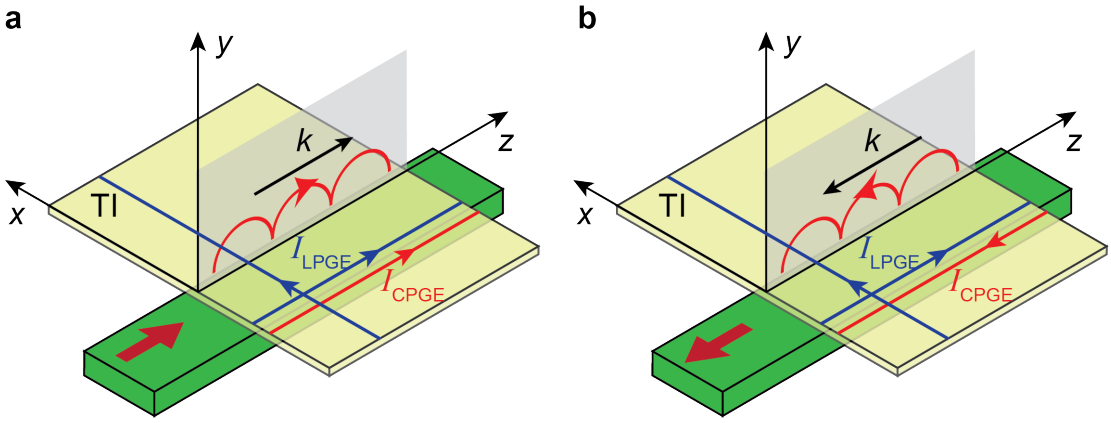

Figure 3.11: Directional photogalvanic current generated in TI. The photocurrent I_{CPGE} generated in the TI by the TM mode of the waveguide is only along the longitudinal direction. Because of the photonic spin-momentum locking, I_{CPGE} changes direction when the light propagation direction in the waveguide is reversed from forward (a) to backward (b). In contrast, the LPGE photocurrent has both longitudinal and transverse components which are independent on the light propagation direction.

Figure 3.12 show the photocurrent, measured with different experiment configurations, as a function of frequency when the laser is modulated with an electro-optic modulator and coupled into the waveguide through integrated grating couplers for TE and TM modes. The most notable results are shown in Fig. 3.12(a)-(b) when the TM mode is launched into the waveguide from either the left or right side. The longitudinal current $I_{\mathrm{long}}^{\mathrm{TM}}$ and its phase show a strong dependence on the light propagation direction. Specifically, when the light propagation direction is changed from leftward to rightward, the sign of $I_{\mathrm{long}}^{\mathrm{TM}}$ reverses, as can be seen from the 180° change in the phase response, along with a change in the magnitude. In contrast, in Fig. 3.12(c)-(d), when TE mode is launched in the waveguide, reversing the light propagation direction has a negligible effect on both the magnitude

and the phase of $I_{\text{long}}^{\text{TE}}$. $I_{\text{long}}^{\text{TE}}$ is expected to include contributions from both LPGE effect ($I_{\text{LPGE}}^{\text{TE}}$) and thermoelectric effect (I_{th}) but negligible contribution from the CPGE effect ($I_{\text{CPGE}}^{\text{TE}}$). Considering the thermoelectric effect, the temperature gradient is along the z-axis in the sample and the induced I_{th} should be reversed when the light propagation direction is reversed. However, $I_{\text{long}}^{\text{TE}}$ shows unnoticeable difference between the opposite light propagation directions. Therefore, we can conclude that the thermoelectric effect is insignificant in our device, possibly because of the small device size and efficient heat sinking. After ruling out the thermoelectric contribution, for the TM mode, we can express the longitudinal photocurrent as $I_{\text{long}}^{\text{TM}\pm} = \pm I_{\text{CPGE}}^{\text{TM}} + I_{\text{LPGE}}^{\text{TM}}$, where $I_{\text{CPGE}}^{\text{TM}}$ is the CPGE photocurrent which flows along the light propagation direction (marked with $\pm$), and $I_{\text{LPGE}}^{\text{TM}}$ is the LPGE photocurrent which is independent of the light propagation direction. Similarly, for the TE mode, $I_{\text{long}}^{\text{TE}\pm} = \pm I_{\text{CPGE}}^{\text{TE}} + I_{\text{LPGE}}^{\text{TE}}$. The transverse photocurrents along the x-axis generated by the TM ($I_{\text{trans}}^{\text{TM}}$) and the TE modes ($I_{\text{trans}}^{\text{TE}}$) provide good control results. Because both the TM and TE modes are linearly polarized in the x-y plane, there is zero z-component of SAM (S_z) and hence no CPGE photocurrent along the transverse x-direction. The symmetry of the device also minimizes the thermoelectric contribution. Therefore, we can conclude that $I_{\text{trans}}^{\text{TM}}$ and $I_{\text{trans}}^{\text{TE}}$ consist of only LPGE photocurrent, which does not change with the light propagation direction. This is clearly shown in Fig. 3.12(e)-(f). The difference between the magnitude of $I_{\text{trans}}^{\text{TM}}$ and $I_{\text{trans}}^{\text{TE}}$ is attributed to the different field intensities of the two modes at the TI layer. Above results and analysis show that, among all of the configurations, only the longitudinal photocurrent generated by the TM mode ($I_{\text{long}}^{\text{TM}}$) uniquely shows a strong dependence on the light propagation direction due to the spin-momentum locked interaction between the photon transverse spin and the TI's surface electrons.

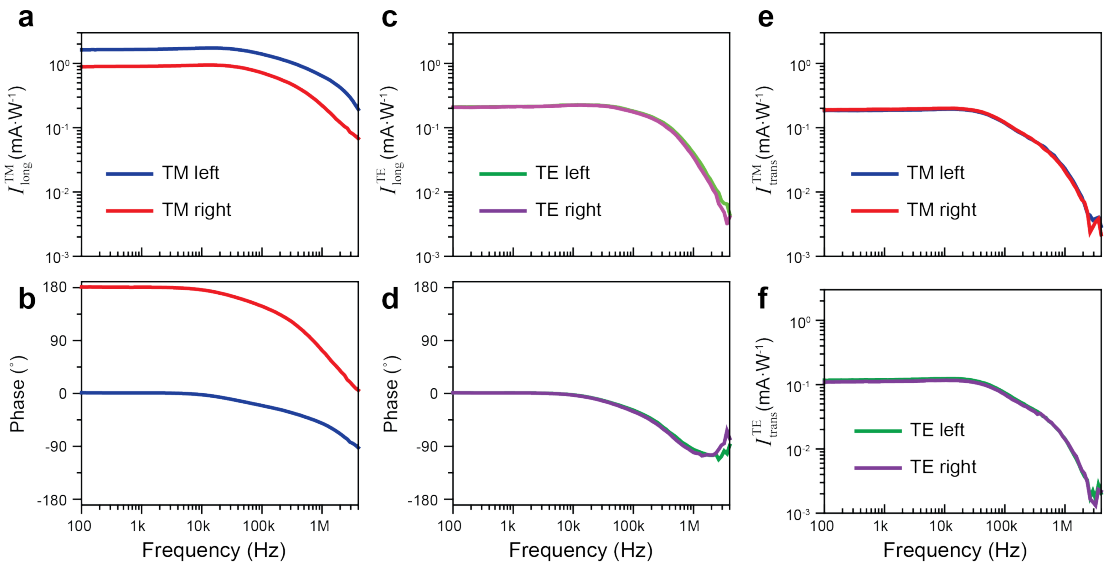

Figure 3.12: Frequency response of the photogalvanic current generated in TI. (a)-(b) Frequency response of the amplitude (a) and the phase (b) of the longitudinal photocurrent ($I_{\text{long}}^{\text{TM}}$) when TM mode is launched in the waveguide. When the light propagation is reversed from leftward to rightward, the sign of the photocurrent reverses, as seen from the 180° change in the phase response, and the amplitude of the photocurrent also changes. (c)-(d) The longitudinal photocurrent of the TE mode ($I_{\text{long}}^{\text{TE}}$) (amplitude in (c) and phase in (d)) and the transverse photocurrent of the TM mode (e) and the TE mode (f). all show negligible dependence on the light propagation direction.

We can further extract and quantify the contributions of the CPGE and LPGE effects in above results by using the reciprocal symmetry of the device such that: $I^{\mathrm{TM}}_{\mathrm{CPGE}} = (I^{\mathrm{TM+}}_{\mathrm{long}} - I^{\mathrm{TM-}}_{\mathrm{long}})/2$ and $I^{\mathrm{TM}}_{\mathrm{LPGE}} = (I^{\mathrm{TM+}}_{\mathrm{long}} + I^{\mathrm{TM-}}_{\mathrm{long}})/2$. The result obtained from Device C are summarized in Fig. 3.13(a) and show that, for the TM mode, the CPGE contribution is more than 3 times larger than the LPGE contribution. The dominance of the CPGE effect results in the reversal of the total photocurrent with the light propagation direction. For the TE mode, the photocurrent is dominated by the LPGE contribution, which is independent of the light propagation direction. The LPGE effect originates from the bulk of the TI and, as shown in Fig. 3.5, is highly anisotropic with respect to the crystalline axes. Therefore, its contribution can vary over a large range depending on the orientation of the TI flake relative to the waveguide, which is uncontrolled in our fabrication process. Fig. 3.13(b) summarizes the measured results, for the TM mode and at a fixed modulation frequency of 110 Hz, from four devices (A-D) with varying length l of the TI between the longitudinal electrode pairs. The results indeed show a large variation in terms of the relative contribution of photocurrent between the CPGE and LPGE effects. In samples where LPGE overwhelms the CPGE, the total photocurrent will not reverse sign with the change of light propagation direction, but its magnitude will vary because of the reversal of the CPGE contribution. Characterization methods such as micro-Raman spectroscopy can be employed to determine the crystalline orientation of the Bi_2Se_3 flake. Therefore, it is possible to precisely align the orientation of the flake with the waveguide to minimize or even completely remove the LPGE contribution from the bulk to obtain a highly asymmetric, helicity-dependent photoresponse with respect to the light propagation direction in the waveguide.

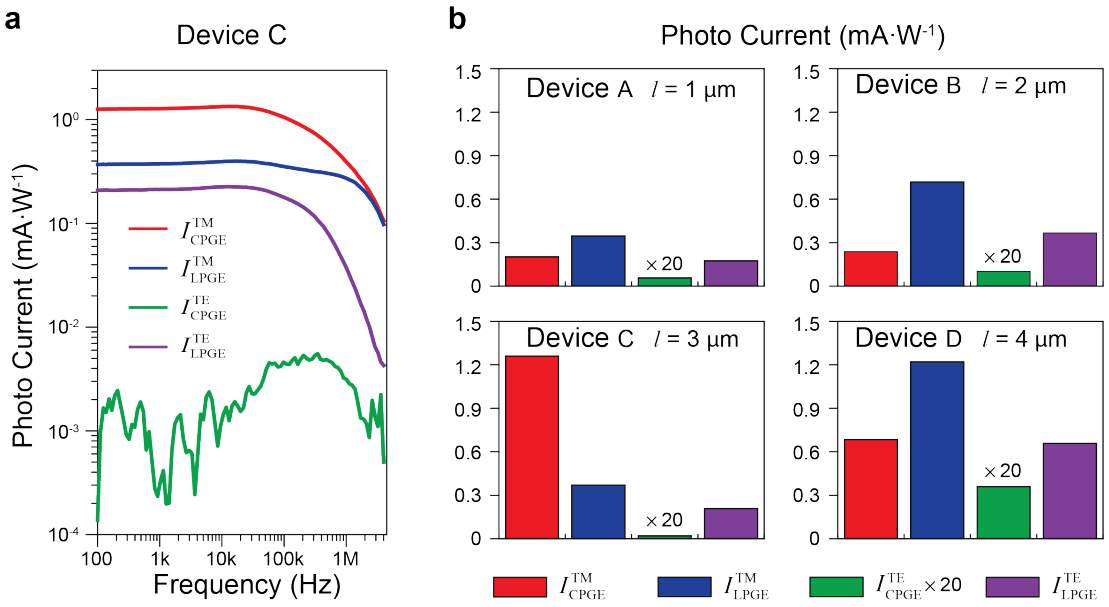

Figure 3.13: Contributions of circular and linear photogalvanic currents. (a) Frequency response of the extracted CPGE and LPGE contributions of photogalvanic current for TM and TE modes in Device C. (b) CPGE and LPGE contributions for TM and TE modes in four devices with different TI lengths l between the electrodes from 1 to 4 μm. A large variation of the ratio between the CPGE and the LPGE contributions is attributed to the high anisotropy of the LPGE, which is sensitive to the crystalline orientation of the Bi_2Se_3 flake to the waveguide.

3.3.3 Discussion

To date, the optical wavelength used in our experiments or similar studies in the literatures are in near-infrared or visible range with the photon energies much higher than the bulk band gap (~ 0.3 eV in Bi_2Se_3). However, the optical transitions between spin-polarized surface states within a single Dirac cone requires light in the mid-infrared wavelength range, which remains unexplored in these experiments. In addition, the TI samples used in our studies are obtained through mechanical exfoliation from the bulk crystals, which suffers from high intrinsic doping and are incapable of tuning Fermi level through electrical gating. This

significantly limits the possible optical transitions that can be observed experimentally. To address these issues, thin TI films ($\sim 10\,\mathrm{nm}$) prepared by molecular beam epitaxy should be used in future experiments to study the photogalvanic effects.

Furthermore, it is of great importance to study the spin lifetime of the photo-induced bulk or surface carriers and verify the spin polarization in the CPGE photocurrent using time-resolved magneto-optic Kerr microscopy with a femtosecond laser [67, 68]. The spin lifetime characterization of the photo-induced carriers is crucial for the generation and control of spin-polarized current in TIs, which may find applications in spintronics.

3.4 Conclusion

In this chapter, we have studied the optical manipulation of surface electrons in 3D topological insulators Bi_2Se_3 using circularly polarized light. Through circular photogalvanic effect, we demonstrate a helicity-dependent interface between the optical modes in a photonic waveguide and the surface electrons of topological insulators that directly converts the spin angular momentum of the guided photons to the spin-polarized photocurrent flowing on the surface of the TI. The helicity-dependence of the interaction stems from the spin-momentum locking effects for both photons and electrons and their coupling in an integrated platform. More broadly, our device represents a new way of implementing coupled spin-orbit interaction of both electrons and photons. The device can be utilized as an optically pumped source of spin-polarized current that may find applications in spintronics. To this end, an important next step is to verify the spin polarization in the CPGE photocurrent with techniques such as magneto-optic Kerr effect and

non-local potentiometric measurement using magnetic contacts. Furthermore, the device converts the path information of photon propagation to the spin polarization of the electrical current and can be used as an interface between photon qubits and spin qubits in a hybrid system of quantum information processing.

Chapter 4

All-Optical Switching of Magnetization in Ferrimagnetic Alloy GdFeCo

4.1 Introduction

To study the magnetization switching of magnetic thin films and nanostructures in an ultrafast time scale not only is of fundamental research interest but also has tremendous impacts on information processing and storage. For example, the logical bits are stored as the magnetization of magnetic domains in various magnetic devices (like magnetoresistive random-access memory (MRAM) and magnetic recording), and how fast the magnetization can be switched between two metastable states determines the device operation speed. The most conventional approach for magnetization switching is to use external magnetic fields, in which the magnetic moments spiral into the direction of the magnetic fields by means of precession. However, as will be shown later, the associated Larmor precession

frequency is proportional to the magnetic field strength and the switching speed is limited to the nanosecond time scale even for a high magnetic field due to the slow spin-lattice relaxation process ($\sim$100 ps) [69]. Moreover, the large integration of magnetic devices requires materials with large magnetic anisotropy, which also increases the switching field strength generated through electrical current. Therefore, the ultrafast control of magnetism without using magnetic fields is essential for the integration of spintronic devices in a large scale for memory, computation, and communication in the beyond-CMOS ear [70–74]. Mechanisms including spin transfer torque [75], spin Hall effect [76], and electric field or strain-assisted switching [77, 78] have been implemented to switch magnetization in various spintronic devices. However, their speed is also fundamentally limited by the spin precession time to longer than 10 ps $\sim$ 1 ns. Such a time constraint severely limits the possible operation speed of spintronic devices, and therefore, overcoming it is critical for the prospective development of spintronics.

Over the last decades, there has been a surge of interest in exploring the all-optical manipulation of magnetic order in various magnetic systems in a time scale of the exchange interaction using femtosecond laser pulses as the ultrafast stimuli [69]. In pioneering work, Beaurepaire et. al. performed the spin dynamics measurement on a metallic ferromagnetic Ni thin film using a magneto-optic pump-probe scheme [79]. It was shown that the magnetization of a 20 nm thick Ni film dropped accompanied a drastic increasing in electron and spin temperatures within 1 ps after the absorption of the 60 fs laser pulses (Fig.4.1), indicating the observed ultrafast demagnetization is due to electron-spin relaxation (characteristic time scale of $\sim$100 fs) rather than the conventional spin-lattice relaxation (characteristic time scale of $\sim$100 ps).

In 2007, Stanciu et. al. demonstrated that the optical excitation using 40 fs

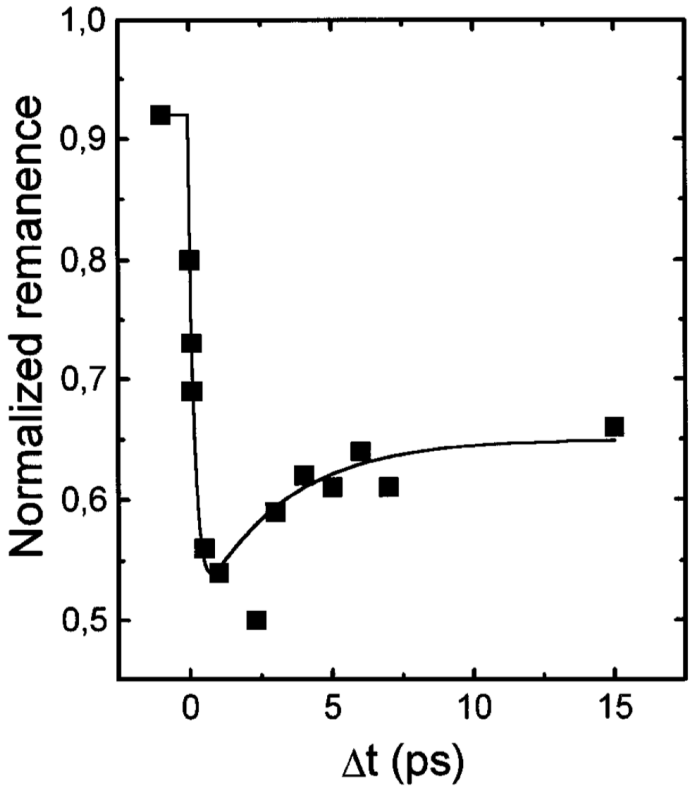

Figure 4.1: Ultrafast spin dynamics in a Ni thin film. Time-resolved magneto-optic Kerr microscopy signal of a Ni(20 nm)/MgF 2(100 nm) film after the excitation of single 60 fs laser pulses. Reproduced with permission from [79]

laser pulses alone could even lead to the ultrafast magnetization switching (∼3 ps) in metallic ferrimagnetic alloy GdFeCo [80], where Gd and FeCo sublattices are anti-ferromagnetically coupled. In particular, regardless the initial magnetization direction, the final magnetization state after laser excitation was shown to be solely dependent on light polarization (σ^+ or σ^-). For example, in Fig. 4.2, σ^+ (σ^-) laser pulses set the final magnetization to up (down) state, represented as white (black) small domains. Therefore, the demonstrated all-optical switching is light helicity-dependent and the film magnetization can be manipulated in a

completely deterministic manner by controlling light polarization.

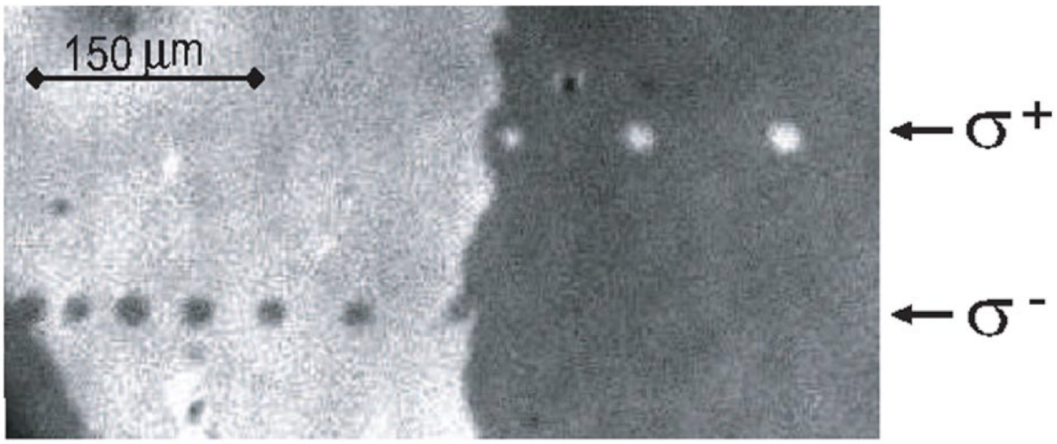

Figure 4.2: Helicity-dependent all-optical magnetic switching in GdFeCo. Small magnetic domains were generated by sweeping pulsed laser beams across the GdFeCo sample. The domain magnetization was determine by light helicity. Reproduced with permission from [80]

Since the first discovery of all-optical switching (AOS) in GdFeCo alloy, the underlying mechanism that governs the ultrafast spin dynamics has been a subject of hot debate. The switching mechanism was first proposed as the joint effects of ultrafast laser heating of the magnetic system to below the Curie temperature and the effective magnetic field induced by light through the inverse Faraday effect [80, 81]. In particular, the polarity of the effective magnetic field is determined by light polarization (σ^+ or σ^-) and thus the final magnetization state is dependent on light helicity. However, in 2012, Khorsand et. al. had a contradictory observation that all-optical switching in GdFeCo can always be achieved once the optical absorption in the film is above a threshold value [82]. The previously observed helicity-dependence in magnetization switching is due to the magnetic circular dichroism that films' optical absorption varies for polarized light with opposite helicity. Therefore, the switching behavior should be

universal regardless light polarization or wavelength. Not long after, a series of theoretical and experimental studies have revealed that the observed magnetization switching in GdFeCo is a pure thermal effect, which involves the energy and angular momentum exchange between three thermodynamic reservoirs (electron, spin and lattice) [83–85]. Although the fundamental researches regarding all-optical magnetization switching in various material systems and structures are still going on [86, 87], all-optical switching of magnetization has been proposed to be promising for a plethora of applications, including ultrafast magnetic recording, non-volatile magnetic memory, and spin logics.

In this chapter, we will present the experimental study of all-optical switching in ferrimagnetic alloy GdFeCo and its use in device implementation using telecom-band femtosecond laser pulses ($\lambda = 1.55\,\mu m$) as the ultrafast stimuli. First, to illustrate the very distinct all-optical switching mechanism from other magnetization switching approaches through spin precession, we start with a brief review of the dynamics of magnetic moments in (effective) magnetic fields and under laser pulse excitations. Then, in the later section, we present a systematic study of all-optical switching in GdFeCo thin films with near-infrared, femtosecond optical pulses using the magneto-optic Kerr microscopy. As a step toward device applications from previous material and spectroscopic investigations, we further demonstrate the ultrafast all-optical switching of an magnetic tunnel junction (MTJ) [88–90], the building blocks of spintronic logic, using single femtosecond laser pulses [91]. This optically switchable MTJ uses GdFeCo as the free layer and its switching is read out by measuring its tunneling magnetoresistance with a $\Delta R/R$ ratio of 0.6%. A switching repetition rate at 1 MHz has been demonstrated, but the fundamental upper limit should be higher than tens of GHz rate. This result represents an important step toward integrated opto-spintronic devices

that combines spintronics and photonics technologies to enable ultrafast conversion between fundamental information carriers of electron spins and photons.

4.2 Dynamics of magnetic moments

4.2.1 Dynamics of magnetic moments in magnetic fields

The magnetic moment $\mathbf{m}$ of a charged particle is related to its angular momentum $\mathbf{j}$ through the gyromagnetic ratio γ as $\mathbf{m} = \gamma \times \mathbf{j}$. Therefore, in classical mechanics, the motion of $\mathbf{m}$ in an external magnetic field is determined by the torque applied on it, and is given by the Landau-Lifshitz (LL) equation:

$$\partial_t \mathbf{m} = -\gamma \mathbf{m} \times \mathbf{H} \tag{4.1}$$

The LL equation describes the precessional motion of $\mathbf{m}$ in the plane perpendicular to $\mathbf{H}$ periodically at the Larmor frequency $\omega = \gamma H$, which is linearly proportional to $\mathbf{H}$. For a magnetic solid with homogenous magnetization, the magnetic field $\mathbf{H}$ on the right side of the LL equation should also include the contributions from effects such as shape anisotropy, magnetocrystalline anisotropy, spin injection etc., so that $\mathbf{H}$ is replaced with an effective field $\mathbf{H}_{\text{eff}}$.

In general, a damping term proportional to the precession velocity $\partial_t \mathbf{m}$ (the dimensionless damping coefficient λ is assumed to be positive) is added to the right hand of the equation of motion to account for the phenomenological friction in the precession process, and therefore, the new equation of motion is given by the Landau-Lifshitz-Gilbert (LLG) equation

$$\partial_t \mathbf{m} = -\gamma \mathbf{m} \times \mathbf{H}_{\text{eff}} - \gamma \lambda \frac{\mathbf{m}}{|\mathbf{m}|} \times (\mathbf{m} \times \mathbf{H}_{\text{eff}}) \tag{4.2}$$

Note that the motion of $\mathbf{m}$ described by the LLG equation can be viewed as a vector with fixed length traverses on the Poincare sphere, since the two torque

terms on the right side of the LLG equation are perpendicular to $\mathbf{m}$ and thus $|\mathbf{m}|$ is conserved. When a magnetic field $\mathbf{H}_{\text{eff}}$ is applied opposite to $\mathbf{m}$, according to the LLG equation, $\mathbf{m}$ will first deviates from its equilibrium position pointing anti-parallel to $\mathbf{H}_{\text{eff}}$ due to thermal fluctuation and then spiral into the direction of $\mathbf{H}_{\text{eff}}$ through the exchange of energy and angular momentum between spin and the lattice (which is manifested by the damping coefficient λ). Therefore, the speed of the magnetization switching through precession is limited by the spin-lattice relaxation time that is typically longer than 100 ps in solids.

There is a caveat about the LLG equation: $|\mathbf{m}|$ is assumed to be a constant in the dynamic evolution (macrospin approximation), which is only valid when the exchange energy is dominant over other energies of the magnetic system. However, this assumption fails when dealing with the ultrafast spin dynamics induced by femtosecond laser pulses and certain modifications are required for the LLG equation to account for the change in $|\mathbf{m}|$. It turns out that the ultrafast spin dynamics can be captured using the Landau-Lifshitz-Bloch (LLB) equation as [84]

$$\partial_t \mathbf{m} = -\gamma \mathbf{m} \times \mathbf{H}_{\text{eff}} + \gamma \lambda_{||} \frac{(\mathbf{m} \cdot \mathbf{H}_{\text{eff}})\mathbf{m}}{m^2} - \gamma \lambda_{\perp} \frac{\mathbf{m} \times (\mathbf{m} \times \mathbf{H}_{\text{eff}})}{m^2} \tag{4.3}$$

where $\lambda_{||}$ and $\lambda_{\perp}$ are longitudinal and transverse damping parameters that are dependent on electron temperature T as

$$\lambda_{||} = \lambda \frac{2T}{3T_c^{\text{MF}}},\ \lambda_{\perp} = \lambda \big[1 - \frac{T}{3T_c^{\text{MF}}}\big] \tag{4.4}$$

4.2.2 Review of the time-resolved study of all optical magnetization switching in GdFeCo

In 2011, Radu et. al. performed time-resolved study of the ultrafast magnetization dynamics in ferrimagnetic GdFeCo thin films using the element-specific X-ray magnetic circular dichroism (XMCD) technique [92]. In the experiment, linearly polarized 60 fs laser pulses with photon energy of 1.55 eV were used to instantaneously heat up the material. To probe the induced spin dynamics, 100 fs X-ray pulses with certain temporal delay with respect to the pump pulses were used to selectively probe the magnetic moments of either Gd or FeCo sublattices. Figure 4.3 shows the element-resolved magnetization dynamics of the two sublattices in a few picoseconds time scale. The striking feature is that followed by the absorption of the pump pulses, the magnetic moments of both Gd and FeCo sublattices independently relax to zero at different rates within $\sim$1 ps, which is the time scale of the exchange interaction. Because the FeCo sublattice demagnetizes much faster than the Gd sublattice, its magnetic moment crosses the zero signal line and aligns parallel to the Gd moment after $\sim$200 fs, forming a transient ferromagnetic-like state, although the two sublattices are anti-ferromagnetically coupled in the ground state. In the subsequent spontaneous relaxation, the moment of Gd sublattice keeps decreasing and eventually recovers the anti-ferromagnetic coupling with respect to the FeCo sublattice, leading to a reversed net magnetization state within $\sim$3 ps. Note that it takes more than $\sim$100 ps for the two sublattices to fully recover their magnetic moments to the level before the laser pulse excitation due to the slow cooling down of the lattice.

Apparently, the emerging transient ferromagnetic-like state is rather striking and cannot be explained within the framework of the macrospin approximation

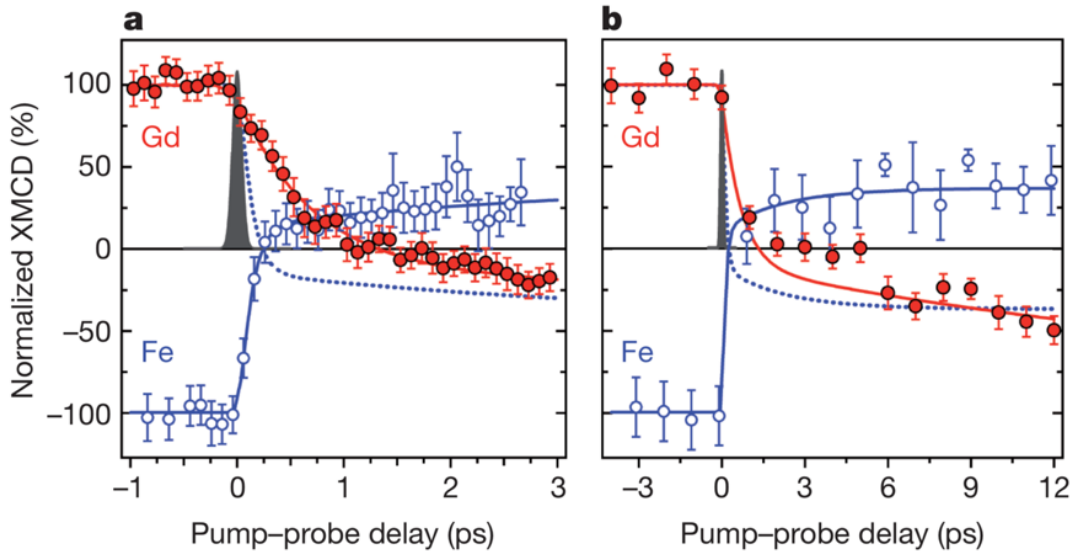

Figure 4.3: Element-resolved spin dynamics in GdFeCo measured by time-resolved XMCD. Reproduced with permission from [92].

introduced above. The key to understand the laser induced ultrafast spin dynamics is to take into account the energy and angular momentum exchange between electron, spin and lattice reservoirs, as well as the angular momentum relaxation between the two non-equivalent sublattices within the spin reservoir.

4.3 All-optical switching of magnetization with single ultrafast near infrared laser pulses

4.3.1 Material preparation and experiment setup

Material preparation

The GdFeCo films used in this study are sputtered on thermally-oxide-silicon wafers at room temperature in a magnetosputter system with a base pressure $< 5 \times 10^{-8}$ torr. The composition of GdFeCo films is controlled by varying the sputter power of Gd and $Fe_{90}Co_{10}$ targets. As shown in Fig. 4.4, the sample has a stack structure of Ta(4 nm)/$Gd_x(Fe_{90}Co_{10})_{100-x}$(20 nm)/Ta(4 nm). The 4 nm thick Ta layers are used as buffer and capping to prevent film from oxidation.

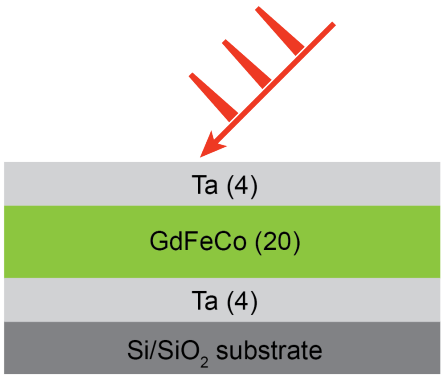

Figure 4.4: Schematic of Gd(Fe,Co) film stack.

The magnetic properties of the GdFeCo films were characterized at room temperature using vibrating sample magnetometer (VSM) and the composition of GdFeCo layer was characterized using Rutherford backscattering spectrometry (RBS). It turns out samples with Gd composition (x) in the range from 21% to 27% show good perpeicular magnetic anisotropy. Figure 4.5 shows the hysteresis

loops of the GdFeCo films with various Gd compositions. The saturation magnetization (M_s) for all samples within the above range is below 80 emu/cm^3, as these samples' compensation temperatures are close to room temperature. We also find a unidirectional shift of magnetic hysteresis loop from zero field for GdFeCo with Gd composition close to the compensation point ($x_{\mathrm{Gd}} \approx 24\%$). This shift indicates that there is an intrinsic exchange bias in the film, which exists in the exchange coupled ferromagnet/antiferromagnet structure. For example, the GdFeCo film with Gd composition of 24.8% has an exchange bias field of $\sim$ 70 Oe, as shown in Fig. 4.5. It could be attributed to the forming of zero moment GdFeCo phases inside the films where Gd and FeCo sublattice moments compensate each other during the multi-targets co-sputter deposition, which are exchange coupled with other non-zero GdFeCo phases. Similar exchange-bias behaviors have also been observed in other amorphous RE-TM alloys, such as TbFeCo and DyCo films [93, 94].

Experimental setup

All-optical magnetization switching in GdFeCo films and microstructures can be observed using magneto-optic Kerr effect (MOKE). Figure 4.6 shows the schematics of the laser excitation and magnetic domain imaging apparatus used in the AOS measurement. A 400 fs optical pulse train out from a fiber laser (Polaronyx URANUS 0500-1500) has a base repetition rate of 1 MHz. An acoustic-optic modulator (AOM) is used as a laser pulse picker, whose optical transmission is controlled by electrical pulse signals provided by a signal generator. By setting the electrical pulse width properly, single or multiple laser pulses with 1 µs temporal separation are picked out for the single shot and multiple shot experiments, respectively. Due to the lack of synchronization between optical and electrical pulses, and the finite rise/fall time ($\sim$10 ns) of the electrical pulses, laser pulse

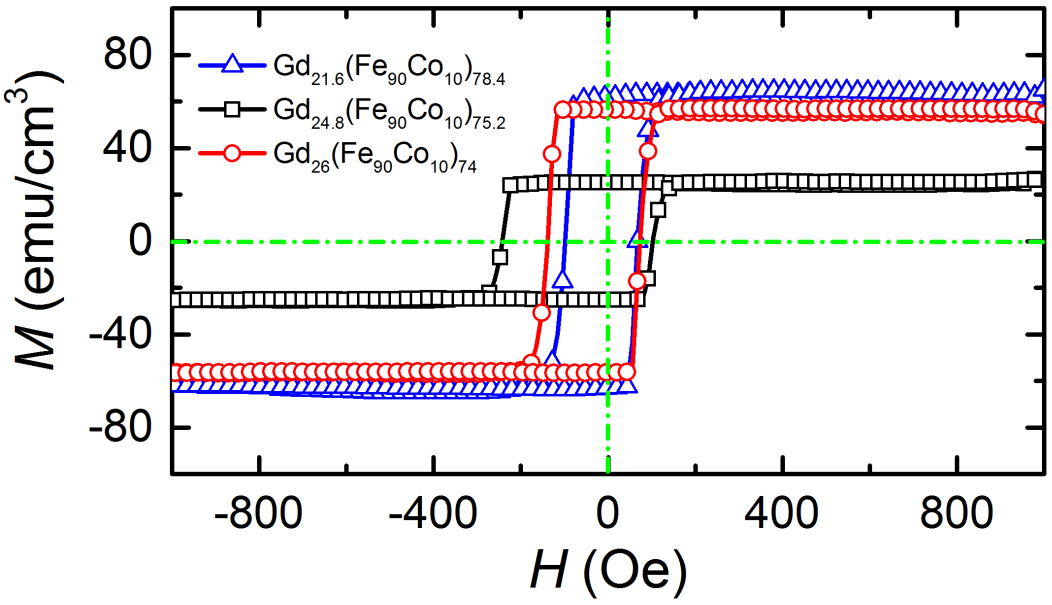

Figure 4.5: M-H Hysteresis loops of GdFeCo films with different Gd compositions.

energies may fluctuate slightly, which results in unsuccessful switching in the AOS measurement occasionally.

4.3.2 Films

To demonstrate the magnetization of GdFeCo films can be switched by a single laser pulses, we scan the laser beam across the sample surface. The laser spot diameter of 20 µm with an optical fluence of 5.8 mJ/cm^2 is used consistently throughout this work. With a low laser pulse repetition rate and high scanning speed, there is no spatial overlap between adjacent pulses. Figure 4.7(a) shows a representative MOKE image of a $Gd_{26}(Fe_{90}Co_{10})_{74}$ sample after the scan. It can be seen that individual bubble domains in size similar to the laser spot

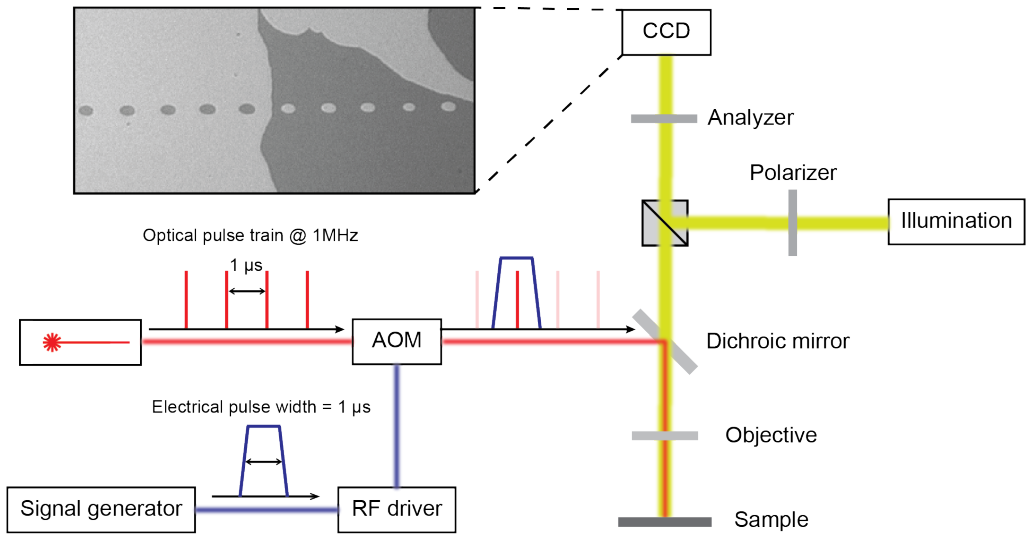

Figure 4.6: Schematics of laser excitation and magnetic domain imaging system.

have been created through AOS in domains with both up and down magnetizations. AOS in our materials is independent of the laser polarization, and the laser pulses always reverse the magnetization, which is consistent with other reports on helicity-independent AOS of GdFeCo [80, 85, 86]. Therefore, the linear polarization is used in all of our experiments. We systematically characterize the AOS in GdFeCo samples with various Gd compositions. It turns out that AOS is only observed in samples with Gd composition in the range from 22% to 26% (the grey-shadowed region in Fig. 4.7(b)), close to the point where the magnetic moments of Gd and FeCo sublattices cancel each other ($M_s = 0$) at room temperature. Our result is consistent with previous reports by several other groups using visible laser pulses [80, 85].

To further confirm that single laser pulses can toggle the film magnetization repeatedly and the observed switching is not due to the stray field and/or domain

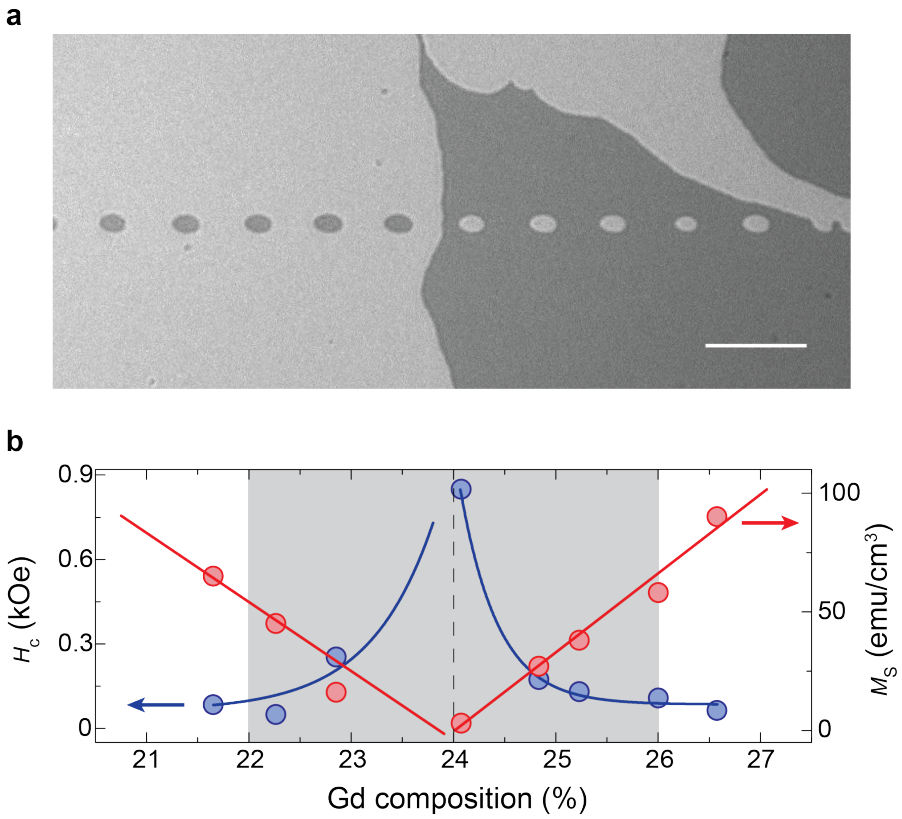

Figure 4.7: All-optical switching of GdFeCo films. (a) The MOKE image of single bubble domains crated via AOS by scanning single subpicosecond laser pulses across the boundary between two large magnetic domains in the sample. The scale bar is 100 µm. (b) The coercivity H_c (blue symbols) and saturated magnetization M_s (red symbols) of GdFeCo samples versus their Gd composition. Samples with Gd composition in the gray-shadowed region (22%-26%) show AOS behavior. The solid lines are used to guide the eyes.

walls from the surrounding area that is not exposed to laser pulses, we perform similar single laser shot experiment on a square patterned from the GdFeCo film (width = 12 µm). Figure 4.8 are the MOKE images of the patterned structure exposed to five consecutive laser pulses, showing that each pulse (except the third pulse) reverses the magnetization. We also notice that the third pulse fails to switch the square magnetization from gray to dark, but rather creates multiple domains. This failure in switching could be attributed to the fluctuation of laser pulse energy in our measurement system due to the lack of synchronization between the pulsed laser and the AOM pulse picker. Nevertheless, the fourth pulse switches the square back to gray (possibly because the patterned structure tends to form single domain in its equilibrium state). The repeatable toggling of magnetization in GdFeCo square confirms that the switching is resulted from ultrafast heating alone and the surrounding area that is not exposed to laser pulses does not play a role in AOS.

4.3.3 Hall cross

As an intermediate step towards device applications, we demonstrate the magnetoelectric response of the GdFeCo films to AOS by measuring the anomalous Hall effect (AHE). We patterned the film into pillars and deposited transparent electrodes made of 110 nm thick indium tin oxide (ITO) to measure the Hall resistance. Figure 4.9(a) shows an optical image of a typical device with a pillar diameter of 15 µm. Using an external perpendicular magnetic field (Lakeshore), the hysteresis loop of the anomalous Hall resistance (R_{AHE}) is measured. The asymmetric R_{AHE} for the up and down magnetized states is attributed to the slight asymmetry in the electrodes' position. The observed rectangular hysteresis loop shows the device has nearly 100% remanence. We next use this hall device

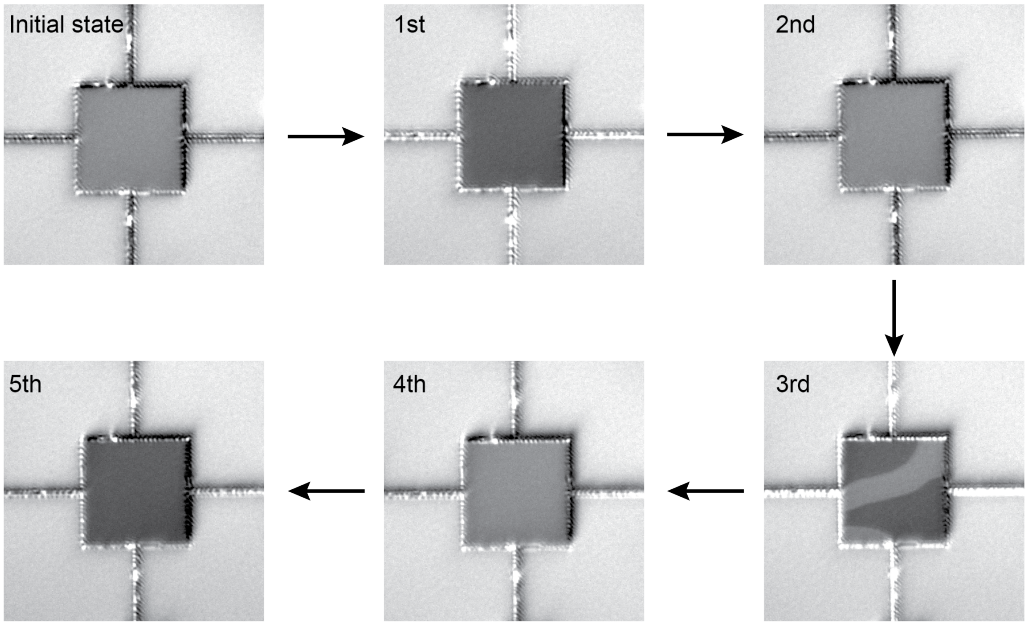

Figure 4.8: All-optical switching of patterned GdFeCo microstructures. The MOKE images of a GdFeCo square subject to five consecutive optical pulses. The thin wires are connected to metal pads for electrical measurements.

to demonstrate direct electrical readout of AOS. The pillar is exposed to a train of single laser pulses with a repetition rate of 0.5 Hz, and the Hall resistance is measured in real time. The result presented in Fig. 4.9(c) shows that the Hall resistance is reversed by every laser pulse. Comparing Fig. 4.9(b) and (c). it can be seen the values of R_{AHE} reversed by AOS in Fig. 4.9(c) are the same as in Fig. 4.9(b). This result indicates that every single laser pulse completely reverses the magnetization of the GdFeCo pillar.

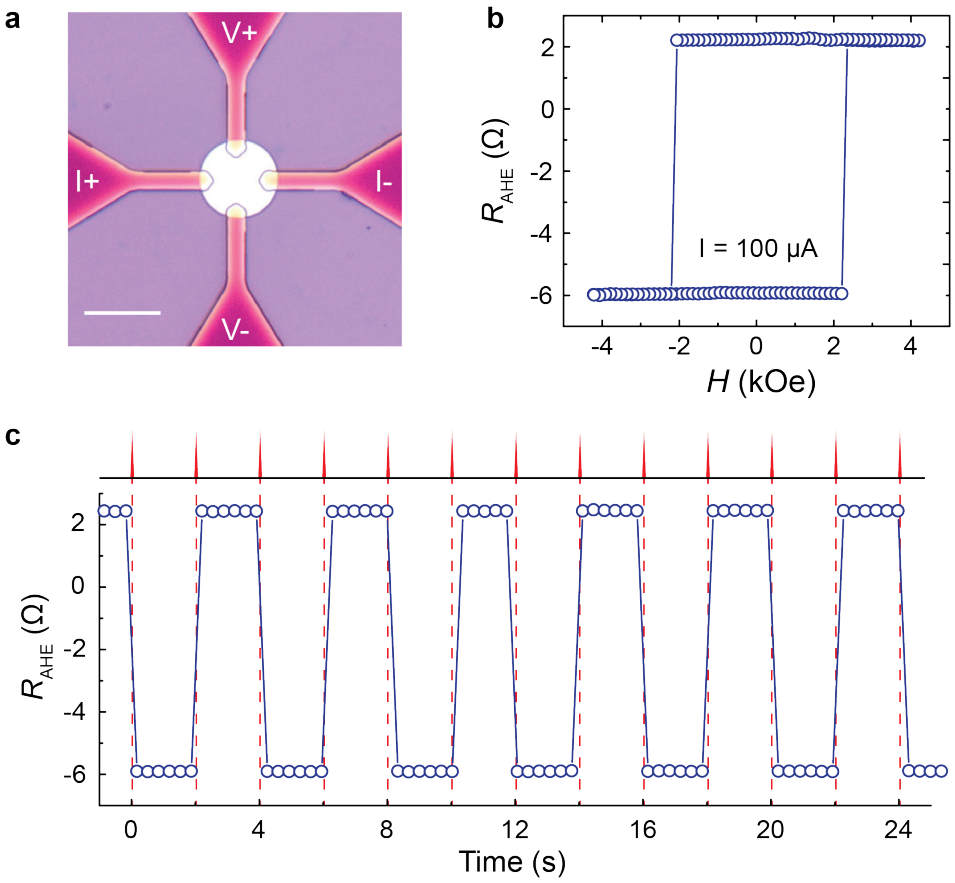

Figure 4.9: Direct magnetoelectric readout of AOS in GdFeCo film by AHE. (a) Optical microscope image of a typical Hall device with pillar diameter of 15 µm and transparent ITO/Cu electrodes. The scale bar is 15 µm. (b) R_{AHE} hysteresis loop of the device measured by sweeping a perpendicular magnetic field with a constant dc bias current of 100 µA. (c) R_{AHE} of the device measured during AOS by single laser pulses with 0.5 Hz repetition rate. The consistent change of R_{AHE} in (b) and (c) confirms that the GdFeCo pillar is completely switched by the laser pulses.

4.3.4 All-optical switching of magnetic tunnel junctions with single laser pulses

AOS has been extensively explored for its prospects of enabling ultrafast magnetic recording and operation of spintronic device. However, there has not been any demonstration of AOS in realistic spintronic devices, such as magnetic tunnel junctions. Since previous studies of AOS have been performed only on a single magnetic layer, how additional magnetic layers affect the AOS phenomenon remains unknown. Here, we demonstrate an optically switchable MTJ with fast operating speed by using the GdFeCo film as the free layer. To this end, we design and fabricate a MTJ stack in the configuration of Ta(5 nm)/Pd(10 nm)/[Co(0.6 nm)/Pd(1.5 nm)]$_{\times 4}$/Co(0.8 nm)/MgO(1.8 nm)/GdFeCo(20 nm)/Ta(4 nm), as illustrated in Fig. 4.10. The MgO layer is the tunneling barrier. The Ta and Pd layers are used as the buffer and the bottom electrodes. The Co/Pd multilayers are the fixed layer, which is optimized to obtain good perpendicular magnetic anisotropy. Notably, ITO is used as the transparent top electrode to allow optical access. Figure 4.11 shows an optical image of a representative MTJ device with a pillar diameter of 12 µm.

We measure the tunneling magnetoresistance (R_{TMR}) of the MTJ by sweeping a perpendicular magnetic field in the range of ±2 kOe. A clear TMR minor loop showing the low and high resistance states of the MTJ is measured, as shown in Fig. 4.11. Because the Gd composition is chosen to be close to compensation point, the bottom Co/Pd multilayers have a lower coercivity H_c than the GdFeCo layer, they are switched by the magnetic field while the magnetization of the GdFeCo layer remains fixed. The MTJ in the low and high resistance states have resistance of 98.0 and 98.6 Ω, respectively. Therefore, the TMR ratio defined as

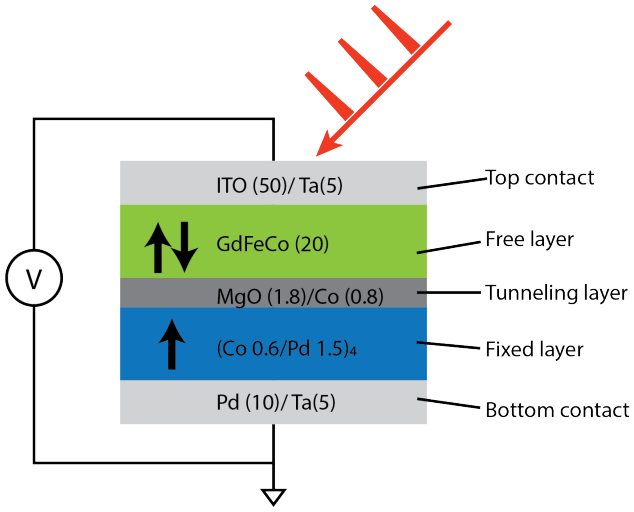

Figure 4.10: Schematic of the MTJ stacks.

$\Delta R_{\mathrm{TMR}}/R_{\mathrm{TMR}}$ is ~0.6%. We attribute the low TMR ratio to the low quality of the MgO layer because no post-deposition annealing is performed, and to the oxidation at the MgO/GdFeCo interface. The relatively high noise in the TMR measurement is attributed to the poor interface between the ITO and the Ta capping layers. Nevertheless, the device provides a sufficient TMR signal-to-noise ratio to discern optical switching of the MTJ.

The AOS measurement on the MTJ is performed in a similar way to the Hall device by setting the laser repetition rate at 0.5 Hz and monitoring the TMR value with an averaging time constant of 100 ms to obtain the result shown in Fig. 4.12(a). It clearly shows that each laser pulse switches the MTJ between high and low resistance states. In contrast to switching using a magnetic field, the laser pulses switch the magnetization of the GdFeCo layer that is on the top of the MTJ while the magnetization of the Co/Pd multilayers at the bottom remain fixed, as is evident in the MOKE images in Fig 4.12(b) and (c). The change of the TMR by AOS is 0.6 $\pm$ 0.05 Ω, in agreement with the value obtained in

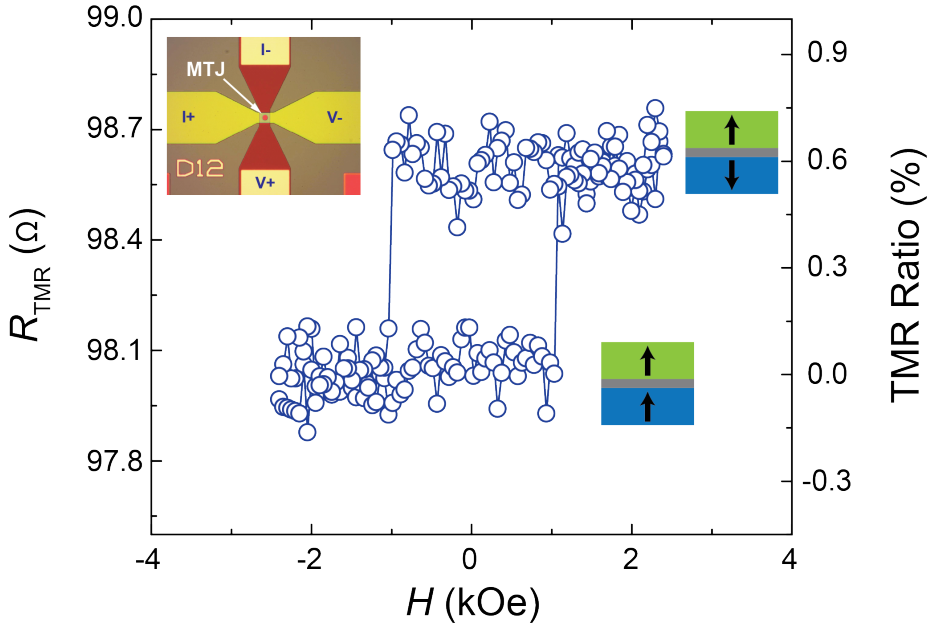

Figure 4.11: The R_{TMR} minor loop measured with external magnetic fields. Inset, Optical microscope image of a MTJ device with ITO electrodes on the top for TMR measurement.

the magnetic field measurement. We note that, in Fig 4.11 and 4.12, the slight difference in the absolute resistance values is due to the changed probe-to-device contact resistance in two different measurement setups. The consistent change of the TMR value unambiguously confirms that the GdFeCo layer in the MTJ has been completely switched via AOS. The TMR ratio in this device can be increased by exchange coupling the GdFeCo layer with a ferromagnetic layer, such as CoFe and CoFeB [95, 96], and by annealing to improve the quality of MgO layer. Our result represents a demonstration of all-optical switching of a realistic spintronic device by using ultrafast laser pulses.

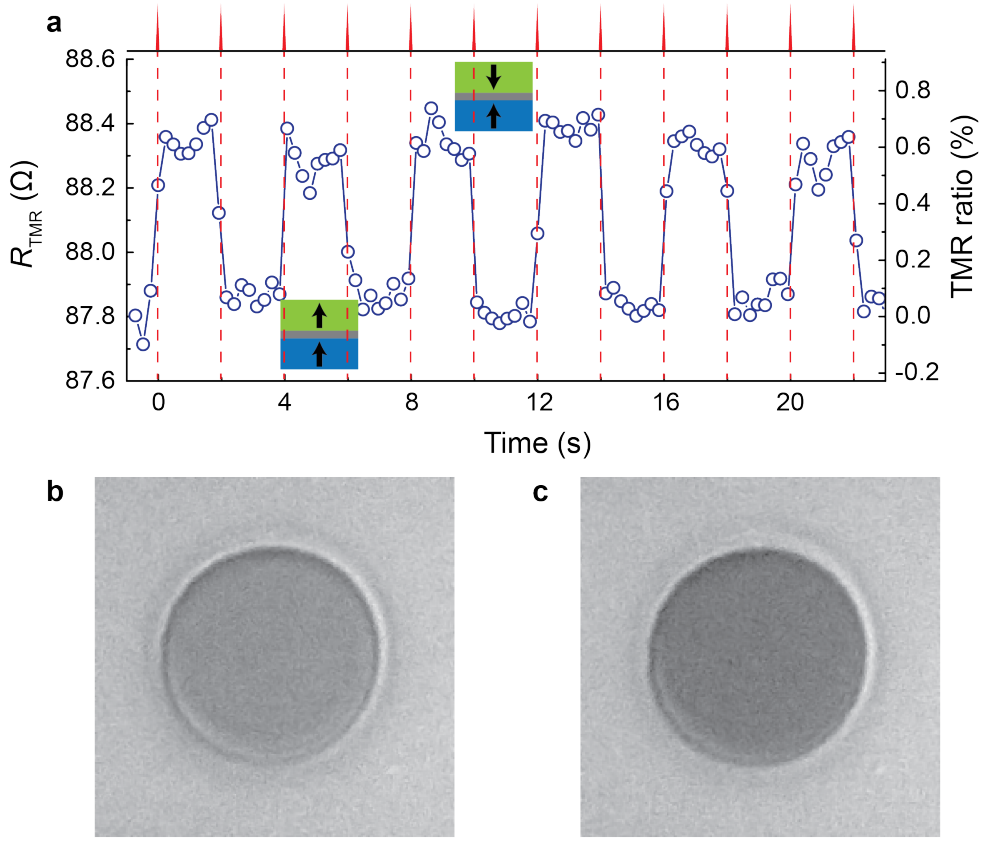

Figure 4.12: AOS of an MTJ with subpicosecond single laser pulses. (a) R_{TMR} of the MTJ device measured during AOS by 0.4 ps single laser pulses at 0.5 Hz repetition rate. The change of R_{TMR} in (a) and Fig. 4.11 have the same value of $\sim$0.6 $\pm$ 0.05 Ω, indicating the GdFeCo layer has been completely switched. (b)-(c) The MOKE images of the MTJ pillar before and after AOS by a single laser pulse, showing the GdFeCo layer is completely switched.

4.3.5 Switching speed

According to the previous time-resolved spin dynamics study (Fig. 4.3), the net magnetization of the GdFeCo films can be switched by a femtosecond optical pulses within ∼3 ps, however, the complete recover of the magnetic moments of each sublattices to the equilibrium value takes much longer time of ∼100 ps due to the slow cooling down of the lattice. Therefore, how fast the GdFeCo magnetization in a realistic spintronic device can be switched is of great technological importance for the high-speed device operation. To this end, we demonstrate the repeatability of AOS using a GdFeCo Hall cross device similar to the one in Fig. 4.9. The device is exposed to trains of multiple pulses with the time spacing of 1 µs, generated using the pulse picker. Since our laser's base repetition rate is 1 MHz, even shorter time spacing is not possible. Figure 4.13 shows that, when the device is exposed to two consecutive pulses, the second pulse, 1 µs after the first pulse, switches the device again and thus resets the device to its original state. As a result, no change of R_{AHE} is observed because a measurement time constant of 20 ms is used. Similarly, when the device is exposed to three and four consecutive pulses, the third pulse switches the device again, so that change of R_{AHE} resumes, and the fourth pulse resets the device. This result demonstrates a 1 MHz AOS repetition rate of a GdFeCo Hall cross device. However, the fundamental switching rate of GdFeCo should be much higher and requires further investigation.

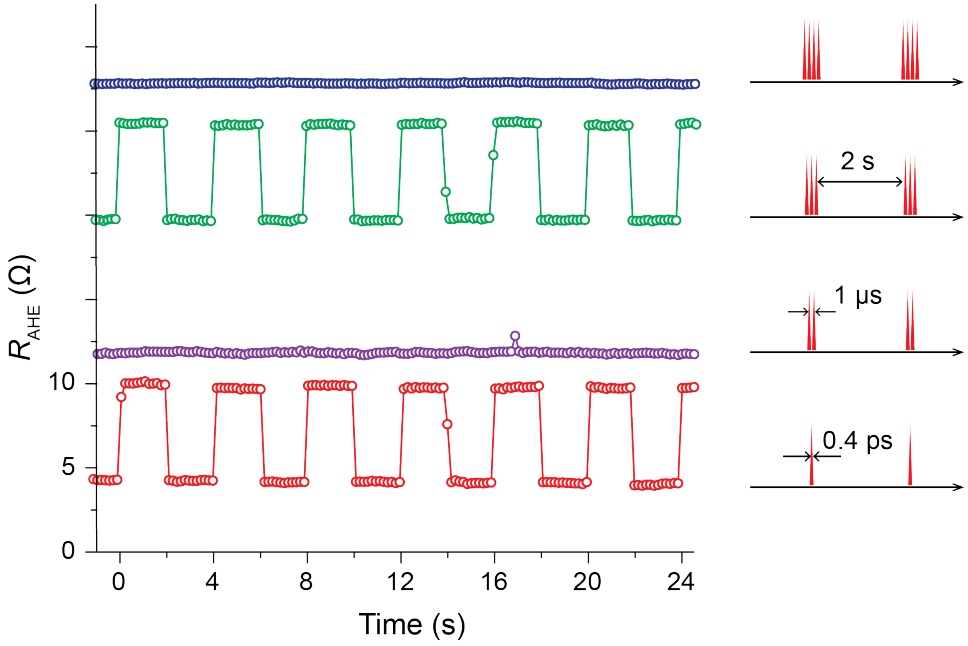

Figure 4.13: Repetitive AOS of the GdFeCo Hall device. The GdFeCo Hall device is exposed to trains of single (red), dual (purple), three (green), and four (blue) consecutive pulses with 1 μs pulse-to-pulse time spacing and the AHE resistance is measured. The device is switched repetitively by the pulses: the second pulse resets the switching by the first pulse and the fourth pulse resets the switching by the third pulse. Therefore, no R_{AHE} change is measured for trains of double and quadruple pulses. The result demonstrates 1 MHz AOS repetition rate.

4.4 Discussion

In conclusion, we have integrated an optically switchable Gd(Fe,Co) film into an MTJ device and have demonstrated ultrafast all-optical switching of this spintronic device using subpicosecond laser pulses. The picosecond time scale of optical switching is 2 orders of magnitude faster than other switching methods. The use of telecom-band infrared laser sources also makes such devices compatible for integration with silicon photonics and fiber optics. Future work to improve the TMR ratio of the optically switchable MTJ and reduce the required optical fluence for switching is necessary to enable large-scale integration and practical applications. The energy per pulse required for AOS scales inversely with the device area and the efficiency of AOS also improves with the reduced device area [97]. Therefore, for an AOS device with subwavelength dimensions [98, 99], femtojoule pulse energy should be sufficient to switch it. The presented results pave a path toward a new category of optospintronic devices, which can directly convert ultrafast optical signals into the nonvolatile magnetic states of spintronic structures and thus may find novel applications combining photonic and magnetic technologies.

Chapter 5

Concluding Remarks

This dissertation has discussed three scenarios that involve angular momentum transfer in the process of light-matter interaction.

In chapter 2, we presented the measurement of spin angular momentum of photons propagating in a birefringent waveguide. We demonstrated an on-chip optomechanical seesaw device to amplify and transduce the optical torque generated in the silicon waveguide. Our quantitative torque measurement reveals that the photon spin angular momentum in the waveguide is slightly larger than the value in vacuum, suggests that Minkowski momentum applies in our system. The result shows that the optical torque is determined by the geometric birefringence of the waveguide and is independent of optical frequency. Therefore, it can be implemented in other nanophotonic structures to generate even more pronounced effects. In general, our device provides a sensitive detection to the rotational motion of microstructures and can be potentially used in applications such as optomechanical gyroscopes and torsional magnetometry.

In chapter 3, we studied the photogalvanic effects in 3D topological insulator Bi_2Se_3. Through circular photogalvanic effect, we demonstrate a helicity-dependent interface between the optical modes in a photonic waveguide and the surface electrons of topological insulators that directly converts the spin angular momentum of the guided photons to the spin-polarized photocurrent of the TI. The device can be utilized as an optically pumped source of spin-polarized current that may find applications in spintronics. To this end, an important next step is to verify the spin polarization in the CPGE photocurrent with techniques such as magneto-optic Kerr effect and non-local potentiometric measurement using magnetic contacts.

In chapter 4, we studied the ultrafast all-optical magnetic switching in ferrimagnetic alloy Gd(FeCo) using sub-picosecond near-infrared laser pulses. By integrating Gd(FeCo) as the free layer, we further demonstrated an optically switchable magnetic tunnel junction with a TMR ratio of 0.6%. A switching repetition rate at 1 MHz has been demonstrated, but the fundamental upper limit should be higher than tens of GHz rate. Further studies are required to improve the device performance towards practical applications. For example, the TMR ratio of this device can be potentially increased by exchange coupling the GdFeCo layer with a ferromagnetic layer, such as CoFe and CoFeB, and by annealing to improve the quality of MgO layer. In terms of device operation speed, the ultimate switching time can be determined by measuring its response to two consecutive pulses with short (sub-nanosecond) temporal spacing using time-resolved pump-probe scheme. Furthermore, since the energy per pulse required for AOS scales inversely with the device area, to study the AOS behavior in devices with sub-wavelength dimension is a important step towards energy-efficient and large scale AOS spintronic devices.

References

[1] Beth, R.A. "Mechanical detection and measurement of the angular momentum of light." *Physical Review*, *50*, 2: p. 115, 1936.

[2] He, L.; Li, H.; and Li, M. "Optomechanical measurement of photon spin angular momentum and optical torque in integrated photonic devices." *Science advances*, *2*, 9: p. e1600485, 2016.

[3] Ganichev, S.D. and Prettl, W. "Spin photocurrents in quantum wells." *Journal of physics: Condensed matter*, *15*, 20: p. R935, 2003.

[4] Farshchi, R.; Ramsteiner, M.; Herfort, J.; Tahraoui, A.; and Grahn, H. "Optical communication of spin information between light emitting diodes." *Applied Physics Letters*, *98*, 16: p. 162508, 2011.

[5] Lodahl, P.; Mahmoodian, S.; Stobbe, S.; Rauschenbeutel, A.; Schneeweiss, P.; Volz, J.; Pichler, H.; and Zoller, P. "Chiral quantum optics." *Nature*, *541*, 7638: p. 473, 2017.

[6] Barnett, S.M. and Loudon, R. "On the electromagnetic force on a dielectric medium." *Journal of Physics B: Atomic, Molecular and Optical Physics*, *39*, 15: p. S671, 2006.

[7] Nichols, E.F. and Hull, G. "A preliminary communication on the pressure of heat and light radiation." *Physical Review (Series I)*, *13*, 5: p. 307, 1901.

[8] Lebedew, P. "Untersuchungen über die druckkräfte des lichtes." *Annalen der Physik*, *311*, 11: pp. 433–458, 1901.

[9] Li, M.; Pernice, W.; and Tang, H. "Tunable bipolar optical interactions between guided lightwaves." *Nature Photonics*, *3*, 8: p. 464, 2009.

[10] Liu, V.; Povinelli, M.; and Fan, S. "Resonance-enhanced optical forces between coupled photonic crystal slabs." *Optics express*, *17*, 24: pp. 21897–21909, 2009.

[11] Rakich, P.T.; Popović, M.A.; and Wang, Z. "General treatment of optical forces and potentials in mechanically variable photonic systems." *Optics express*, *17*, 20: pp. 18116–18135, 2009.

[12] Woolf, D.; Loncar, M.; and Capasso, F. "The forces from coupled surface plasmon polaritons in planar waveguides." *Optics express*, *17*, 22: pp. 19996–20011, 2009.

[13] Aspelmeyer, M.; Kippenberg, T.J.; and Marquardt, F. "Cavity optomechanics." *Reviews of Modern Physics*, *86*, 4: p. 1391, 2014.

[14] Marquardt, F. and Girvin, S.M. "Optomechanics (a brief review)." *arXiv preprint arXiv:0905.0566*, 2009.

[15] Li, M.; Pernice, W.; Xiong, C.; Baehr-Jones, T.; Hochberg, M.; and Tang, H. "Harnessing optical forces in integrated photonic circuits." *Nature*, *456*, 7221: p. 480, 2008.

[16] Chan, J.; Alegre, T.M.; Safavi-Naeini, A.H.; Hill, J.T.; Krause, A.; Gröblacher, S.; Aspelmeyer, M.; and Painter, O. "Laser cooling of a nanomechanical oscillator into its quantum ground state." *Nature*, *478*, 7367: p. 89, 2011.

[17] Safavi-Naeini, A.H.; Chan, J.; Hill, J.T.; Alegre, T.P.M.; Krause, A.; and Painter, O. "Observation of quantum motion of a nanomechanical resonator." *Physical Review Letters*, *108*, 3: p. 033602, 2012.

[18] Loke, V.L.; Asavei, T.; Stilgoe, A.B.; Nieminen, T.A.; and Rubinsztein-Dunlop, H. "Driving corrugated donut rotors with laguerre-gauss beams." *Optics Express*, *22*, 16: pp. 19692–19706, 2014.

[19] Ukita, H. and Kawashima, H. "Optical rotor capable of controlling clockwise and counterclockwise rotation in optical tweezers by displacing the trapping position." *Applied optics*, *49*, 10: pp. 1991–1996, 2010.

[20] Hill, P.M.; Olshansky, R.; and Burns, W. "Optical polarization division multiplexing at 4 gb/s." *IEEE photonics technology letters*, *4*, 5: pp. 500–502, 1992.

[21] O'brien, J.L.; Furusawa, A.; and Vučković, J. "Photonic quantum technologies." *Nature Photonics*, *3*, 12: p. 687, 2009.

[22] Politi, A.; Cryan, M.J.; Rarity, J.G.; Yu, S.; and O'brien, J.L. "Silica-on-silicon waveguide quantum circuits." *Science*, *320*, 5876: pp. 646–649, 2008.

[23] Dai, D.; Liu, L.; Gao, S.; Xu, D.X.; and He, S. "Polarization management for silicon photonic integrated circuits." *Laser & Photonics Reviews*, *7*, 3: pp. 303–328, 2013.

[24] Silverstone, J.W.; Bonneau, D.; Ohira, K.; Suzuki, N.; Yoshida, H.; Iizuka, N.; Ezaki, M.; Natarajan, C.M.; Tanner, M.G.; Hadfield, R.H.; *et al.* "On-chip quantum interference between silicon photon-pair sources." *Nature Photonics*, *8*, 2: p. 104, 2014.

[25] Rakich, P.T.; Davids, P.; and Wang, Z. "Tailoring optical forces in waveguides through radiation pressure and electrostrictive forces." *Optics express*, *18*, 14: pp. 14439–14453, 2010.

[26] Joannopoulos, J.D.; Johnson, S.G.; Winn, J.N.; and Meade, R.D. *Photonic crystals: molding the flow of light*. Princeton university press, 2011.

[27] Hauer, B.; Doolin, C.; Beach, K.; and Davis, J. "A general procedure for thermomechanical calibration of nano/micro-mechanical resonators." *Annals of Physics*, *339*: pp. 181–207, 2013.

[28] Salapaka, M.; Bergh, H.; Lai, J.; Majumdar, A.; and McFarland, E. "Multi-mode noise analysis of cantilevers for scanning probe microscopy." *Journal of Applied Physics*, *81*, 6: pp. 2480–2487, 1997.

[29] Ilic, B.; Krylov, S.; Aubin, K.; Reichenbach, R.; and Craighead, H. "Optical excitation of nanoelectromechanical oscillators." *Applied Physics Letters*, *86*, 19: p. 193114, 2005.

[30] Metzger, C.H. and Karrai, K. "Cavity cooling of a microlever." *Nature*, *432*, 7020: p. 1002, 2004.

[31] Li, H. and Li, M. "Optomechanical photon shuttling between photonic cavities." *Nature nanotechnology*, *9*, 11: p. 913, 2014.

[32] Hopcroft, M.A.; Nix, W.D.; and Kenny, T.W. "What is the young's modulus of silicon?" *Journal of microelectromechanical systems*, *19*, 2: pp. 229–238, 2010.

[33] Zhao, Y. and Alù, A. "Manipulating light polarization with ultrathin plasmonic metasurfaces." *Physical Review B*, *84*, 20: p. 205428, 2011.

[34] Allen, L.; Barnett, S.M.; and Padgett, M.J. *Optical angular momentum*. CRC Press, 2003.

[35] Bliokh, K.Y.; Rodríguez-Fortuño, F.; Nori, F.; and Zayats, A.V. "Spin–orbit interactions of light." *Nature Photonics*, *9*, 12: p. 796, 2015.

[36] Bhattacharya, M. "Rotational cavity optomechanics." *JOSA B*, *32*, 5: pp. B55–B60, 2015.

[37] Burgess, J.; Fraser, A.; Sani, F.F.; Vick, D.; Hauer, B.; Davis, J.; and Freeman, M. "Quantitative magneto-mechanical detection and control of the barkhausen effect." *Science*, *339*, 6123: pp. 1051–1054, 2013.

[38] Wu, M.; Wu, N.L.Y.; Firdous, T.; Sani, F.F.; Losby, J.E.; Freeman, M.R.; and Barclay, P.E. "Nanocavity optomechanical torque magnetometry and radiofrequency susceptometry." *Nature nanotechnology*, *12*, 2: p. 127, 2017.

[39] Klitzing, K.v.; Dorda, G.; and Pepper, M. "New method for high-accuracy determination of the fine-structure constant based on quantized hall resistance." *Physical Review Letters*, *45*, 6: p. 494, 1980.

[40] Thouless, D.J.; Kohmoto, M.; Nightingale, M.P.; and Den Nijs, M. "Quantized hall conductance in a two-dimensional periodic potential." *Physical Review Letters*, *49*, 6: p. 405, 1982.

[41] Berry, M.V. "Quantal phase factors accompanying adiabatic changes." *Proceedings of the Royal Society of London. A. Mathematical and Physical Sciences*, *392*, 1802: pp. 45–57, 1984.

[42] von Klitzing, K. "Developments in the quantum hall effect." *Philosophical Transactions of the Royal Society of London A: Mathematical, Physical and Engineering Sciences*, *363*, 1834: pp. 2203–2219, 2005.

[43] Haldane, F.D.M. "Model for a quantum hall effect without landau levels: Condensed-matter realization of the" parity anomaly"." *Physical Review Letters*, *61*, 18: p. 2015, 1988.

[44] Kane, C.L. and Mele, E.J. "Z 2 topological order and the quantum spin hall effect." *Physical review letters*, *95*, 14: p. 146802, 2005.

[45] Hasan, M.Z. and Kane, C.L. "Colloquium: topological insulators." *Reviews of Modern Physics*, *82*, 4: p. 3045, 2010.

[46] Kane, C.L. and Mele, E.J. "Quantum spin hall effect in graphene." *Physical review letters*, *95*, 22: p. 226801, 2005.

[47] Bernevig, B.A.; Hughes, T.L.; and Zhang, S.C. "Quantum spin hall effect and topological phase transition in hgte quantum wells." *Science*, *314*, 5806: pp. 1757–1761, 2006.

[48] König, M.; Wiedmann, S.; Brüne, C.; Roth, A.; Buhmann, H.; Molenkamp, L.W.; Qi, X.L.; and Zhang, S.C. "Quantum spin hall insulator state in hgte quantum wells." *Science*, *318*, 5851: pp. 766–770, 2007.

[49] Fu, L.; Kane, C.L.; and Mele, E.J. "Topological insulators in three dimensions." *Physical review letters*, *98*, 10: p. 106803, 2007.

[50] Moore, J.E. and Balents, L. "Topological invariants of time-reversal-invariant band structures." *Physical Review B*, *75*, 12: p. 121306, 2007.

[51] Zhang, H.; Liu, C.X.; Qi, X.L.; Dai, X.; Fang, Z.; and Zhang, S.C. "Topological insulators in bi 2 se 3, bi 2 te 3 and sb 2 te 3 with a single dirac cone on the surface." *Nature physics*, *5*, 6: p. 438, 2009.

[52] Hsieh, D.; Qian, D.; Wray, L.; Xia, Y.; Hor, Y.S.; Cava, R.J.; and Hasan, M.Z. "A topological dirac insulator in a quantum spin hall phase." *Nature*, *452*, 7190: p. 970, 2008.

[53] Xia, Y.; Qian, D.; Hsieh, D.; Wray, L.; Pal, A.; Lin, H.; Bansil, A.; Grauer, D.; Hor, Y.S.; Cava, R.J.; *et al.* "Observation of a large-gap topological-insulator class with a single dirac cone on the surface." *Nature physics*, *5*, 6: p. 398, 2009.

[54] Ganichev, S.; Ivchenko, E.; Danilov, S.; Eroms, J.; Wegscheider, W.; Weiss, D.; and Prettl, W. "Conversion of spin into directed electric current in quantum wells." *Physical review letters*, *86*, 19: p. 4358, 2001.

[55] Yuan, H.; Wang, X.; Lian, B.; Zhang, H.; Fang, X.; Shen, B.; Xu, G.; Xu, Y.; Zhang, S.C.; Hwang, H.Y.; *et al.* "Generation and electric control of spin–valley-coupled circular photogalvanic current in wse 2." *Nature nanotechnology*, *9*, 10: p. 851, 2014.

[56] Lyanda-Geller, Y.; Li, S.; and Andreev, A. "Polarization-dependent photocurrents in polar stacks of van der waals solids." *Physical Review B*, *92*, 24: p. 241406, 2015.

[57] Jiang, C.; Shalygin, V.; Panevin, V.Y.; Danilov, S.N.; Glazov, M.; Yakimova, R.; Lara-Avila, S.; Kubatkin, S.; and Ganichev, S. "Helicity-dependent photocurrents in graphene layers excited by midinfrared radiation of a co 2 laser." *Physical Review B*, *84*, 12: p. 125429, 2011.

[58] McIver, J.; Hsieh, D.; Steinberg, H.; Jarillo-Herrero, P.; and Gedik, N. "Control over topological insulator photocurrents with light polarization." *Nature nanotechnology*, *7*, 2: p. 96, 2012.

[59] Junck, A. *Theory of Photocurrents in Topological Insulators*. Ph.D. thesis, Freie Universität Berlin, 2015.

[60] Pan, Y.; Wang, Q.Z.; Yeats, A.L.; Pillsbury, T.; Flanagan, T.C.; Richardella, A.; Zhang, H.; Awschalom, D.D.; Liu, C.X.; and Samarth, N. "Helicity dependent photocurrent in electrically gated $(Bi_{1-x}\,Sb_x)_2Te_3$ thin films." *Nature communications*, *8*, 1: p. 1037, 2017.

[61] Kastl, C.; Karnetzky, C.; Karl, H.; and Holleitner, A.W. "Ultrafast helicity control of surface currents in topological insulators with near-unity fidelity." *Nature communications*, *6*: p. 6617, 2015.

[62] Duan, J.; Tang, N.; He, X.; Yan, Y.; Zhang, S.; Qin, X.; Wang, X.; Yang, X.; Xu, F.; Chen, Y.; *et al.* "Identification of helicity-dependent photocurrents from topological surface states in bi 2 se 3 gated by ionic liquid." *Scientific reports*, *4*: p. 4889, 2014.

[63] Aiello, A.; Banzer, P.; Neugebauer, M.; and Leuchs, G. "From transverse angular momentum to photonic wheels." *Nature Photonics*, *9*, 12: p. 789, 2015.

[64] Van Mechelen, T. and Jacob, Z. "Universal spin-momentum locking of evanescent waves." *Optica*, *3*, 2: pp. 118–126, 2016.

[65] Rodríguez-Fortuño, F.J.; Marino, G.; Ginzburg, P.; O?Connor, D.; Martínez, A.; Wurtz, G.A.; and Zayats, A.V. "Near-field interference for the unidirectional excitation of electromagnetic guided modes." *Science*, *340*, 6130: pp. 328–330, 2013.

[66] Bliokh, K.Y.; Bekshaev, A.Y.; and Nori, F. "Extraordinary momentum and spin in evanescent waves." *Nature communications*, *5*: p. 3300, 2014.

[67] Hsieh, D.; Mahmood, F.; McIver, J.; Gardner, D.; Lee, Y.; and Gedik, N. "Selective probing of photoinduced charge and spin dynamics in the bulk and surface of a topological insulator." *Physical Review Letters*, *107*, 7: p. 077401, 2011.

[68] Wang, M.; Qiao, S.; Jiang, Z.; Luo, S.; and Qi, J. "Unraveling photoinduced spin dynamics in the topological insulator bi 2 se 3." *Physical review letters*, *116*, 3: p. 036601, 2016.

[69] Kirilyuk, A.; Kimel, A.V.; and Rasing, T. "Ultrafast optical manipulation of magnetic order." *Reviews of Modern Physics*, *82*, 3: p. 2731, 2010.

[70] Wolf, S.; Awschalom, D.; Buhrman, R.; Daughton, J.; Von Molnar, S.; Roukes, M.; Chtchelkanova, A.Y.; and Treger, D. "Spintronics: a spin-based electronics vision for the future." *Science*, *294*, 5546: pp. 1488–1495, 2001.

[71] Ney, A.; Pampuch, C.; Koch, R.; and Ploog, K. "Programmable computing with a single magnetoresistive element." *Nature*, *425*, 6957: p. 485, 2003.

[72] Behin-Aein, B.; Datta, D.; Salahuddin, S.; and Datta, S. "Proposal for an all-spin logic device with built-in memory." *Nature nanotechnology*, *5*, 4: p. 266, 2010.

[73] Matsukura, F.; Tokura, Y.; and Ohno, H. "Control of magnetism by electric fields." *Nature nanotechnology*, *10*, 3: p. 209, 2015.

[74] Kim, J.; Paul, A.; Crowell, P.A.; Koester, S.J.; Sapatnekar, S.S.; Wang, J.P.; and Kim, C.H. "Spin-based computing: Device concepts, current status, and a case study on a high-performance microprocessor." *Proceedings of the IEEE*, *103*, 1: pp. 106–130, 2015.

[75] Diao, Z.; Li, Z.; Wang, S.; Ding, Y.; Panchula, A.; Chen, E.; Wang, L.C.; and Huai, Y. "Spin-transfer torque switching in magnetic tunnel junctions and spin-transfer torque random access memory." *Journal of Physics: Condensed Matter*, *19*, 16: p. 165209, 2007.

[76] Liu, L.; Pai, C.F.; Li, Y.; Tseng, H.; Ralph, D.; and Buhrman, R. "Spin-torque switching with the giant spin hall effect of tantalum." *Science*, *336*, 6081: pp. 555–558, 2012.

[77] Wang, W.G.; Li, M.; Hageman, S.; and Chien, C. "Electric-field-assisted switching in magnetic tunnel junctions." *Nature materials*, *11*, 1: p. 64, 2012.

[78] Li, P.; Chen, A.; Li, D.; Zhao, Y.; Zhang, S.; Yang, L.; Liu, Y.; Zhu, M.; Zhang, H.; and Han, X. "Electric field manipulation of magnetization rotation and tunneling magnetoresistance of magnetic tunnel junctions at room temperature." *Advanced materials*, *26*, 25: pp. 4320–4325, 2014.

[79] Beaurepaire, E.; Merle, J.C.; Daunois, A.; and Bigot, J.Y. "Ultrafast spin dynamics in ferromagnetic nickel." *Physical review letters*, *76*, 22: p. 4250, 1996.

[80] Stanciu, C.; Hansteen, F.; Kimel, A.; Kirilyuk, A.; Tsukamoto, A.; Itoh, A.; and Rasing, T. "All-optical magnetic recording with circularly polarized light." *Physical review letters*, *99*, 4: p. 047601, 2007.

[81] Kimel, A.; Kirilyuk, A.; Usachev, P.; Pisarev, R.; Balbashov, A.; and Rasing, T. "Ultrafast non-thermal control of magnetization by instantaneous photomagnetic pulses." *Nature*, *435*, 7042: p. 655, 2005.

[82] Khorsand, A.; Savoini, M.; Kirilyuk, A.; Kimel, A.; Tsukamoto, A.; Itoh, A.; and Rasing, T. "Role of magnetic circular dichroism in all-optical magnetic recording." *Physical review letters*, *108*, 12: p. 127205, 2012.

[83] Stöhr, J. and Siegmann, H.C. *Magnetism: from fundamentals to nanoscale dynamics*, vol. 152. Springer Science & Business Media, 2007.

[84] Kirilyuk, A.; Kimel, A.V.; and Rasing, T. "Laser-induced magnetization dynamics and reversal in ferrimagnetic alloys." *Reports on progress in physics*, *76*, 2: p. 026501, 2013.

[85] Ostler, T.; Barker, J.; Evans, R.; Chantrell, R.; Atxitia, U.; Chubykalo-Fesenko, O.; El Moussaoui, S.; Le Guyader, L.; Mengotti, E.; Heyderman, L.; *et al.* "Ultrafast heating as a sufficient stimulus for magnetization reversal in a ferrimagnet." *Nature communications*, *3*: p. 666, 2012.

[86] Mangin, S.; Gottwald, M.; Lambert, C.; Steil, D.; Uhlíř, V.; Pang, L.; Hehn, M.; Alebrand, S.; Cinchetti, M.; Malinowski, G.; *et al.* "Engineered materials

for all-optical helicity-dependent magnetic switching." *Nature materials*, *13*, 3: p. 286, 2014.

[87] Lambert, C.H.; Mangin, S.; Varaprasad, B.C.S.; Takahashi, Y.; Hehn, M.; Cinchetti, M.; Malinowski, G.; Hono, K.; Fainman, Y.; Aeschlimann, M.; *et al.* "All-optical control of ferromagnetic thin films and nanostructures." *Science*, *345*, 6202: pp. 1337–1340, 2014.

[88] Parkin, S.S.; Kaiser, C.; Panchula, A.; Rice, P.M.; Hughes, B.; Samant, M.; and Yang, S.H. "Giant tunnelling magnetoresistance at room temperature with mgo (100) tunnel barriers." *Nature materials*, *3*, 12: p. 862, 2004.

[89] Yuasa, S.; Nagahama, T.; Fukushima, A.; Suzuki, Y.; and Ando, K. "Giant room-temperature magnetoresistance in single-crystal fe/mgo/fe magnetic tunnel junctions." *Nature materials*, *3*, 12: p. 868, 2004.

[90] Tsunekawa, K.; Djayaprawira, D.D.; Nagai, M.; Maehara, H.; Yamagata, S.; Watanabe, N.; Yuasa, S.; Suzuki, Y.; and Ando, K. "Giant tunneling magnetoresistance effect in low-resistance cofeb/ mgo (001)/ cofeb magnetic tunnel junctions for read-head applications." *Applied Physics Letters*, *87*, 7: p. 072503, 2005.

[91] Chen, J.Y.; He, L.; Wang, J.P.; and Li, M. "All-optical switching of magnetic tunnel junctions with single subpicosecond laser pulses." *Physical Review Applied*, *7*, 2: p. 021001, 2017.

[92] Radu, I.; Vahaplar, K.; Stamm, C.; Kachel, T.; Pontius, N.; Dürr, H.; Ostler, T.; Barker, J.; Evans, R.; Chantrell, R.; *et al.* "Transient ferromagnetic-like state mediating ultrafast reversal of antiferromagnetically coupled spins." *Nature*, *472*, 7342: p. 205, 2011.

[93] Li, X.; Ma, C.T.; Lu, J.; Devaraj, A.; Spurgeon, S.R.; Comes, R.B.; and Poon, S.J. "Exchange bias and bistable magneto-resistance states in amorphous tbfeco thin films." *Applied Physics Letters*, *108*, 1: p. 012401, 2016.

[94] Chen, K.; Lott, D.; Radu, F.; Choueikani, F.; Otero, E.; and Ohresser, P. "Observation of an atomic exchange bias effect in dyco 4 film." *Scientific reports*, *5*: p. 18377, 2015.

[95] Nishimura, N.; Hirai, T.; Koganei, A.; Ikeda, T.; Okano, K.; Sekiguchi, Y.; and Osada, Y. "Magnetic tunnel junction device with perpendicular magnetization films for high-density magnetic random access memory." *Journal of applied physics*, *91*, 8: pp. 5246–5249, 2002.

[96] Almasi, H.; Hickey, D.R.; Newhouse-Illige, T.; Xu, M.; Rosales, M.; Nahar, S.; Held, J.; Mkhoyan, K.; and Wang, W. "Enhanced tunneling magnetoresistance and perpendicular magnetic anisotropy in mo/cofeb/mgo magnetic tunnel junctions." *Applied Physics Letters*, *106*, 18: p. 182406, 2015.

[97] Savoini, M.; Medapalli, R.; Koene, B.; Khorsand, A.; Le Guyader, L.; Duò, L.; Finazzi, M.; Tsukamoto, A.; Itoh, A.; Nolting, F.; *et al.* "Highly efficient all-optical switching of magnetization in gdfeco microstructures by interference-enhanced absorption of light." *Physical Review B*, *86*, 14: p. 140404, 2012.

[98] Le Guyader, L.; El Moussaoui, S.; Buzzi, M.; Chopdekar, R.; Heyderman, L.; Tsukamoto, A.; Itoh, A.; Kirilyuk, A.; Rasing, T.; Kimel, A.; *et al.* "Demonstration of laser induced magnetization reversal in gdfeco nanostructures." *Applied Physics Letters*, *101*, 2: p. 022410, 2012.

[99] Liu, T.M.; Wang, T.; Reid, A.H.; Savoini, M.; Wu, X.; Koene, B.; Granitzka, P.; Graves, C.E.; Higley, D.J.; Chen, Z.; *et al.* "Nanoscale confinement of all-optical magnetic switching in tbfeco-competition with nanoscale heterogeneity." *Nano letters*, *15*, 10: pp. 6862–6868, 2015.